Lund University

Faculty of Engineering, LTH

in collaboration with Philips Research, Eindhoven

Understanding the Fundamental Optical Principles of UV-based Antifouling

Author:
Erik Wilson

Supervisors:
Ir. Bart Salters
Dr. Niklas Sköld

June 27, 2018

Lunds universitet
Lunds Tekniska Högskola

(this page will contain some more official information in the final version)

Abstract

In 2014 Salters et. al. introduced the concept of an UV-emitting wallpaper [1]. By using UVC LEDs, a completely clean ship hull surface can be achieved without polluting the marine environment with biocides, normally associated with antifouling paints. A larger hull surface area could be illuminated by a single LED if the LED light is used efficiently. Exactly how the light exits the wallpaper material, is outcoupled, is not known in ref [1]. This must be understood for a more efficient product to be developed.

Light outcoupling in the UV region is not well studied and the combination of light outcoupling and UV light's antifouling effect has never been studied before. In this master's thesis, we investigate what the antifouling causing light extraction mechanism is when UVC light, with a peak wavelength of 275 nm, is coupled into quartz. The following light extraction mechanisms, scattering, parallel rays, evanescent wave and Fresnel outcoupling, are all investigated by simulations and physical experiments.

The results indicate that scattering is an important antifouling causing light extraction mechanism and the irradiance threshold value correlates with an irradiance of $1 \cdot 10^{-8}$ W/mm^2 that has been found in previous studies to be the threshold for an antifouling effect. The results also indicate an antifouling effect of parallel rays and Fresnel outcoupling. The antifouling effect of an evanescent wave remains undecided. It is concluded that none of the proposed antifouling causing light extraction mechanisms can definitely be ruled out.

Acknowledgements

To chance. For being responsible for the existence of life, on earth, in the universe. You gave the fouling we are trying to tackle a 3.5 billion years head start - It has been a challenge worthy of my time. To Bart Salters. For showing me guidance worthy of a researcher. Without your comments, I would have lost my footing and slipped on the trail of "insight and enlightenment". May you always discard the phase of the moon in your research to come. To Cees, Elvira, Hugo, Marc, Michel, Michiel, Peter and Roelant (the Philips research team) thank you for all your time and help. You welcomed me as a stranger and gave me a farewell as a friend. Ruslan and Fetze, for your friendship and your ear. To all of the heroes of Philips innovation service, where Theo Loring shines the brightest, for all your help in sample making and ASAP delivery times. To Niklas Sköld, the radiant lighthouse you can always rely on in a storm. Thank you for all your help. Thanks to you, my research might become a vital piece in the relevant future to come.

Contents

Chapter 1

Introduction

The potential of enabling UV light's germicidal effect, the effect of killing germs and microorganisms, as an antifouling solution was first coined by Salters et al. in the context of a homogeneously UV-emitting film radiating outwards from an entire ship hull back in 2014 [1]. The concept has since then been proven to keep a surface completely clean for a longer period in areas with high fouling pressure [2]. In this thesis it is investigated how UVC light (275 nm), coupled into quartz geometries, escapes the quartz material and delivers a high enough light dose to cause an antifouling effect on the outer surface of the material. It is important to understand what exact light extraction mechanisms contribute to the antifouling effect in order to potentially decrease the required power consumption, and therefore cost, of a final product.

1.1 Background

Marine biofouling, or simply fouling, is the unwanted growth of marine organisms on hard structures, immersed in an oceanic environment. For marine vessels, fouling poses a major problem if their hull remains unprotected. A ship without any fouling protection will get increased frictional drag from increased fouling growth, something that equals an increased fuel consumption for the vessel over time. Fouling is characterized by appearance and thickness. Schultz et al. investigated the increased required shaft power on USS destroyers in 2011, and concluded that light slime requires a 9% power increase, heavy slime 18% and heavy fouling as much as 76% to maintain cruising speed [3].

Fouling is today normally tackled with antifouling solutions containing biocides that are slowly released into the marine environment, killing both fouling organisms and polluting its surroundings [4]. Increased awareness and environmental concerns have led to the introduction of more strict regulations concerning the number and the amount of biocides in future antifouling paints. This forces solution providers to look for novel solutions to an ancient problem.

One of the more promising novel solutions is the UV-wallpaper concept proposed by Philips [5], illustrated in Figure 1.1, where an entire ship hull is dressed in a UVC-emitting film with a peak wavelength of 275 nm, a wavelength with a known germicidal effect [6]. The key aspects of this solution are that all organisms are targeted, even biofilm formation is prevented, and UVC light is only emitted close to the ship's hull and does not damage the surrounding environment.

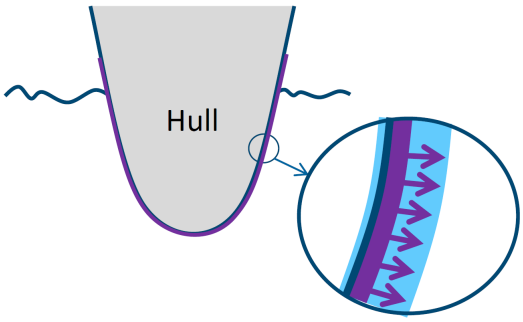

Figure 1.1: A cross-section of an immersed ship hull, dressed in an UV-wallpaper is seen. The purple arrows illustrate the emitted UVC light propagating through the blue wall-paper material, into the oceanic environment.

1.1.1 Aim

In a previous experiment, done internally, a much larger quartz surface area than expected was kept clean with a single UVC LED. The aim of this thesis is to investigate different light extraction mechanisms of UVC light ($\lambda_p = 275$ nm) in quartz waveguides.

To achieve this, quartz waveguides with embedded LEDs were immersed in North Sea water, and the fouling patterns were investigated to explore the light extraction mechanisms: scattering, parallel rays, evanescent wave and Fresnel outcoupling. From these findings, the aim is to increase the knowledge about what light extraction mechanism contribute to the antifouling effect and, therefore, enhance the efficiency of a future product.

1.1.2 Research history of UV-based antifouling by Philips

Out of several investigated UV-based antifouling concepts within the research group, the so-called wallpaper concept is one of the most promising. The wallpaper concept can be described as a film containing equally spaced UVC LEDs, covering an entire ship hull, that radiates UV light outwards from the surface. The goal is to have the film radiating a homogeneous irradiance pattern, above the antifouling irradiance threshold level of $1 \cdot 10^{-8}$ W/mm^2 [7], delivering a high enough UV-dose to either kill, or prohibit all types of fouling organisms from settling. An illustration of the concept is seen in Figure 1.1.

Different publications, discussed in next chapter, mainly investigated the *antifouling irradiance threshold level* for UVC light projected onto surfaces with intermediate oceanic water. The water will absorb part of the UV light and the irradiance level reaching the surface will be dependent on the clarity of the water. By incorporating the LEDs in a film (the wallpaper concept), the entire surface will radiate, and the irradiance threshold level will be constant and independent of water clarity.

Most of the optical power of a LED is emitted in the forward direction. When a LED is placed in an outward facing position in the UV-wallpaper, most of the light escapes directly in front of the LED. Thus the illuminated area receives an irradiance level several orders of magnitude above the irradiance threshold level which should be regarded as wasted energy. To make the wallpaper more energy efficient, the same type of LEDs were placed sideways in future iterations [2]. A plane-facing LED can illuminate a much larger area with an irradiance above the threshold level. With plane-facing LEDs, the wallpaper can act as a waveguide, which is defined as a structure that guides electromagnetic waves, such as UV light, with minimal loss and restricts the wave in one or two dimensions. Light leaks out from the material over distance, proportional to the distance from the source. To spread the light more evenly, and over a larger area, it becomes relevant to control the light outcoupling mechanisms.

One early experiment conducted in the group was to couple UVC light into a quartz plate, letting it act as a waveguide, while immersed in oceanic water. The observed antifouling pattern, seen in Figure 1.2, is one of the largest observed clean areas for a single UVC LED with an optical power of 1.3 mW to date. How such a large area remained clean is unknown and was the reason for this thesis's initially asked question - **What are the exact antifouling causing light extraction mechanisms for UVC light in quartz?**

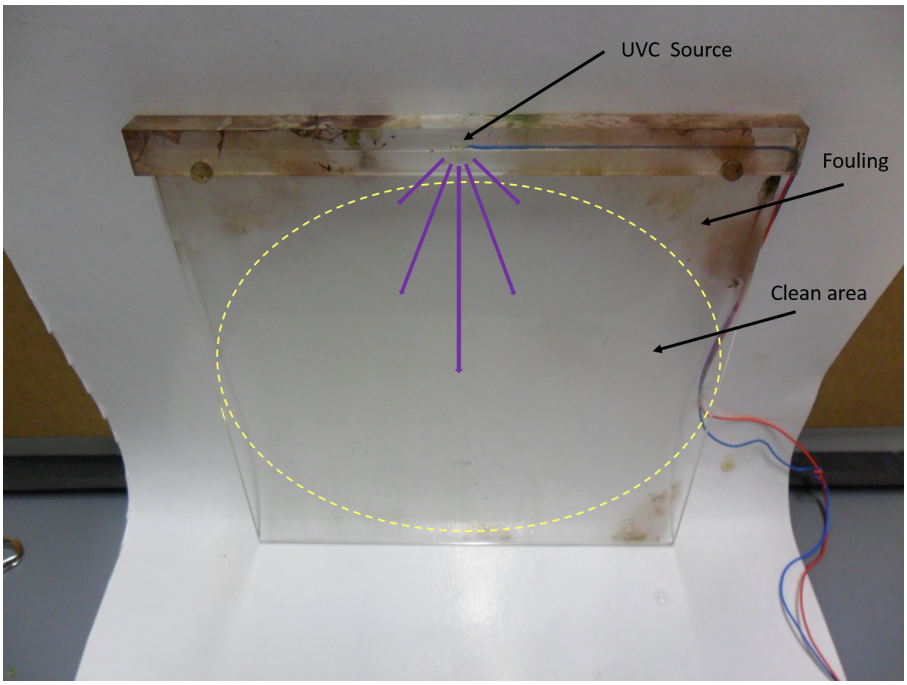

Figure 1.2: A clean circle, highlighted in yellow, is seen on a quartz plate measuring 178x178x3 mm where UVC light, purple arrows, was coupled into the quartz plate by a LED at the top edge of the plate. Fouling can be seen at the corners of the plate, outlining the clean circle, and on the PMMA LED-holder.

For an ideal non-leaking waveguide, no light should escape the quartz waveguide beyond the critical angle. The critical angle is the angle for which the light undergoes total internal reflection. Meaning, no light escapes beyond this point and all the optical power is reflected back into the waveguide.

A much smaller clean area was expected, a distance only a few centimeters from the source via light escaping by direct illumination and refracted light. Most of the light was expected to remain in the waveguide and only escape via the sides of the waveguide.

A clean circle shaped area with a diameter of 178 mm is, however, observed on the surface of the quartz plate, seen in Figure 1.2. The conclusion that UVC light actually reaches the surface follows directly from the observed antifouling effect, causing the clean circle.

The following ideas on possible antifouling causing light extraction mechanisms are explored in an attempt to explain the observed antifouling effect, seen in Figure 1.2.

- **Scattering:** Light is extracted from the quartz material by either bulk or surface scattering, caused by imperfections in the crystal. Scattering forces the light to change propagation direction and could very well send the light outwards from the waveguide, or, into an angle that can easily exit.
- **Parallel rays:** Refracted rays, originating from close to the critical angle, propagate parallel to, and on the outside of, the quartz plate surface.
- **Evanescent wave:** An evanescent wave is present on the outer surface of the quartz plate after the critical angle, and in the point of reflection. Settling organisms frustrate the light and cause light outcoupling. This concept can be compared to the quantum tunneling phenomena, the change in refractive index caused by the settling organisms result in an energy transfer across the intermediate oceanic water.
- **Fresnel outcoupling:** When light escapes before the critical angle, and moves between media of differing refractive indices part of the light is reflected back into the waveguide. For each new interaction with the waveguide surface, the same proportion of the light is refracted and reflected until the remaining optical power dissipates.

1.2 Chapter Summary

To explain the unexpectedly good antifouling behavior of UVC light, $\lambda_p = 275$ nm coupled in a waveguide, four proposed antifouling causing light extraction mechanisms scattering, parallel rays, evanescent wave and Fresnel outcoupling were proposed. The insight from investigating which one contributes to the observed antifouling effect will help in the development of more efficient UV-based antifouling products. The antifouling irradiance threshold level has previously been determined to be around $1 \cdot 10^{-8}$ W/mm^2.

Chapter 2

Theory related to UV-based antifouling

In this chapter, a closer look is taken at the underlying theory that is needed to understand the main research question - **What is the exact antifouling causing light extraction mechanism for UVC light in quartz?** Therefore, theory related to optics, light's behavior in materials and different light extraction mechanisms, and the fouling, biofilm formation and UVC's germicidal effect, is reviewed.

2.1 Guiding

To allow light to propagate farther in the material one could utilize guiding. Meaning, the light is optically confined inside the material, the waveguide, and guided away from the source. This relies on total internal reflection, TIR, when all light is reflected into the material instead of escaping the material. One requirement is that the surrounding medium, in this case, oceanic water, has a lower refractive index compared to the guiding medium. The best example of a modern application utilizing guiding is optical fibers, which transfers most of the world's Internet data.

2.1.1 Snell's law and total internal reflection

Snell's law describes the relation between incident angle and refracted angle.

Light's transition between two materials with different refractive indices is described by Snell's law, $n_1 \sin(\theta_1) = n_2 \sin(\theta_2)$. This is illustrated in Figure 2.1. The refractive index for quartz is 1.496 [8] ($\lambda = 275$ nm) and used throughout this work. A critical angle is derived from Snell's law as $\theta_c = \frac{n_2}{n_1} \sin(\theta_2)$ with $\theta_2 = 90°$, and all the rays with an incident angle greater than the critical angle will undergo TIR.

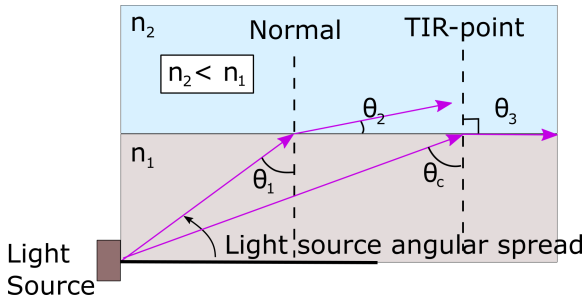

Figure 2.1: Showing how an incident ray is refracted and totally reflected at an interface between two media with different refractive indices. The refractive index of material 1, n_1, has higher refractive index than material 2, n_2, much like quartz immersed in oceanic water.

In Figure 2.1, the term 'angular spread' is seen. The angle between the forward directed LED light and the half power of the LED's emission pattern is used as the outermost angle of the emission pattern for numerical calculations.

After a certain distance from the source, depending on geometry and refractive indices, total internal reflection will happen where no light can escape. The critical angle, θ_c is the incidence angle at which total internal reflection takes place, and the distance from the source is here defined as the TIR-point, also seen in Figure 2.1. After the TIR-point no light should escape an ideal non-leaking waveguide. A distance of roughly 10 mm for our samples, which is why we were surprised by the fouling pattern seen in Figure 1.2 raised the question - how does light escape after this point, and affect fouling organisms settled onto the waveguide?

Refractive index of Salt water

The refractive index of salt water for $\lambda = 275$ nm was initially believed to be 1.38. Calculations showed that a refractive index of 1.366 is a better estimate of the refractive index for salt water with a temperature of 25°C and a salinity of 35 ppt [9]. The salinity is a good approximation of the world's oceans and the water temperature is related to the water temperature used in this work's experiments. Both values were used in this work because time constraints did not allow for simulations to be redone once the refractive index was numerically determined.

2.2 Fresnel outcoupling

Light hitting the waveguide surface with incidence angles sharper than the critical angle (before TIR-point) will be partially reflected. The reflectivity has an angular dependence given by the Fresnel equations. The reflected light will in turn for each waveguide surface reflection be partly transmitted and partly reflected. The amount of light reflected is determined by the incident and transmitted angle and the polarization of the light. This mechanism, for the periodic outcoupled light, described by the Fresnel equations, is defined as "Fresnel outcoupling".

Fresnel outcoupling, is illustrated in Figure 2.2. The figure also shows that the calculated distance to the TIR-point from the waveguide end, for a quartz waveguide slab with a height of 10 mm, immersed in salt water, is 11 mm if the LED is placed in the center. The calculations are made using Snell's law and basic trigonometry functions.

To calculate the reflected power for light rays with an incident angle greater than 0°, the polarization becomes relevant. The interested reader is referred to Appendix C, 'Optical power in Fresnel outcoupled light' for exemplified calculations.

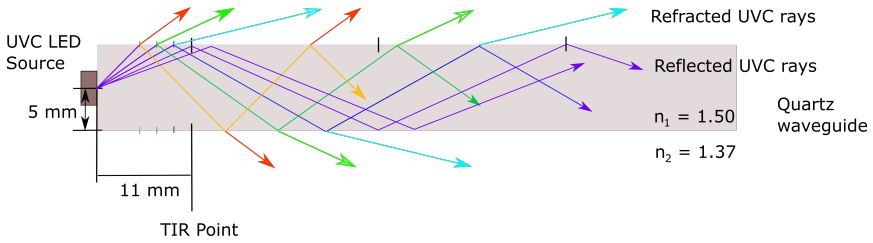

Figure 2.2: An illustration of how different light rays behave as they undergo Fresnel reflection and total internal reflection in a quartz waveguide immersed in oceanic water. Part of the light is Fresnel outcoupled, and part of the light is reflected for an incident angle smaller than the critical angle.

2.3 Parallel rays

If one continues to argue that Snell's law prohibits light to be transmitted beyond the TIR-point, the light to cause an antifouling effect after the TIR-point has to come from light refracted before the TIR-point. In theory, some light will be refracted and propagate parallel, or close to parallel, to the waveguide surface according to Snell's law. These rays, with enough optical power and little absorption from the oceanic water, can cause an antifouling effect on fouling organisms settled onto the waveguide surface.

2.4 Scattering

Fused quartz, simplified in this thesis as quartz, is an amorphous and extremely pure material, made up of SiO_2 molecules. As light rays propagate inside the material, rays interact with material aberrations, scatterers (e.g. atomic dislocations, vacancies and impurity atoms). Scatterers explain the localized change in the refractive index of the material and cause the light to change direction of propagation, which is also called scattering, resulting in less forward directed light and will cause light to exit the material regardless of the TIR-point [10].

Several scattering models have been developed over the past hundred years. They are all solutions to Maxwells equations using different approximated sphere sizes as scatterers, meaning, various boundary conditions. A sphere can be viewed as an abnormality from an otherwise homogeneous material. The scattering models have different names depending on their inventor where they take various spherical sizes to wavelength in consideration. Examples of bulk scattering models are *Mie scattering* (particles larger than the wavelength), *Raman scattering* (inelastic scattering) and *Rayleigh scattering* (particles smaller than 1/15 of the wavelength).

Within the project, an unknown quality of quartz in combination with a wavelength of 275 nm is used. Only a few [11, 12] publications exist on the scattering mechanism in quartz for this wavelength. Since characterization of the irradiance pattern remains difficult, theoretical models have to be created. The following section describes the believed scattering behavior of UVC light in quartz.

2.4.1 Rayleigh scattering

Lord Rayleigh presented his paper in 1871 in which he explained the blue color of the sky using simple arguments based on dimensional analysis [10]. He revisited the topic 1899 with the help of Maxwell, saying that scattering from air particles would suffice to give us a blue sky [11, 13]. Since then, it is believed that particles smaller than the wavelength (i.e. less than $\lambda/15$) cause Rayleigh scattering and that the intensity of the scattered light is proportional to $1/\lambda^4$ [10].

In regards to what the dominant scattering mechanism in quartz is, one article from 1995 investigated the contribution of surface, subsurface and bulk scattering. It was concluded that bulk scattering was the dominant factor at certain measurement angles. In the article, angle resolved scattering from bulk scattering fused silica (quartz) substrates was measured at 442 nm and 633 nm [11].

The main bulk scattering mechanism in quartz is suggested by Black et al. [11, 12] to be Rayleigh scattering. In [11] the bulk scattering of fused silica is correlated to Rayleigh scattering by investigating the two wavelengths of 442 nm and 633 nm, where the average scattering from investigated sample is Rayleigh in shape, but the intensity does not follow the suggested wavelength dependency. The intensities wavelength dependency is corrected for by Schröder et al. [12] where they investigate fused silica in a similar way for 193 nm. It is discovered that the intensity is not proportional to $1/\lambda^4$, as previously stated but n^8/λ^4 where n is the refractive index of the material. This is more evident for shorter wavelengths due to the wavelength dependency of the refractive index. Schröder et al. continue the theoretical reasoning where they extrapolate the wavelength dependent scattering and plot it as a function, seen in Figure 2.3.

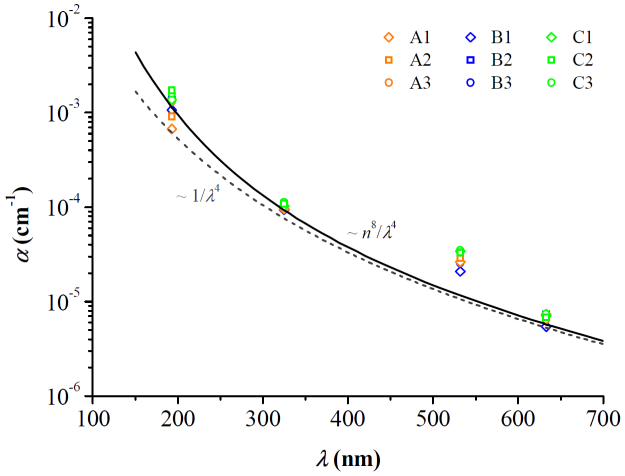

Figure 2.3: Reproduced from Schröder et al. as a plot showing measured Rayleigh bulk scattering of UVC light in fused silica (filled line), versus the dotted line following the previously believed scattering behaviour, where the symbols represent various material qualities. α is representing the scattering coefficient.

The mean distance a photon travels before a scattering event is defined as the MFP, mean free path. It is related to the material quality of the waveguide. A poor-quality waveguide has a low MFP value and hence, much scattering. For a high-quality material, quartz, it is the opposite. α, the scattering coefficient in Figure 2.3 above, can be related to MFP as a first approximation for the relevant wavelength. For $\lambda = 275$ nm $\alpha = 2 \cdot 10^{-4}$ cm^{-1}. If the MFP $= \alpha^{-1}$, $MFP_{\lambda=275\text{nm}} = 50,000$ mm.

2.4.2 Henyey-Greenstein scattering model

LightTools, LT, was the software used for optical simulations and does only allow for ray tracing, i.e. geometrical optics, to be simulated. The bulk scattering model used in LightTools, was the Henyey-Greenstein, HG, scattering model. The challenge was to let the HG scattering model replace the theoretical Rayleigh scattering model, discussed above, which was not available in LT, while being sure the scattering model represented UVC light's behavior in quartz accurate enough.

The HG scattering model is a function that allows one to alter only one integer parameter, $-1 \leq g \leq 1$, which ranges the light from back scattering, isotropic scattering and forward scattering. It is today regularly used in the biomedical field to model light scattering of tissue [14]. The HG phase function has the following appearance:

$$P_{HG}(\theta) = \frac{1}{4\pi} \frac{1 - g^2}{(1 + g^2 - 2g\cos\theta)^{3/2}} \tag{2.1}$$

where g is the anisotropy factor which describes the angular scattering distribution. It is defined as the average cosine of the scattering angles (θ) [14]. Here, only forward scattering is considered as it is the expected scattering direction for quartz [11]. Other values that were altered in the LightTools bulk scattering model are the MFP, and transmissivity.

The polar plots in Figure 2.4 are seen to illustrate the behavior of simulated UVC light. Light originates from the center of the circle, at zero, in a direction given by the g-parameter. The blue ellipse show direction and spread of the light and its relative intensity.

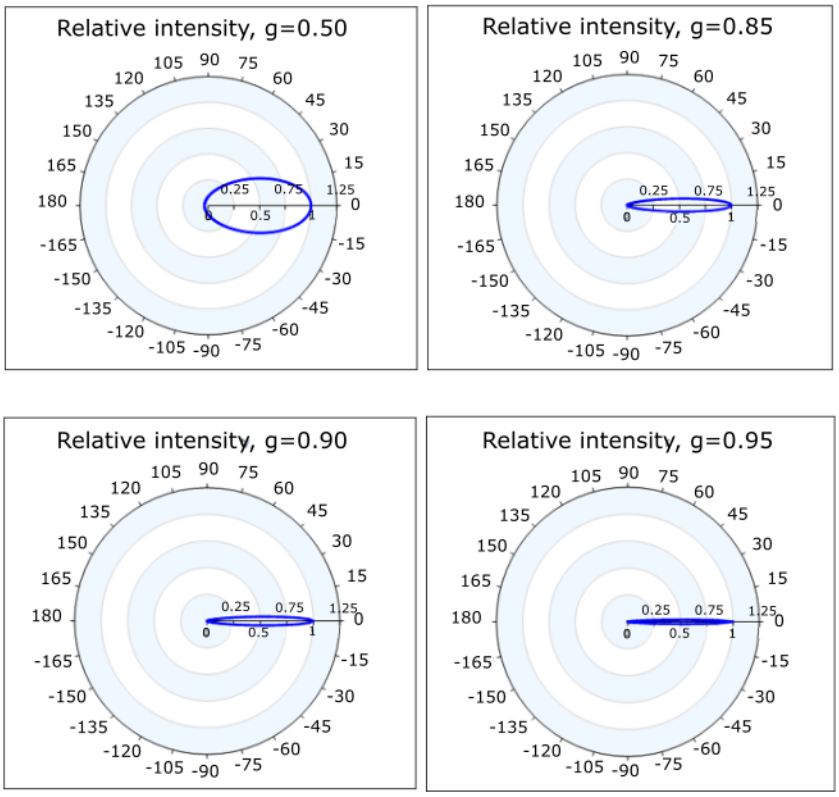

Figure 2.4: Polar plots of the relative intensity as a function of the scattering angle. Different anisotropy factors were swept in LT. The top left image has a value of g = 0.50. The top right image a value of g = 0.85 (default value in LT). The bottom left picture has a value of g = 0.90 and the bottom right image a value of g = 0.95.

2.5 Evanescent wave

If the boundary between two dielectric media is regarded, it is stated that tangential components of the electric and magnetic fields **E** and **H**, and the normal components of the electric flux densities **D** and **B**, must be continuous to fulfill Maxwell's equations [15]. The scenario, explained by geometrical optics, where incidence rays with a greater angle than the critical angle are totally reflected at the boundary of two dielectric media, does not fulfill this condition. To allow the field components to be continuous, the solution to Maxwells equations will have to be an evanescent wave.

The solution to Maxwells equations will not be covered in this chapter, but interested readers are referred to [16, 17].

For an infinitely wide beam (a beam width many times the wavelength of the source which is a good approximation in our case) the intensity (energy per unit area per second) decays exponentially with perpendicular distance z from the interface [10, 16]:

$$I(z) = I(0)e^{-z/d_p} \tag{2.2}$$

where,

$$d_p = \frac{\lambda_0}{4\pi}(n_1^2 \sin^2\theta - n_2^2)^{-1/2} \tag{2.3}$$

where λ_0 is the peak wavelength, z is the distance from the waveguide surface into the second medium. θ is the incident angle and $I(0)$ is the intensity of the surface. Depth d_p, defined as *penetration depth* indicates how far into the second medium the amplitude of the evanescent wave stretches, is independent of the polarization of the incident light and decreases with increasing θ. Note that d_p goes toward infinity, and I(z) toward I(0) as θ goes toward θ_c. Meaning, the evanescent wave is largest close to the critical angle. This is realized when inserting values in the equation $n_1^2 \sin^2\theta - n_2^2$. The term $n_1^2 \sin^2\theta > n_2^2$ when $\theta > \theta_c$ and $n_1^2 \sin^2\theta = n_2^2$ when $\theta = \theta_c$.

The above equation 2.2, is plotted in Figure 2.5 below for a few values, to give the reader a sense of the evanescent wave's behavior when an infinitely wide light beam ($\lambda_0 = 275$ nm) pass into a second media with a lower refractive index, quartz, $n_{quartz} = 1.496$ and, salt water, $n_{water} = 1.366$.

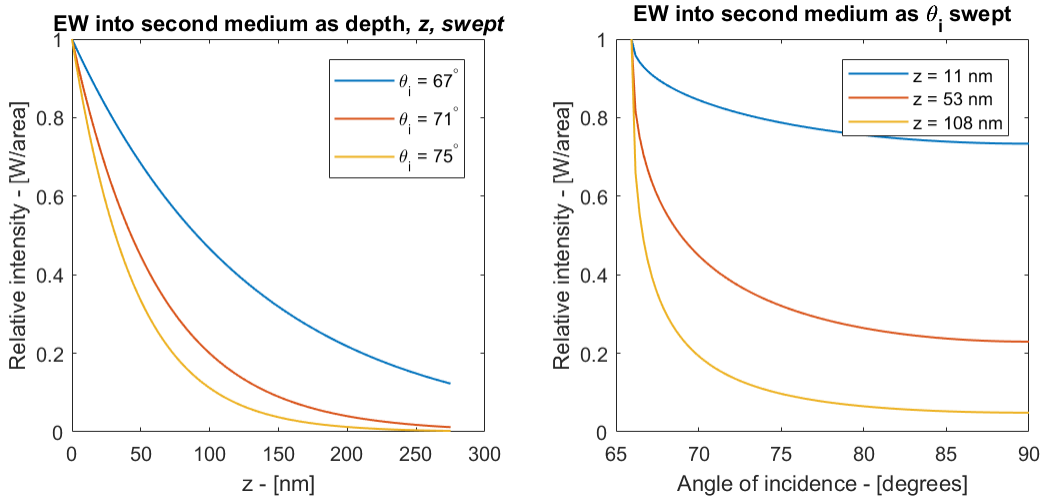

Figure 2.5: The left graph displays the relative intensity as z is swept from 0 to λ_0 for three different incidence angles, $\theta_i = 67°, 71°, 75°$. The right graph displays the wave as the incidence angle is swept from the $\theta_c = 65.94°$ to $\pi/2$ for three different distances, $z = 11, 53$ and 108 nm.

Frustrated Total Internal Reflection

The evanescent wave does not transport power across an interface. Energy is only outcoupled when something comes in contact with the evanescent wave and 'frustrates' the wave. This is called frustrated total internal reflection, FTIR, which causes some of the energy to flow across the intermediate medium, and into the frustrating object and onwards [10].

FTIR is illustrated in Figure 2.6. When a fouling organism interacts with the evanescent wave some light is outcoupled. The amount of light that is transmitted into the frustrating object is affected by the refractive index of the intermediate layer, n_2 and the frustrating object n_3. The distance between the waveguide, with refractive index n_1, and the frustrating object, as well as the angle of incidence, also affect the transmission. For light to be outcoupled, one requirement is that the frustrating object must have a higher refractive index, than the intermediate layer, and that the distance between the waveguide and the frustrating object is small enough, usually in the size range of $< \lambda_0$. [10, 18]

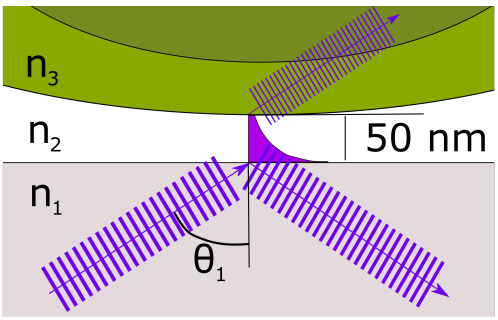

Figure 2.6: The evanescent wave of the UVC light incident toward the quartz(grey)-water(white) surface becomes frustrated by the bacteria, body in green, and some of the energy is transported into the bacteria, seen with a much less dense light beam. The image is not drawn to scale.

Once the evanescent wave becomes frustrated, the amount of transmitted light, caused by the frustrating object, various depending on refractive indices and distance between object and waveguide surface [18]. An example is seen in Figure 2.7 where a Pellin-Broca prism ($n = 1.517$) is frustrated with a dielectric slab of the same material, with intermediate air ($n = 1$). The equations and more thorough calculations are found in Appendix D

If the same example should be applied to a situation where the frustrating object is a fouling organism, and the intermediate layer is either salt water or the conditioning layer, spontaneously adsorbed macromolecules found in oceanic water (see section 2.6.1), the thickness of the intermediate layer and the refractive index of some fouling organism has to be known.

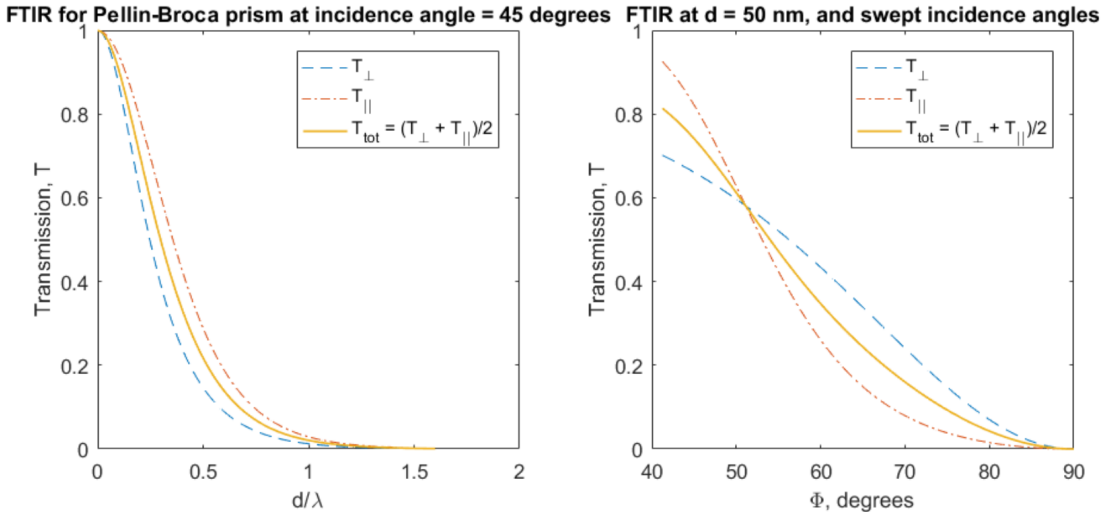

Figure 2.7: The left graph displays FTIR as a dielectric slab of the same material as the waveguide is moved closer. The incidence angle is 45° when the system has $\theta_c \approx 41.2°$. The left graph shows the transmission for a fixed intermediate distance, $d = 50$ nm, as the angle of incidence is swept from θ_c to $\pi/2$.

2.6 Fouling and biofilm formation

Fouling is here defined as the unwanted growth of marine organisms on hard surfaces, more specifically, ship hull structures. Seconds after a hard surface is immersed into oceanic water, adsorption of macromolecules causes a conditioning layer to form. Simultaneously as the conditioning layer is forming, different marine micro- and macro-organisms start probing and evaluating the surface to determine if they should settle and proceed to their next immobile life cycle step. Marine organisms as bacteria, algae, seaweed, barnacles, and mussels, to mention a few, have been identified to cause fouling problems. Fouling organisms are often categorized into micro- and macro-foulers. Bacteria, diatoms, and protozoa are defined as micro-foulers and result in a fouling layer, a biofilm, defined either as thin or thick slime depending on its thickness. The rest are called macrofoulers and are divided into soft and hard macrofoulers. Seaweed, for instance, belongs to the soft macrofoulers while mussels and barnacles are defined as hard macrofoulers due to their shells or shell-like structures.

It should be noted that fouling is not a linear process, meaning it does not follow a strict timeline where one stage of fouling takes place after the next. Instead, according to J.A. and M.E. Callow, the process should be regarded as dynamic where any fouling organism can settle independently of other fouling categories [4]. Fouling is highly influenced by outer circumstances like water temperature, salinity, pH, nutrients present in the water and water flow speed. Areas with higher fouling pressure are usually found in coastal regions close to the equator such as the coastal waters around Brazil and Singapore. A ship possesses the highest risk of fouling during low speed or under static conditions, like when idle in a harbor [4, 19].

2.6.1 Conditioning layer and biofilm formation

Microfouling, i.e. a biofilm, is most often described as the more resilient fouling category. Therefore, judging the biofilm's pattern and thickness has been adopted as evaluation method for an antifouling method's effectiveness within our group. The conditioning layer and the biofilm are also thought to affect the different light outcoupling mechanisms that are studied in the various experiments further on.

As soon as any hard surface is immersed in natural seawater, dissolved chemical compounds are

immediately adsorbed onto the surface. The initial fouling layer is adsorbed onto the surface in an entirely physically spontaneous process to neutralize surface charge, a process that takes roughly 20 hours [20, 21]. The layer is mainly made up of carbohydrates, glycoproteins, humic acids and other molecules. Carbohydrates are known to play an important role in bacterial adhesion and biofilm development [22]. The thickness of the conditional film is reported to be somewhere between 30 nm and 80 nm (characterized using ellipsometry, measured thickness depends on estimated refractive index of the conditioning film) [20]. The confirmation and thickness of the conditioning film are relevant to evaluate the likelihood of an evanescent wave having an antifouling effect.

As the conditioning layer is starting to be adsorbed, unicellular organisms, often referred to as initial colonizers, start probing the surface to evaluate if it is a suitable substrate for attachment. If it is, the previously reversible settling process becomes irreversible when bacteria start to secrete extracellular polymeric substances (EPS). As the EPS is secreted it forms a matrix for the bacteria to ensure stability, which consists of polysaccharides, proteins, nucleic acids and other useful building blocks for the bacteria to thrive [23], see Figure 2.8. As the bacteria start to divide, and new bacteria start to settle, a biofilm will form. Depending on the growth time, slime can be felt by touch or characterized by visible inspection. Even though biofilms are found on every surface in contact with water, the exact probing or sensing mechanism bacteria use to evaluate if a surface is suitable for settlement, is not known [24].

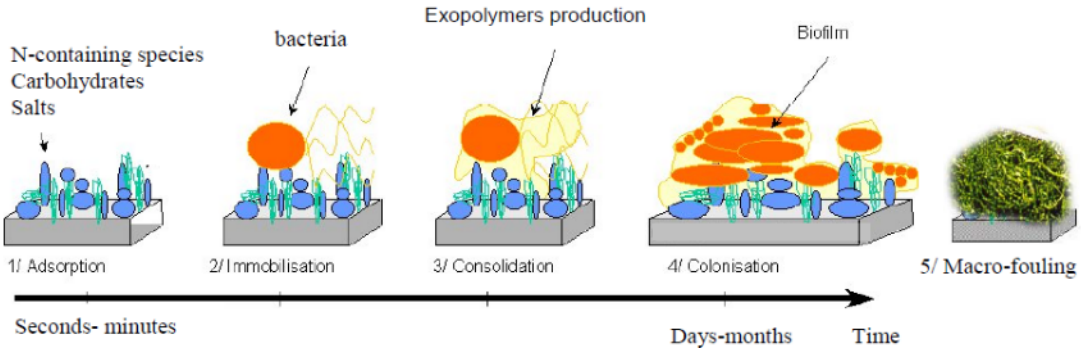

Figure 2.8: An illustration of the biofilm formation adapted from Lehaitre et al. [23]. It depicts a somewhat simplified linear fouling process starting with the initial conditioning layer to the left, followed by the settlement of bacteria and their secretion of the extracellular polymeric substances (EPS). After the EPS has been secreted a biofilm has formed, shown here with several bacteria layers. The last picture illustrates the final macro-fouling.

2.7 UVC light and its germicidal effect

The antifouling method enabled within Philips relies on UVC light produced by LED sources. The germicidal effect, meaning to kill or inactivate microorganisms, is well documented for UVC (200-280 nm) and UVB light (280-320 nm) and is used today in air and water disinfection systems where the technique is described as ultraviolet germicidal irradiation (UVGI) [6].

Germicidal efficiency reaches a peak between 260-265 nm where the largest fraction of the light is absorbed (characterized for E.coli bacterium) which is illustrated in Figure 2.9. The effectiveness varies slightly from species to species. The DNA molecule is the most UVC absorbing part of a cell's nucleus where the photons interact with the weakest link of the DNA, which is the thymine (T) - adenine (A) bond. The T-A bond consists of two hydrogen bonds, rather than three, as is the case for the cytosine (C) - guanine (G) bond. If two thymine molecules are positioned next to each other and a UVC photon breaks their hydrogen bonds to adenine, the two thymine molecules will cross-link and form a covalent bond. This molecule configuration is called a thymine dimer and has been identified as one of the main damage inducers for cells. With a sufficient amount of thymine dimmers, too many DNA transcription errors will be caused, and the cell is unable to

replicate. Additionally, UV light can cause photochemical reactions of proteins inside the cell's nucleus with an absorption peak at 280 nm [6].

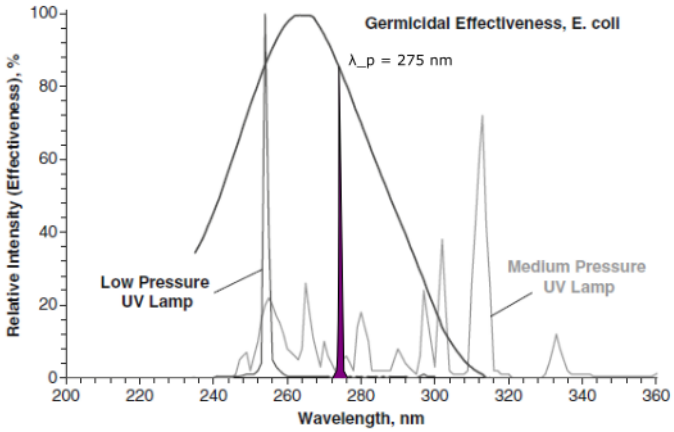

Figure 2.9: The germicidal effectiveness for varying UV wavelengths plotted for E.coli bacterium. The graph overlaps with the emission spectrum of three different types of UV sources. The peak wavelength of the UVC LED source used within the research group is highlighted in purple. Graph is reproduced from *Ultraviolet Germicidal Irradiation Handbook* [6].

The amount of UV light a microorganism requires to become inactivated is defined as the UV exposure dose (i.e. irradiance threshold level). The dose is the amount of light that inhibits more than 50% of the bacterial population to divide within the cells generation time (time for the population to double). This dose will over time lead to decay of cells and will result in a clean surface. The dose D, fluence - [J/m^2] is the product of exposure time, E_t - [sec], and irradiance, I_R - [W/m^2] [6]. The generation time varies for different marine bacteria. The growth rate of most marine bacteria isolated from water is 7-9 h at 10°C and $0.7-1.5$ h if the water temperature is increased to 25°C [25].

Most of the antifouling experiments done within the group have been conducted with continuous UVC irradiance. The required dose to keep a surface clean is therefore defined as irradiance threshold level. This threshold level has been experimentally confirmed by allowing a surface, immersed in North Sea water at 25°C, to radiate UVC light and correlate the clean area with a simulated irradiance pattern. The irradiance threshold level is not dependent on the clarity of the water and will affect all organisms close to the surface. Other experiments have been performed, outside the Philips research group, to confirm the antifouling effect of UVC light and to determine its irradiance threshold value. Patil et al. demonstrated the antifouling effect of an immersed UV lamp (254 nm) radiating onto glass slides positioned at different distances from the source. The different irradiance levels were reported to be $14.7\cdot10^{-6}$ W/mm^2, $9.6\cdot10^{-6}$ W/mm^2 and $7.3\cdot10^{-6}$ W/mm^2, where the most successful exposure times were continuous and 30 min/h where almost a completely clean surface was reported after seven days of immersion [26]. Their irradiance values are roughly two orders of magnitude higher than reported by Salters et al. [7] which is most likely explained by the light being projected onto the surfaces and the intermediate oceanic water having a UV absorbing effect. Another irradiance threshold value of $20 \pm 10 \cdot 10^{-8}$ W/mm^2 was reported by DiSalvo et al. where a low-pressure mercury vapor lamp (254 nm) was used as UV source placed behind a quartz window immersed in San Francisco bay [27].

Not every photon absorbed by a molecule results in a photochemical reaction. The energy might be dissipated by various means, such as vibrations, and therefore heat, or be re-emitted with a longer wavelength. Since not every quantum of incident energy is absorbed by a molecule, there is an absorption efficiency describing photochemical absorptivity. The quantum yield, Φ, is defined as the number of molecules reacting chemically, N_c, over the number of photons absorbed, N_p. The inactivation of, for instance, DNA, involves quantum yields in the order of 10^{-3} to

10^{-4}. UV inactivation studies of E.coli showed that only 0.025% of the bacterial DNA molecules is photochemically altered while the dose was large enough to kill 99% of the E.coli [6].

Since the transmission of the genetic information from one cell to another is key to the cells survival, the transmission requires extreme accuracy. The cell has therefore developed several DNA repair mechanisms to ensure the correct transmission of information. One of the simplest repair mechanisms involves the enzyme photolyase which binds to some of the dimers along the DNA strand and reverses the damage by using the energy from absorbed blue light. More complicated repair mechanisms are called excision repair where parts of the DNA are replaced instead of repaired. Two major categories of excision repair are base excision repair (BER) and nucleotide excision repair (NER) [28]. These repair mechanisms should be regarded because the irradiance threshold value is a result of the constant battle between a cell's repair mechanisms and the DNA-damaged induced by UVC light.

2.8 Chapter Summary

Seconds after the immersion of a hard surface in oceanic water, a conditioning layer consisting of macromolecules is adsorbed. At the same time, microfoulers start to settle to form a biofilm. A biofilm can be regarded as the most resilient fouling stage and is therefore used as evaluation of an antifouling method's effectiveness. The light extraction mechanisms believed to cause an antifouling effect are scattering, parallel rays, Fresnel outcoupling and evanescent waves. The main bulk scattering in quartz is believed to be Rayleigh scattering and was modeled by the Henyey-Greenstein scattering model in LightTools. Incident angles just before the critical angle, result in refracted parallel rays along the quartz plate surface. Fresnel outcoupling is explained by incident angles sharper than the critical angle, partly refracted and partly reflected. Evanescent waves will not contribute to an antifouling effect unless the light is frustrated by settling fouling organisms, FTIR, and the penetration depth of the evanescent wave is roughly equal to the wavelength.

Chapter 3

Experimental overview

Three experimental series were designed to investigate what light extraction mechanisms contributed to the antifouling effect. The experiments were named; Scattering experiment, Parallel ray experiment and Evanescent wave experiment. In this chapter the experiments will first be summarized followed by an overview over the scientific approach and a description of the sample construction. Each experimental series can be found in an individual, sequent chapter, where method, result, and discussion, related to each experiment, are covered. This is lastly followed with a summarizing discussion and conclusion.

3.1 Experimental series

In this section, the three experiments designed to answer what is the antifouling causing light extraction mechanism will be described. The fourth extraction mechanism Fresnel outcoupling, only discovered to contribute to the antifouling effect after some time, will be looked at and explained why it is believed to contribute. Fresnel outcoupling was also found to affect all the experiments and therefore difficult to suppress.

3.1.1 Scattering experiment

Here, we aim to investigate if scattering occurs and if it has antifouling effect. This was done by investigating the fouling pattern on quartz rods with two different diameters. Scattering would be indicated if there is a difference in the thickness of the fouling pattern after the TIR-point. A quartz rod with a larger diameter has a larger surface area, hence the (surface) intensity is expected to be lower, diluted, at a given distance from the source for the thicker rod, if scattering has an effect, and fouling is more prone to occur. The investigation was done by using two quartz rod waveguides with two different diameters, 10 and 12 mm, with a length of 350 mm. An illustration is seen in Figure 3.1 where light extraction via bulk scattering is highlighted. In hindsight, the name 'scattering experiment', is a poor choice since none of the proposed light extraction mechanisms are either suppressed or enhanced.

In this experimental series, no mechanisms were suppressed.

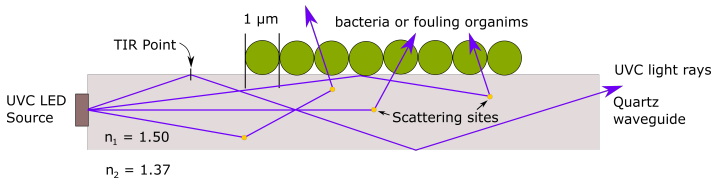

Figure 3.1: Light is coupled, to the left in the image, into the waveguide. Rays with a greater angle than the critical angle undergo total internal reflection. When the light rays interact with scattering sites, they change direction of propagation and can escape the material. If enough rays escape via the top surface of the waveguide, the surface in contact with aquaria water, an antifouling effect will be created. The image is not drawn to scale.

3.1.2 Parallel ray experiment

The purpose of the parallel ray experiment was to investigate a possible antifouling effect by refracted rays propagating parallel with the quartz plate surface. The antifouling effect of parallel rays was tested by blocking any possible parallel rays with a ceramic knife on the outside of the quartz plate. If parallel rays have an antifouling effect, a shadow pattern will be created behind the knife. An illustration is seen in Figure 3.2 where parallel rays, refracted from close to the critical angle, propagate parallel to the outer quartz plate surface. Parallel rays were considered as refracted rays with an incident angle between the critical angle and 1/10,000,000 part of a degree. The small angle of refraction is given by considering a light ray reaching to the top of a 1 μm particle, roughly 62 mm from the light source where the ceramic blade was placed.

In this experimental series, parallel rays were completely suppressed behind the ceramic knife.

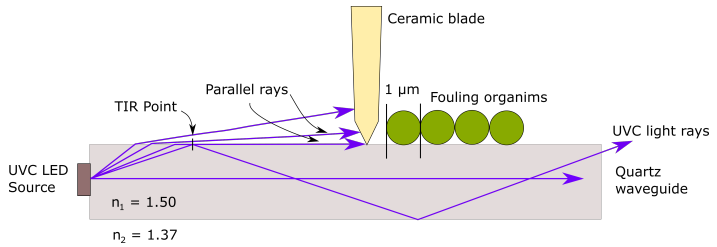

Figure 3.2: Light is coupled, to the left in the image, into the waveguide. If a ceramic knife is placed after the critical angle, any parallel rays will be blocked, and a difference in fouling would appear in front of the knife compared to behind the knife. The image is not drawn to scale.

3.1.3 Evanescent wave experiment

The purpose of the Evanescent wave experiment was to investigate if an evanescent wave has an effect on the outer surface of quartz waveguides in contact with aquarium water. The antifouling effect of an evanescent wave will be investigated by coupling UVC light in a quartz rod, inside a quartz tube with intermediate demineralized water. A possible evanescent wave will be trapped on the outside of the inner quartz rod, and therefore unable to affect settling fouling organisms in contact with the quartz tube. An illustration is seen in Figure 3.3. The resulting fouling pattern of the quartz tube will be compared with a similar experiment where the sample is a simple quartz rod only, without a covering quartz tube.

In this experimental series, the mechanisms evanescent wave and parallel rays were completely suppressed.

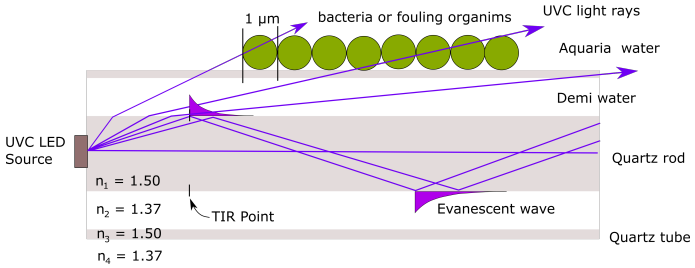

Figure 3.3: A quartz rod is placed in a quartz tube, with intermediate demineralized water. Light is coupled, to the left in the image, into the waveguide. All light rays with greater angles than the critical angle will undergo total internal reflection. At the point of reflection the evanescent wave, with a penetration depth roughly equal to the wavelength, will appear on the outside surface of the waveguide. These exponential decaying waves are illustrated in purple. The image is not drawn to scale.

3.1.4 Fresnel outcoupling

Light emitted from the source, hitting the quartz-water surface with sharper angles than the critical angle, will partly be refracted and partly reflected at the quartz-water interface, illustrated in Figure 3.5. For each additional reflection a light ray undergoes, a fixed fraction of the power is outcoupled.

A fringe-like fouling pattern appeared in many of the experiments that were believed to be caused by Fresnel outcoupling. A fringe-like fouling pattern is defined as a periodic fouling pattern with a fouling gradient in each fringe. Figure 3.4 below illustrates the definition.

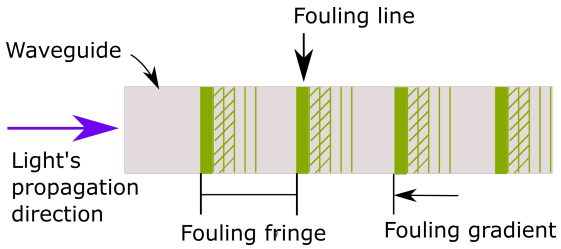

Figure 3.4: A fringe-like fouling pattern is illustrated where the light is incident from the left in the waveguide. The fringes appear in a periodic pattern, where a denser fouling line marks the start of a new fringe. A fringe also contains a very prominent fouling gradient where thicker fouling becomes less dense over distance.

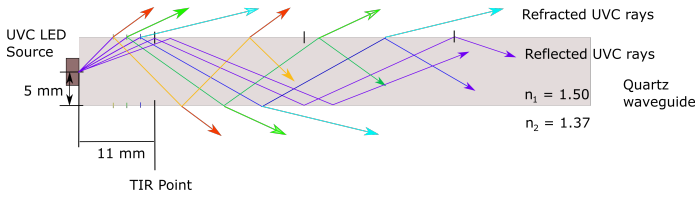

Figure 3.5: Light rays undergo Fresnel outcoupling for each interaction with the quartz-water interface. Part of the power is refracted, and part of the power is reflected. The image is not drawn to scale.

3.2 Scientific Approach

This section describes the scientific approach which provides an overview of how, and what was done to obtain the following results and conclusion.

To discover which of the suggested light extraction mechanisms have an antifouling effect, different experiments were designed to focus on one of the mechanisms by either enhancing the mechanism or suppressing and canceling out the other mechanisms.

In each experiment, UVC light from a LED was allowed to propagate in a quartz waveguide. The fouling patterns, obtained after immersing the quartz samples in oceanic water for various times, were then compared to simulated results. Here, two tools were used. First tool, the LT software, based on ray tracing yielding irradiance graphs. The second tool, Fresnel equations in MATLAB as in Appendix C. A reference sample without a LED was also simultaneously immersed for each experimental series.

The ray tracing software, LT, only accounts for geometrical optics. It is, therefore, unable to model all of the light extraction mechanisms. Scattering and Fresnel outcoupling can be modeled using LT, but parallel rays and evanescent wave are either too difficult to model or explained by more advanced theory.

If the observed fouling pattern, i.e. clean length or area, correlated with the resulting irradiance graph from the LT simulations, in respect to the irradiance threshold value, it was regarded to support the extraction mechanisms scattering and or Fresnel outcoupling. When more advanced light extraction mechanisms, parallel rays and evanescent wave, were allowed to affect the fouling pattern, the result was regarded to indicate the effect of the investigated light extraction mechanism or mechanisms, if the LT simulations failed to explain the fouling pattern observations.

3.2.1 Detection of UV light

One of the challenges of this work has been working with UVC light, wavelengths not detectable by the human eye and most camera systems. The wavelength's light-matter interaction with quartz is also relatively unknown. The previously suggested antifouling irradiance threshold level in the order of $1 \cdot 10^{-8}$ W/mm^2 is extremely low and requires a detection system with both a very high sensitivity and spatial resolution to map the irradiance of a surface accurately. Also, most of the light is suggested to escape at grazing angles (very small angles) according to optical simulations, which would require a scanning tool to capture all angles. To determine the irradiance level on the quartz surfaces we use a computer model in combination with known material properties and judge the model's accuracy by evaluating the fouling pattern on the outer surface of the waveguide.

3.3 Sample construction

The following section describes the samples of the experiments.

The quartz rods used to evaluate light output by scattering were 10 and 12 mm in diameter. The quartz rods were all 350 mm long. They had a UVC LED source in close contact with one of the quartz rod end surfaces. The LED source was placed inside an aluminum cap that acted as reflector and heat sink. The aluminum cap was placed inside a PMMA-housing to seal the construction from water. The PMMA-housing had an overlap with the quartz rod surface of roughly 3 mm, with one additional millimeter covered by sealing silicone glue. A stand was constructed in PMMA to allow the samples a vertical position in the aquaria. The design of the LED holder and PMMA-housing is illustrated in Figure 3.7 and the set-up is illustrated in Figure 3.6 A.

In the parallel ray experiment the samples are two quartz plates, measuring 178x178x3 mm in width, length, and thickness. A UVC LED was mounted in close contact, in the center of one quartz plate edge, for each quartz plate. The UVC LED was held in place with a PMMA-ledge attached to the quartz plate with two nylon screws. One of the quartz plates, with attached PMMA-ledge, was placed in a ceramic knife holder device constructed in PMMA. The quartz

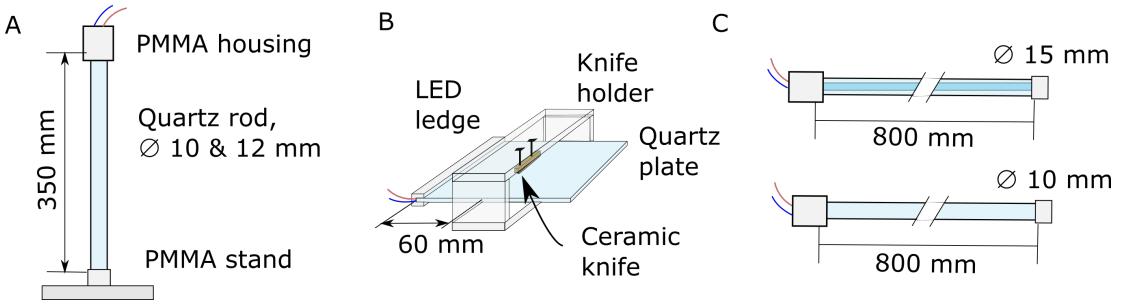

Figure 3.6: In image A the scattering experiment is illustrated, a Ø10 mm and a Ø12 mm quartz rod were positioned vertically. Image B illustrates the parallel ray experiment where the quartz plate is attached to the knife holder, and the ceramic blade is in direct contact with the top surface of the quartz plate. Image C illustrates the evanescent wave experiment. The top device has an outer quartz tube with an outer diameter of 15 mm.

plate was held in place with three screws. A ceramic knife, measuring 34 mm from *slice*™, was pressed against the top quartz plate surface in the center of the plate in width and 61.5 mm from the LED in length. The so-called knife experiment is illustrated in Figure 3.6 B.

The evanescent wave experiment consisted of two samples, both of quartz rods of 10 mm in diameter and 800 mm in length. One of the samples was placed inside a quartz tube, 800 mm long, an outer diameter of 15 mm and a wall thickness of 1 mm. The remaining space of 1.5 mm in width between the quartz rod and quartz tube cylindrical surfaces was completely filled with demineralized water. The samples were constructed with the same LED and PMMA-housing design as for the scattering experiment, as seen in Figure 3.7. The set-up is illustrated in Figure 3.6 C.

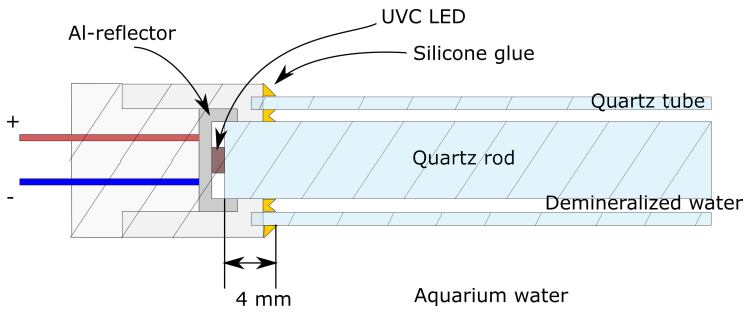

Figure 3.7: The LED-housing in PMMA and an aluminum reflector are seen close-up. This design was shared for both the scattering experiment and the evanescent wave experiment. The construction is seen with an outer quartz tube.

3.4 Chapter Summary

Three different experiments were produced to answer what extraction mechanisms are causing an antifouling effect. The scattering experiment tested if light escaped beyond the TIR-point and if altering the quartz rod diameter resulted in different fouling pattern thicknesses, which would indicated light extraction via scattering. The parallel ray experiment will consist of one experiment where possible parallel rays are blocked by a ceramic blade, and one experiment without a blade. The evanescent wave experiment suppress a possible evanescent wave and parallel rays by placing a quartz rod inside a quartz tube. This result will be compared to an equally long quartz rod without a tube with equal experimental conditions.

Chapter 4

Scattering experiment

The following chapter contains method, result, and discussion, related to the scattering experiment. The purpose of the scattering experiment was to dilute the irradiance level reaching the quartz rod surface by increasing the quartz rod diameter seen by a possible difference in fouling thickness after the TIR-point which would indicate that light escaping via scattering. None of the proposed light extraction mechanisms were suppressed in this experiment. The samples consisted of one Ø10 mm, a Ø12 mm quartz rod, and a reference sample.

4.1 Method

4.1.1 Immersion

The rods were immersed in a vertical position in the aquarium with a spacing of more than 100 mm between the samples to make sure they did not influence each other. The samples were immersed for totally 92 days. For the first 29 days, the LED sources had an optical output power of 1.5 mW, which was then lowered to roughly 0.18 mW. Due to difficulties in adjusting a very low current of the power supplies, the optical output power was set to 0.173 mW for the Ø10 mm quartz rod, and 0.21 mW for the Ø12 mm, which is roughly a 20 % difference.

The optical power was initially too high and too close to the irradiance threshold value, to clearly separate a clean section from a fouled one on the same rod. Instead, the quartz rod surface remained close to, or completely clean, which was an undesirable result. An undesirable result because a distinct difference in the fouling pattern was required to understand the effect of altering the quartz rod diameters, which was impossible if both of the rods remained clean, or close to clean. In addition, a clear transition between clean and fouled area would offer the possibility of confirming the irradiance threshold value, if the fouling pattern could be correlated with the LT irradiance graph.

After additionally 12 days the samples were retrieved from the aquaria for documentation. This was done by turning off the power, rinsing the samples with tap water and documenting the fouling patterns, before the samples were immersed again and the power was turned on. The entire procedure took roughly 30 minutes. The same type of inspection was done after another 38 days. After an additional 13 days, the experiment was terminated, and part of the Ø10 mm quartz rod surface was inspected with fluorescence microscopy.

Three similar aquaria were used for immersion of the experiments. They all contained authentic North Sea water with a measured salinity of 34 ppt and a temperature of 25 C°.

LED degradation was taken into account in the values of optical output power mentioned above. The LED degradation was internally characterized for the different LED models used.

4.1.2 Fouling pattern analysis

Images of the rods were taken with a camera, from different angles, to capture any biofilm formation. A surface was regarded as completely clean by visible inspection if no biofilm could be seen. Images were analyzed in ImageJ to characterize distances between fouling patterns and any clean lengths and areas. The width of a fringe was measured between each apparent 'fouling line', which marks a fringe. The semi-clean length of a fringe was determined by measuring the distance between the start of a semi-clean area in the next 'fouling line'. Semi-clean is defined as an obviously more clean area, or length, than a neighboring fouled area, but not totally clean, see Figure 3.4 for clarification.

4.1.3 LightTools Simulations

A an extensive LT simulation was done to correlate the observed experimental fouling pattern with theoretical simulations where the software could only handle ray optics.

The following descriptive parameters were used to construct the LT models. The quartz material was customized to resemble the correct wavelength dependent refractive index and bulk scattering model. The refractive index of quartz was 1.496, and bulk scattering was modeled with Henyey-Greenstein scattering with a g-parameter of 0.85. A g-parameter of 0.85 was chosen because it was both the default value in LT and had previously been used by the research group to model bulk scattering in quartz. The mean free path, MFP, of the quartz rods used in the models for scattering and evanescent wave experiment, was investigated in an extensive iteration process to explain the observed fouling pattern. The MFP was initially a value between 55 mm and 613 mm, depending on the quartz rod diameter (Ø10 and Ø12 mm), which was determined after having the material characterized by visible light and the amount of scattering of UVC light calculated for the different quartz rods. The material characterization procedure can be read about in Appendix A. When the scattering model did not resemble the observed fouling pattern of the initial scattering experiment, the MFP value was swept from 55 to 2,500 mm to correlate the observed fouling pattern.

The LED used in the scattering experiment was modeled with a peak wavelength of $\lambda = 275$ nm. It was modeled as an Lambertian emitter, with an angular spread, of 85°. The value of the angular spread was selected to fit the observed fouling pattern with irradiance pattern. The optical power of the sources was set to 0.173 mW and 0.21 mW for the Ø10 mm and Ø12 mm quartz rod experiments.

The irradiance detectors in the LT simulations were placed 10 μm above the quartz surfaces. This was done to avoid bouncing rays that you otherwise detect if the detector is placed directly onto the surface of the material, but still close enough to the quartz rod surface to detect refracted rays escaping the material at gracing angles. To achieve a 2-dimensional irradiance curve the detector had 1 bin in the y-direction and 350 in the x-direction, one per millimeter quartz rod length.

The number of rays used in the Monte Carlo simulations, to achieve a high enough spatial resolution, was 10,000,000 rays. The quartz rods were immersed in cubes of salt water which was modeled with a refractive index from 1.38 to 1.395. The refractive index of the salt water was swept to match observed fouling pattern with the LT irradiance pattern.

All the surfaces of the quartz geometries had Fresnel losses and a probabilistic ray split as optical properties.

More detailed information about the LightTools models can be found in Appendix B.

4.1.4 Fluorescent microscopy

A fluorescent microscopy study was conducted with the purpose to investigate if the parts of the quartz rod surface that looked clean to the naked eye, contained any fouling. Part of the Ø10 mm quartz rod was investigated 92 days after the sample was initially immersed. The PMMA-cap was removed, and the quartz rod closest to the source was cut into a 50 mm long piece, to fit into a medium-sized petri dish. The quartz rod was rinsed in BSA solution, a protein concentration standard in biochemical experiments, to avoid unnecessary cell damage. The sample was stained with LIVE BacLight from invitrogen. After staining, the sample was semi-immersed in BSA to avoid cell death. A Leica TCS SP5 Confocal microscope was used.

4.1.5 Numerical calculations of Fresnel outcoupling

To get a better understanding how Fresnel outcoupled light contributed to the antifouling effect numerical calculations were done.

One calculation compared the measured fouling fringe-width, to the theoretical based standard trigonometry, as a function of the quartz rod diameter.

The second, calculated the percentage of optical power in a set of angular dependent refracted rays to visualize the isolated effect of Fresnel outcoupling. These calculations are based on the Fresnel equations for both polarized directions where appropriate refractive indices and wavelength are used. These calculations can be found in Appendix C.

4.2 Results

The following section contains the result of the fouling patterns, LT simulations, fluorescent microscopy analysis and numerical calculations.

4.2.1 Fouling pattern

A fouling pattern, described as fouling-fringes, or just 'fringes', appeared on the outside of both the quartz rods, seen in Figure 4.1. A 1 cm completely clean length is observed, followed by a 3 cm semi-clean length, closest to the source, seen in the top of the images. Semi-clean is defined as an obviously more clean area, or length, than a neighbouring fouled area, but not totally clean. This section, closest to the source is defined as 'initial length', seen in a close-up in Figure 4.2.

Three very distinct fringes were observed after the 'initial length' and seen on both of the rods. The fringes contained a fouled area with a gradient, where the antifouling effect gradually increases up until it reaches a new, fouled area, marked by a sharp fouling line. The average fringe width was 22 mm and 30 mm, for the Ø10 mm and Ø12 mm quartz rod respectively, when considering fringe A, B and C. A close-up of the fouling pattern can be seen in Figure 4.2 and the measured values are found in Table 4.1 and 4.2. The thickness of the fouling layer was observed to be thinner for the Ø12 mm quartz rod and the fringes were shifted 9 mm further away from the source. The fouling layer was thicker on both of the rods, closest to the source (and the aquaria water surface). The reference rod, seen in Figure 4.1c is heavily fouled, with some settled macrofoulers on its surface.

(a) Ø10 mm, with $P_{opt} = 0.17$ mW

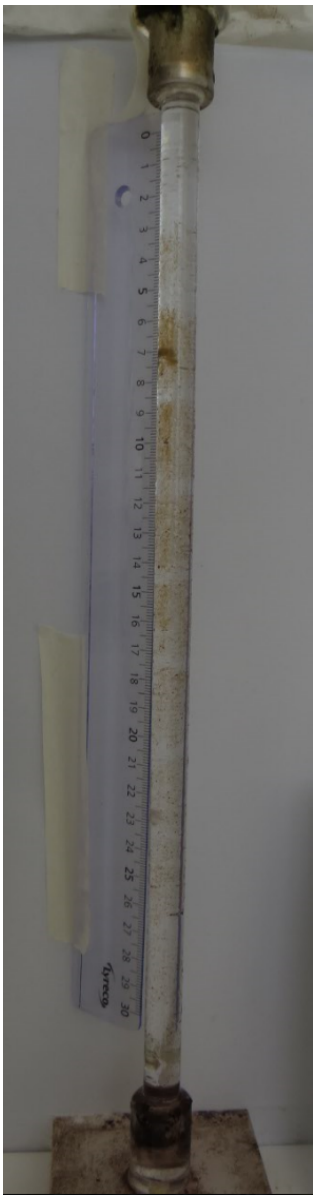

(b) Ø12 mm, with $P_{opt} = 0.21$ mW

(c) Reference rod

Figure 4.1: The fouling patterns of the three samples are compared. The light sources are placed in the top of each sample, which was also closest to the aquaria water surface. A periodic fouling pattern is seen on the Ø10 and Ø12 mm samples. The reference sample is seen to the right in the image, heavily fouled.

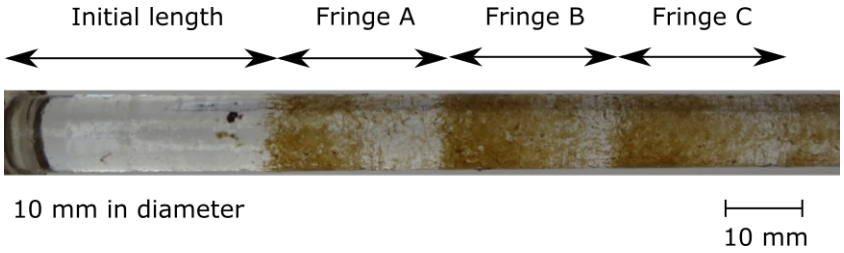

(a) Ø10 mm. LED source is placed to the left in the image.

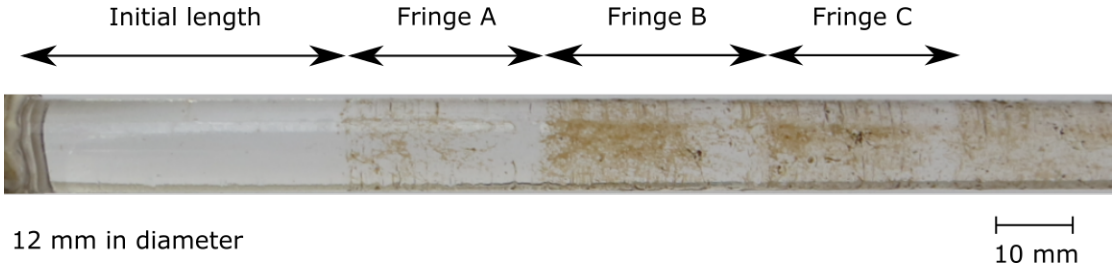

(b) Ø12 mm. LED source is placed to the left in the image.

Figure 4.2: A fringe-like fouling pattern can be seen on both the quartz rods. The LED source is located to the left in the images. The area, 1 cm closest to the source is completely clean on both of the rods. The rest of the 3.5 cm of the 'initial length' has a not so prominent biofilm, which is hard to distinguish in the images. The fringes, A-C, have a "fouling gradient" up till a very distinct fouling line, marking the start of a new fringe. The fouling is observed to be less dense on the Ø12 mm quartz rod, compared to the Ø10 mm rod. The fouling thickness is also, on average, thicker closer towards the water surface.

Ø10 mm Quartz Rod	Initial length (mm)	Fringe A (mm)	Fringe B (mm)	Fringe C (mm)
Distance from the start of the quartz rod to the fringe edge	35	59	81	105
Average width from Image 1 and 2	35	24	23	23
Image 1	34.62	23.27	23.65	22.50
Image 2	35.49	23.85	22.00	23.84
Semi-clean length	0	8.4	4.7	3.1

Table 4.1: Measured values for the 'initial length' and the three distinct fringes seen in Figure 4.2a. The numbers presented, except the semi-clean lengths, are average values from two different images, values of the width presented in 'Image 1' and 'Image 2'. The semi-clean lengths are the length of the end section of a fringe, regarded as much cleaner than the rest of the fringe.

Ø12 mm Quartz Rod	Initial length (mm)	Fringe A (mm)	Fringe B (mm)	Fringe C (mm)
Distance from the start of the quartz rod to the fringe edge	44	72	103	133
Average width from Image 1 and 2	44	29	31	30
Image 1	44.41	28.98	30.45	27.25
Image 2	42.70	28.27	30.62	32.59
Semi-clean length	0	8.5	7.8	3.4

Table 4.2: Measured values for the 'initial length' and the three distinct fringes seen in Figure 4.2b. The numbers presented, except the semi-clean lengths, are average values from two different images, values of the width presented in 'Image 1' and 'Image 2'. The semi-clean lengths are the length of the end section of a fringe, regarded as much cleaner than the rest of the fringe.

Interpretation

The thinner fouling layer of the Ø12 mm quartz rod vs Ø10 mm, is opposite to the posed hypothesis, that the light would follow standard geometrical rules and be diluted by the thicker rod diameter, and fouling more prone to occur. The effect of the wider rod, and therefore geometrical rules, is instead seen in the increased width of the observed fringes compared to the more narrow rod. The fringes indicate that Fresnel outcoupling plays a significant role and would fit with the theory of Fresnel outcoupling. The width of the semi-clean areas is also seen to decrease by each fringe, which indicates that the optical power is reduced over distance.

4.2.2 Theoretical vs measured fringe-width

The observed fouling fringes are believed to be caused by Fresnel outcoupling, explained in section 2.2. The 'initial length' and the fringe-width increased with rod diameter. The period of the fringes should be dependent on the distance, x, from LED source to the TIR-point, illustrated in Figure 4.3, which is proportional to the diameter of the quartz rod. Since the source is located in the middle of the rod, the distance x corresponds to half the fringe-width. This means that the 'initial length' in table 4.1 and 4.2 is $3x$ in length, i.e. the 'direct illumination'-part and the '1^{st} reflection', and fringe A corresponds to the 2^{nd} reflection and so forth. It is believed that very faint fouling is seen in the '1^{st} reflection' because the irradiance level is close to the irradiance threshold level, resulting in an antifouling effect.

Calculations were done for both quartz rod diameters to see if the theoretical values below correlate with the measured values. Figure 4.3 below explains the derivation of the equation. Snell's law is used in combination with basic trigonometry.

The distance between the LED source and the normal for the critical angle, i.e. TIR-point, is calculated using the following equation $x = r \cdot tan(90 - sin^{-1}(n_2/n_1))^{-1}$. One fringe-width = $2x$. For $r = 5$ mm, $x = 11$ mm and $2x = 22$ mm. For $r = 6$ mm, $x = 13.4$ mm and $2x = 27$ mm when $n_1 = 1.496$ and $n_2 = 1.366$.

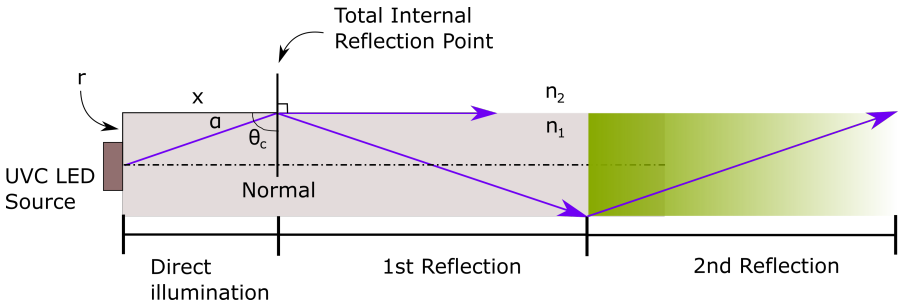

Figure 4.3: Illustrates how the fringe-width depends on the rod radius, r. The 'direct illumination'-part is the area between the LED source and the TIR-point and has no fouling due to too high irradiance.

The result is compared to the measured fringes of the Ø10 mm and Ø12 mm quartz rods, found in table 4.1 and 4.2 above. The plot of the compared results, where the fringe-width is plotted against the rod diameter for both measured and calculated values, can be seen in Figure 4.4 below.

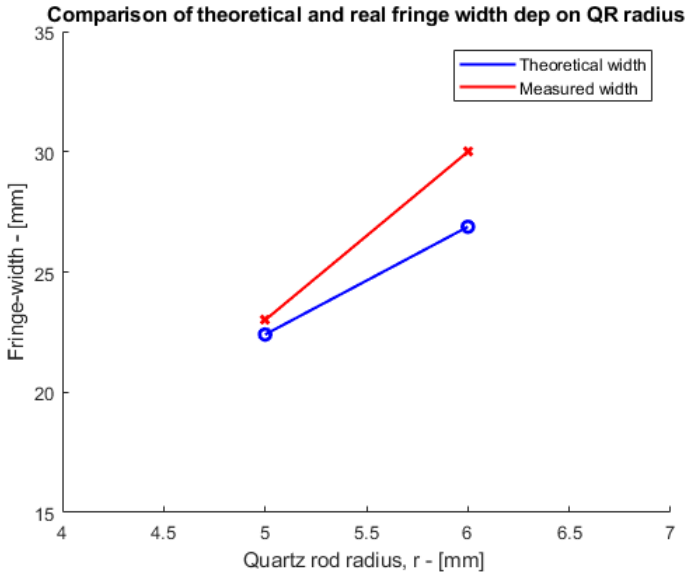

Figure 4.4: The plot contains both the measured (red) and calculated (blue) fringe-width as a function of quartz rod radius. For $r = 5$ mm the calculated value is 22 mm, and measured value is 23 mm. For $r = 6$ mm the calculated value is 27 mm and measured value is 30 mm.

The above comparison shows that the fouling fringe-width is dependent on the quartz rod diameter and that it is a close match with the shift of the TIR-point, which is the result of increasing the rod diameter.

4.2.3 LightTools results and predictions

The following graphs are from the LT models that gives us an the surface irradiance (W/mm^2) as a function of distance to the LED source. The MFP value was the main parameter altered to fit the irradiance pattern to the observed fouling patterns when the irradiance threshold value of $1 \cdot 10^{-8}$ W/mm^2 was regarded and a g-parameter of 0.85 was used in the HG-scattering bulk scattering model. The initial input value of the MFP, found during the material characterization

(see in Appendix A) for visible light, adjusted for UVC light, failed to correlate the irradiance graph with the observed fouling pattern. An extensive LT iteration process was started where the MFP was altered. The resulting MFP is presented as 'Output', in table 4.3 below. Fresnel reflection was also 'activated' as optical property on all the quartz surfaces in the LT models. A huge difference in MFP between the input- and output value can be seen.

	Input, MFP (mm)	Output, MFP (mm)
Ø10 mm Quartz rod	59	2,500
Ø12 mm Quartz rod	524	2,500

Table 4.3: Different MFP values are presented. The values in the input column are average values from the light material characterization. The output values were found to best correlate the LT irradiance pattern with the observed fouling pattern when an irradiance threshold value of $1 \cdot 10^{-8}$ W/mm^2 was used.

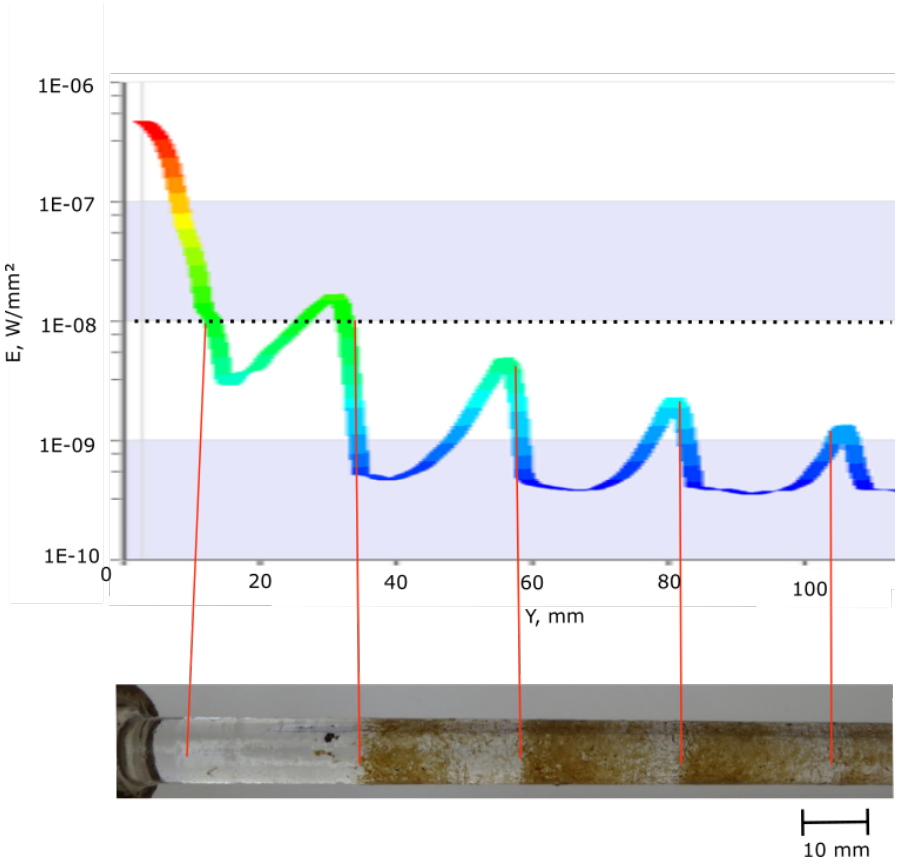

Figure 4.5: A 2-dimensional LT irradiance graph over the **Ø10 mm quartz rod** is presented. A black dashed line indicates the believed antifouling irradiance threshold level of $1 \cdot 10^{-8}$ W/mm^2. The irradiance level is above this line in two sections, $y = 0 : 12$ mm and $y = 26 : 31$ mm. The spacing between the irradiance peaks is roughly 23 mm.

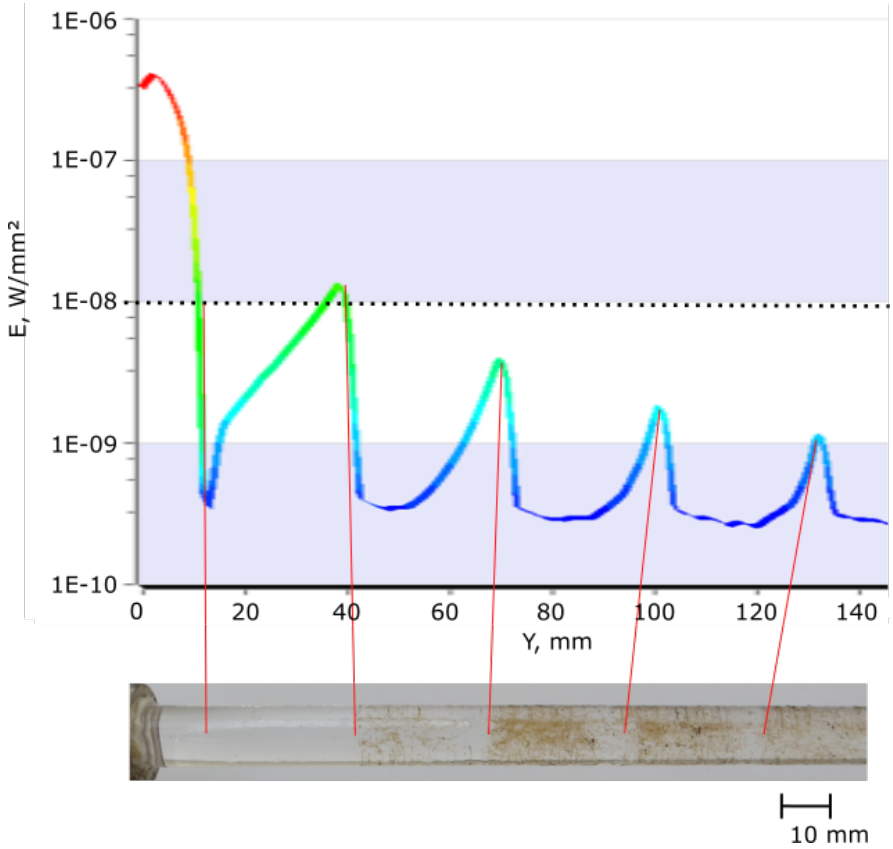

Figure 4.6: A 2-dimensional LT irradiance graph over the **Ø12 mm quartz rod** is presented. A black dashed line indicates the believed antifouling irradiance threshold level of $1 \cdot 10^{-8}$ W/mm^2. The irradiance level is above this line in two sections, $y = 0 : 11$ mm and $y = 37 : 40$ mm. The spacing between the irradiance peaks is roughly 32 mm.

Interpretation

The two irradiance graphs are seen to correlate with the observed fouling patterns, seen below the graphs, when the irradiance threshold level of $1 \cdot 10^{-8}$ W/mm^2 is regarded. The distinct irradiance peaks correlate with the observed semi-clean length and the fouled line of the fringes. The width of the fringes also correlates with the width of the irradiance peaks.

The very sharp peak, at the beginning of the irradiance curves, correlates with the first 1 cm clean length of the rods, at roughly the location of the TIR-point. The diameter of the rod, since it affects the distance between the quartz rod end, and the TIR-point, is therefore believed to affect the width of the fringes since rays are internally reflected from close to the critical angle.

Altering the MFP of the scattering model was needed to adjust the width of the irradiance peaks. The very distinct shape of the peaks is believed to explain the fouling gradient in the fringes. This close match between LT simulations and the fouling pattern suggests that the light is extracted via geometrical optics, i.e. scattering and Fresnel outcoupling. The huge difference in MFP, between the input and output, seen in Table 4.3 tells that either the material characterization was done wrongly, where the input MFP value was determined, or that UVC light has a much smaller bulk scattering effect than what is deduced extrapolated from bulk scattering of visible light.

4.2.4 Fresnel outcoupled light

The graphs and table below describe the quartz-water interface transmittance and light's reflected power depending on the angle of incidence between 0° and θ_c. The calculations are based on the Fresnel equations, found in Appendix C.

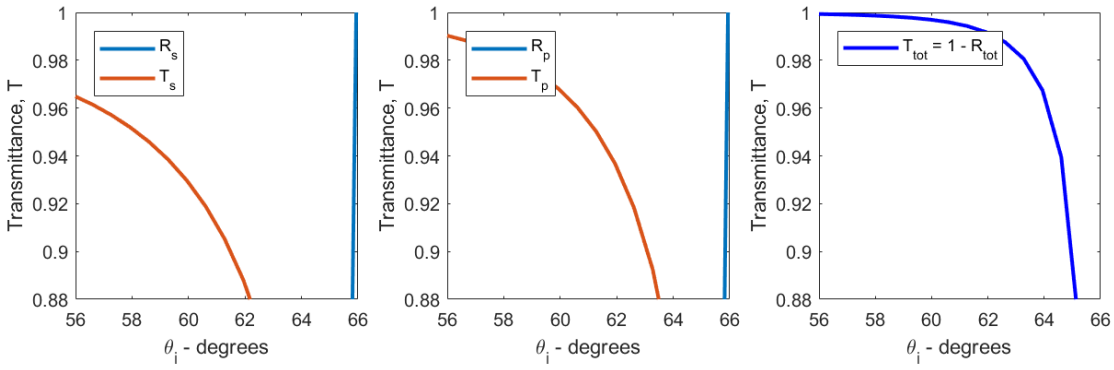

Figure 4.7: The left graph displays the fraction of the power that is reflected, R_s, blue line, and the transmittance, T_s, red line, for the transverse electric polarization. The middle graph displays the same value for the transverse magnetic polarization. The right graph is the total transmittance, T_{tot}.

Angle of incidence, θ_i	58	59	60	61	63	64	65	66
Angle of refraction, θ_r	68	70	72	74	76	79	82	90
Transmittance, T - %	95	94	92	89	85	79	66	0
Reflection, R - %	5	6	8	11	15	21	34	100

Table 4.4: The angle of incidence dependent Fresnel outcoupled light. A large reflection is seen close to the critical angle, $\theta_c = 65.94$, for a transition between quartz and seawater.

The plots create a theoretical window into the angles before the critical angle, and to the conditions of the optical power. The angles, closest to the critical angle, will allow for the optical power to partly be refracted, partly reflected and dissipate for each interaction with the quartz-water interface. The angles of incidence to allow for enough optical power to both be refracted and cause and antifouling effect and partly by reflected repeatedly, are few, seen in table 4.4.

4.2.5 Fluorescent microscopy

Results from the fluorescent microscopy investigation of the clean Ø10 mm quartz rod surface are presented below where the purpose was to analyze if an area, clean to the naked eye, contained any fouling on the microscale.

In the area, previously regarded as completely clean, seen in the top image of Figure 4.8 cells were seen in red, believed to be diatoms (a type of algae) due to their large size. Roughly 10 mm away from the source, bacteria were evident. Single bacteria with an almost equal spacing, are seen in green in Figure 4.8 *b*. Roughly 30 mm from the silicone edge, seen in Figure 4.8 *c* bacteria populations appeared, seen in a bead-like manner, next to a few diatoms. Roughly 35 mm from the silicone edge, seen in Figure 4.8 *d*, in what can be regarded as a fouled area, a great number of diatoms were seen together with several bacteria populations.

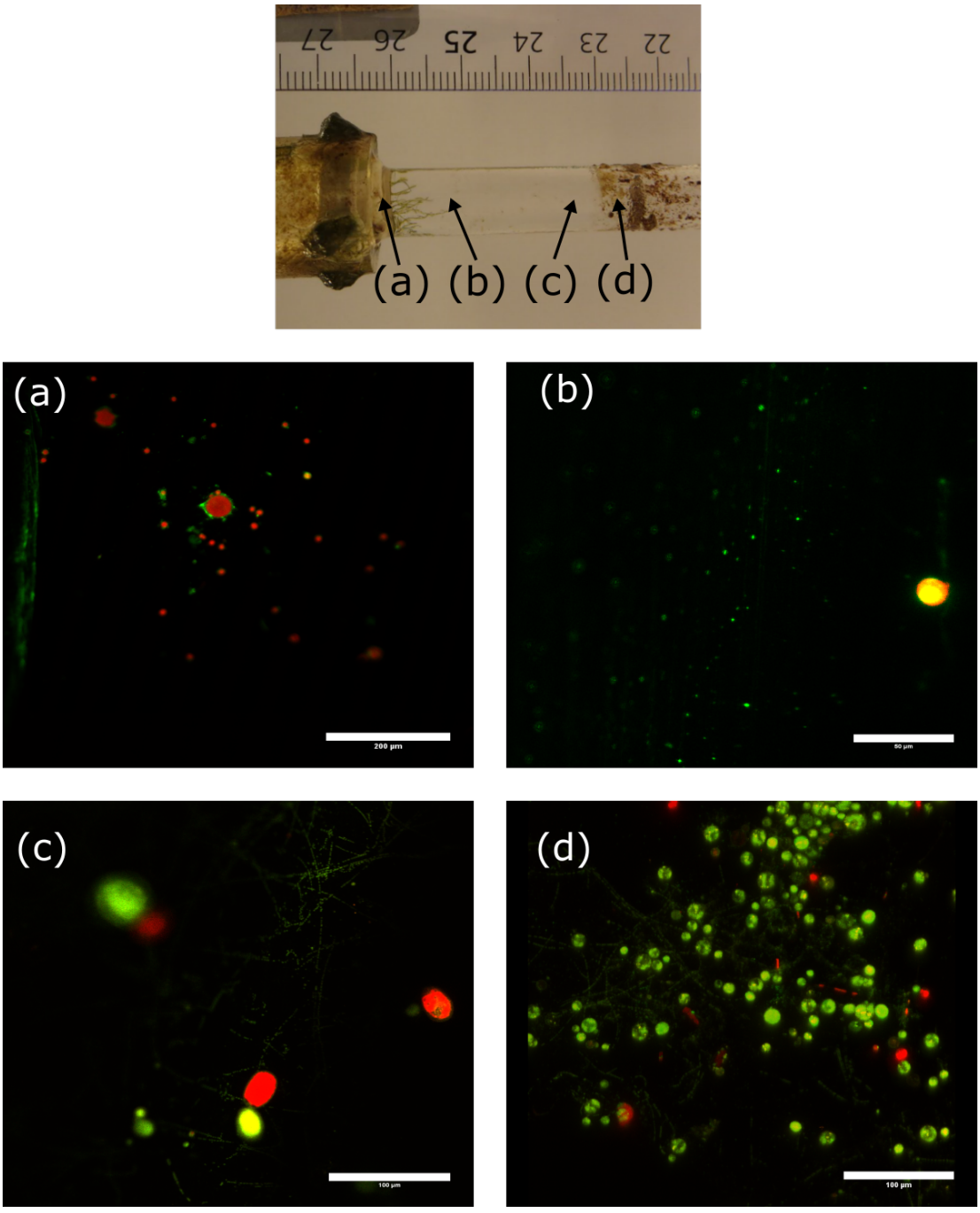

Figure 4.8: The resulting fluorescent microscopy images from various investigated areas. The top image displays the location of the investigated areas. In image *(a)* a few diatoms can be seen, but no bacteria, the scale bar is 200 μm. In image *(b)* 10 mm from the source, a few equally spaced bacteria can be seen, the scale bar is 50 μm. In image *(c)*, 30 mm from the source, populations of bacteria are starting to appear in a beads-like manner, the scale bar is 100 μm. In the fouled area, seen in image *(d)*, found 35 mm from the source, bacteria populations are seen in direct contact with a large concentration of diatoms, the scale bar is 100 μm. LIVE Baclight stains gram-positive cells fluoresce red and gram-negative cells fluoresce green, it is mainly used to create microscopy images with good contrast. Bacteria are the small green speckles seen in the images, often 1-2 μm in size.

4.3 Discussion

The purpose of the scattering experiment was to dilute the irradiance level reaching the quartz rod surface by increasing the quartz rod diameter, to investigate if geometrical optics rules, like bulk scattering, were followed by interpreting the difference in fouling patterns. It should be remembered that all of the proposed light extraction mechanisms were able to affect the fouling pattern.

After 6 weeks of immersion, and 2 weeks after the decrease in optical power, an evident fouling pattern appeared on both of the rods. The fouling layer thickness of the wider rod was thinner compared to the more narrow rod, which is opposite to the proposed hypothesis.

This means that light extraction is not only caused by scattering. We now have to look at other facts from the result, to explain the observations.

The optical power of the source, used in combination with the Ø12 mm rod, had a roughly 20% higher optical power. The increased power was due to difficulties in adjusting a low current of the power supply. The increased optical power was accounted for in the LT model and when one compares the two resulting irradiance curves for the two quartz rods, the height of the irradiance curve in Figure 4.6, compared to the irradiance curve of the Ø10 mm quartz rod in Figure 4.5, is almost equal, which should mean an equal fouling layer thickness is expected. This was not seen.

None of the suggested antifouling causing light extraction mechanisms are expected to increase in efficiency with increased quartz rod diameter. The increased fouling efficiency is instead believed to be attributed to the higher material quality and the more smooth surface of the Ø12 mm quartz rod. Less fouling on the Ø12 mm quartz rod could be attributed to fewer surface scratches. Fewer scratches would mean less light distortion, allowing more light to reach the surface, leading to settling fouling organisms experiencing more frustration. Also, fouling organisms are known to have difficulties adhering to a more smooth surface.

It seems likely that less fouling occurred due to a combination of these two reasons. Other explanations to the varied fouling thickness could be the LED sources not having the correct optical power output, stated by its specification datasheet. The LED sources were not individually characterized. The LEDs are expected to vary slightly from their specifications, but not enough to explain the observed fouling difference. Lastly, the Ø12 mm quartz rod was placed in the opposite corner of the aquarium, compared to the Ø10 mm rod, where less ideal fouling conditions like faster water flow speed, and less amount of incident sunlight, would also contribute to less fouling.

An initially unexpected result was the fouling fringes that appeared on the cylindrical quartz rod surfaces. The fringes appeared in a periodic manner with a clear fouling gradient inside each fringe. This distinct pattern is thought to be explained by partly refracted and partly internally reflected light originating from a section before the TIR-point. This behavior would be explained by Fresnel outcoupling. Fresnel outcoupling would mean that light from the source, in a periodic manner, is constantly refracted/reflected from the quartz rod surface along the length of the rod, till the optical power finally dissipates. The observed decreased semi-clean length of the fringes, summarized in Table 4.1 and 4.2, indicates a dissipating power for each periodic refraction/reflection.

The roughly 10 mm clean length closest to the source was seen on both rods, which marks the location of the TIR-point. The sharp edge, the fouling line, defining each fringe, is believed to be attributed to the TIR-point at the beginning of the rod. The fringe-width also clearly has a rod diameter dependency which proved to be related to the shift of the TIR-point.

The fluorescent microscopy analysis, done on the area closest the the LED source, confirmed that the initial clean length was completely clean also on the micro scale.

Numerical calculations illustrating the fractional output power by Fresnel equations, seen in Figure 4.7 and in Table 4.4, showed the few incidence angels for when enough optical power would both be refracted and cause an antifouling effect, and be repeatedly reflected. This result questions if more antifouling causing light extraction mechanisms are behind the observed fouling pattern.

A LT iteration process was started to find an irradiance pattern that would explain the fouling pattern. Fresnel reflection was activated as an optical property for the quartz surfaces, and the

MFP of the HG scattering model had to be increased in value for the irradiance peaks to be as wide, and sharp, to fit the fouling pattern.

A fairly good correlation was obtained between the fouling pattern and the irradiance curve for a MFP value of 2,500 mm when an irradiance threshold of $1 \cdot 10^{-8}$ W/mm^2 was assumed. The only completely clean length is seen 10 mm from the source where the irradiance peak admittedly reaches a value 15 times higher than the irradiance threshold level, but intersects with the irradiance threshold value roughly 10 mm from the source. The obtained irradiance peaks reaches an irradiance value between $3 \cdot 10^{-9} - 1 \cdot 10^{-8}$ W/mm^2 and would explain the semi-clean lengths.

The fouling pattern can therefore be explained by LightTools, which includes scattering and Fresnel outcoupling. Scattering cannot be the only extraction mechanism due to the thinner fouling layer of the wider rod, but according to the LT simulation and the very close correlation between model and fouling pattern, scattering can still be argued to be required to explain the very characteristic pattern of the fringes. Altering the scattering parameter, MFP, was necessary to fit the width, and the sharpness, of the fringes. A smaller MFP value, meaning more scattering, smoothed out the fringes. It also affected the position of the bottom part of the irradiance graph (i.e. 'background radiance'). A comparison between two irradiance graphs can be seen in Appendix B, '*Why scattering is required*', where no scattering and only Fresnel outcoupling is compared to a model with scattering, having a MFP value of 55 mm. Scattering seems to be, an antifouling causing light extraction mechanism, because the appearance of the fouling pattern, according to LT, cannot within our model be explained without it.

Therefore, in this experiment, both scattering and Fresnel outcoupling were indicated as antifouling causing light extraction mechanisms.

The final MFP value of 2,500 mm was a value 5 and 42 times larger than first predicted in the material characterization step. The only explanation is that either the material characterization was done wrongly, or UVC has a much smaller scattering effect than predicted. There are few, or no values, in the literature to compare how reasonable this value is. If the scattering coefficient for quartz, provided by Schröder et al. in Figure 2.3 is converted to MFP as a first approximation, a MFP of 50,000 mm was given. This value is 20 times larger than used in LT but it is worth reminding that this value is highly dependent on the g-parameter of the HG scattering model.

It is still unknown why both of the quartz rods are successfully modeled with the same MFP value of 2,500 mm when the material quality between the two rods appears to be vastly different when inspected in the visible regime. The Ø10 mm rod had hazy quartz rod ends, believed to act as diffusers, and both the rod's surface and volume had considerably more visible scattering sites, compared to the Ø12 mm rod. One possible explanation is that macro scatterers do not affect UVC light in a profound way. It is evident that more research has to be done in this area.

In hindsight, this experiment with the purpose to mainly investigate scattering was poorly designed since all the light extraction mechanisms affected the fouling organisms and since they were so different in quality, and in immersion conditions. A more suited experiment would have been to use a UVC laser through a quartz rod, then bulk scattering would have been the only light extraction mechanism.

Chapter 5

Parallel ray experiment

The following chapter contains method, result, and discussion, related to the parallel ray experiment. The purpose of the parallel ray experiment was to investigate a possible antifouling effect by refracted rays propagating parallel with the quartz plate surface. These were completely blocked with a ceramic blade in close contact with one of the quartz plate surfaces and the fouling pattern behind the blade was compared to an experiment without a blade. The experimental series consisted of one experiment with a ceramic blade (the knife experiment), one without a ceramic blade (the non-knife experiment), and a reference sample without a LED.

5.1 Method

5.1.1 Immersion

The two samples belonging to the parallel ray experiment were immersed and terminated after 7 days due to malfunctioning because of water leakage, causing the LEDs to short circuit. The LED of the knife experiment failed 5-24 hours before termination of experiment and the non-knife experiment failed 24-48 hours before termination. Both the LEDs had an optical output power of 1.3 mW. The samples were placed on the aquarium bottom in a standing position to avoid collecting sedimentation.

5.1.2 Fouling pattern analysis

The fouling patterns were analyzed in a similar way mention in Chapter 4, Scattering Experiment. The resulting images, seen below, are best visualized on a computer screen.

5.1.3 LightTools Simulations

Initial simulations did not correlate with the observed fouling pattern, and the MFP value was swept from 60 to 20,000 mm. The final MFP value of the quartz plate material was determined when the LT irradiance curves matched the respective fouling patterns, considering the irradiance threshold value of $1 \cdot 10^{-8}$ W/mm^2.

The LED used in the parallel ray experiment was modeled with a peak wavelength of $\lambda = 275$ nm. It was modeled as an Lambertian emitter, with an angular spread of 65°. The value of the angular spread was given by the LED's specification sheet. The optical power was 1.3 mW.

The quartz plate irradiance detector had a grid of 178x1780 bins in x- and y-direction and was placed 1 μm above the surface in the simulations. The detector had ten times more bins in the y-direction to increase the spatial resolution in the forward direction of the LED light.

The number of rays used in the Monte Carlo simulations was 120,000,000 rays.

All the surfaces of the quartz plate had Fresnel losses and a probabilistic ray split as optical properties. More detailed information about the LightTools models can be found in Appendix B.

5.2 Results

The following section contains results of the fouling patterns, LightTools simulations, and from numerical calculations.

5.2.1 Fouling pattern

Neither the knife experiment nor the non-knife experiment had any truly clean areas. Instead, a triangular shaped pattern with less fouling was seen in front of the LED sources. Behind the ceramic knife, indicated with a yellow line in Figure 5.1a, 5.2 and 5.3, a higher fouling density was seen, compared to areas not shadowed by the knife at the same distance from the source, seen in Figure 5.1b and 5.4. The increased fouling density behind the knife was distinguished by observing the difference in reflection from the lab's fluorescent tubes, best seen at grazing angles in Figure 5.2 and 5.3.

Fouling-fringes were again observed, mainly in the triangular shaped fouling pattern on the quartz place, close to the end-edge of the quartz plate. The fringes were similar in appearance as described in section 4.2.1, but circular shaped, with one part fouled and one part less fouled (semi-clean). A fringe was measured at 7.3 and 7.9 mm in width, for the knife and non-knife experiment. 36% and 43% of a fringe's length were regarded as visibly more clean for the knife and non-knife experiments. A close-up of the fringes can be seen in Figure 5.5. A single space between the source and the first observable fringe, of roughly 110 mm and 79 mm, was observed for the knife and non-knife experiment. These numbers are useful when comparing how well the fouling pattern is matching the simulated LT irradiance pattern. They are summarized in Table 5.1.

The knife experiment had more fouling on the left side of the quartz plate, seen in 5.1a. This side was also closest to the water surface. The non-knife experiment had more fouling on the top side of the quartz plate, mostly covering the LED ledge. This side was positioned closest to the surface.

The reference plate, seen in Figure 5.1c, was regarded as completely fouled with soft fouling. The top side of the reference plate can be seen with more fouling. This side was closest to the surface.

Parallel ray experiment	Knife	No Knife
Fringe period (edge to edge) (mm)	7.3	7.9
% of Fringe semi-clean	36	43
Distance between source and first fringe (mm)	110	79

Table 5.1: Data from the observed fouling pattern on the knife and non-knife experiment. Fouling fringes appeared where one part was fouled, and one was part semi-clean. A difference between the observable distance between the source and the first distinct fringe was seen for each experiment.

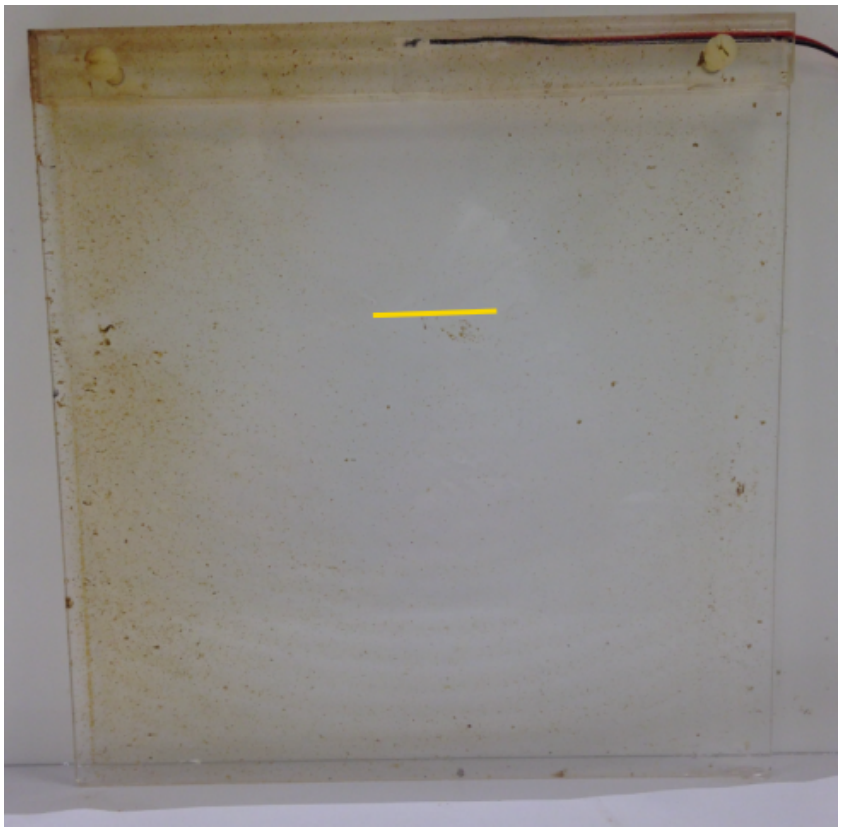

(a) Knife experiment

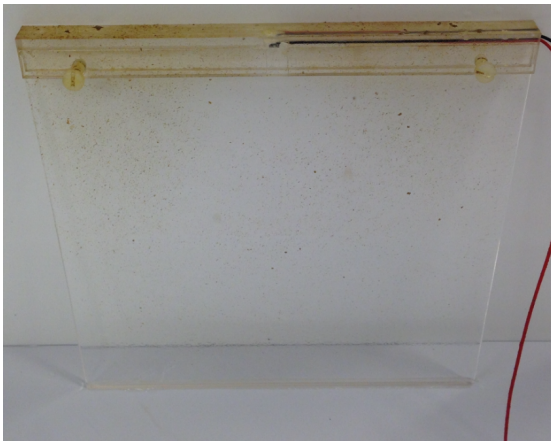

(b) Non-knife experiment

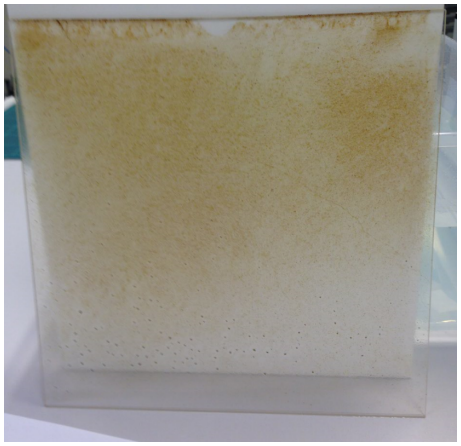

(c) Reference plate

Figure 5.1: The quartz plates after seven days of immersion and rinsed. The knife and non-knife experiments both had an optical power of 1.3 mW. The knife location is marked with a yellow line in Figure 5.1a. Fringes are faintly seen in the bottom left part of Figure 5.1a. A close-up of this area is seen in Figure 5.5.

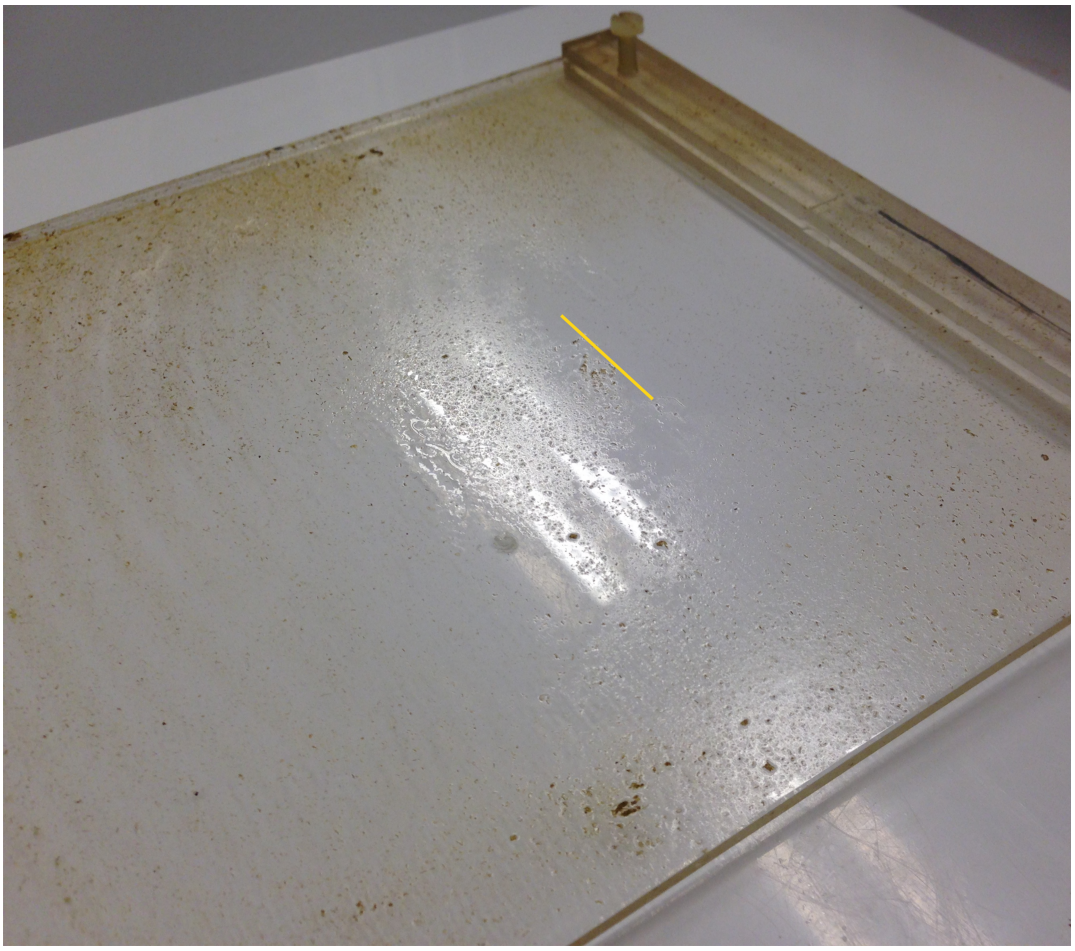

Figure 5.2: The knife experiment is viewed at grazing angles. The yellow line marks the location of the knife. More fouling is seen to the left of the yellow line, the area shadowed by the knife. Less reflection from the lab's fluorescent tubes is seen in the quartz plate surface, indicating a thicker biofilm. A close-up of the area is seen on the next page, in Figure 5.3.

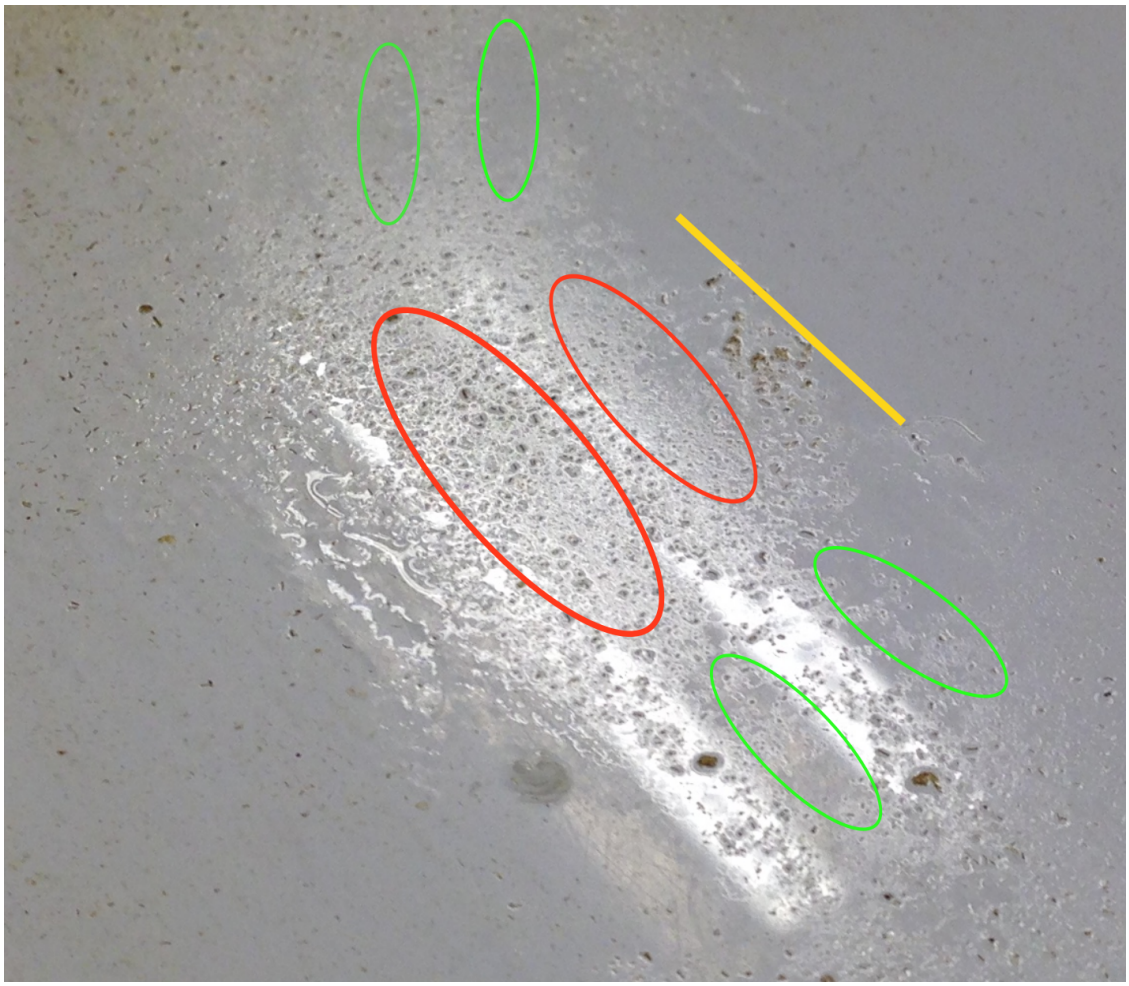

Figure 5.3: A close-up of the most interesting area of the knife experiment is seen. The yellow line marks the location of the ceramic knife. The circles highlight interesting areas. In the green circles, less fouling can be seen, compared to the content in the red circles located on the same fringe, or semi-circle.

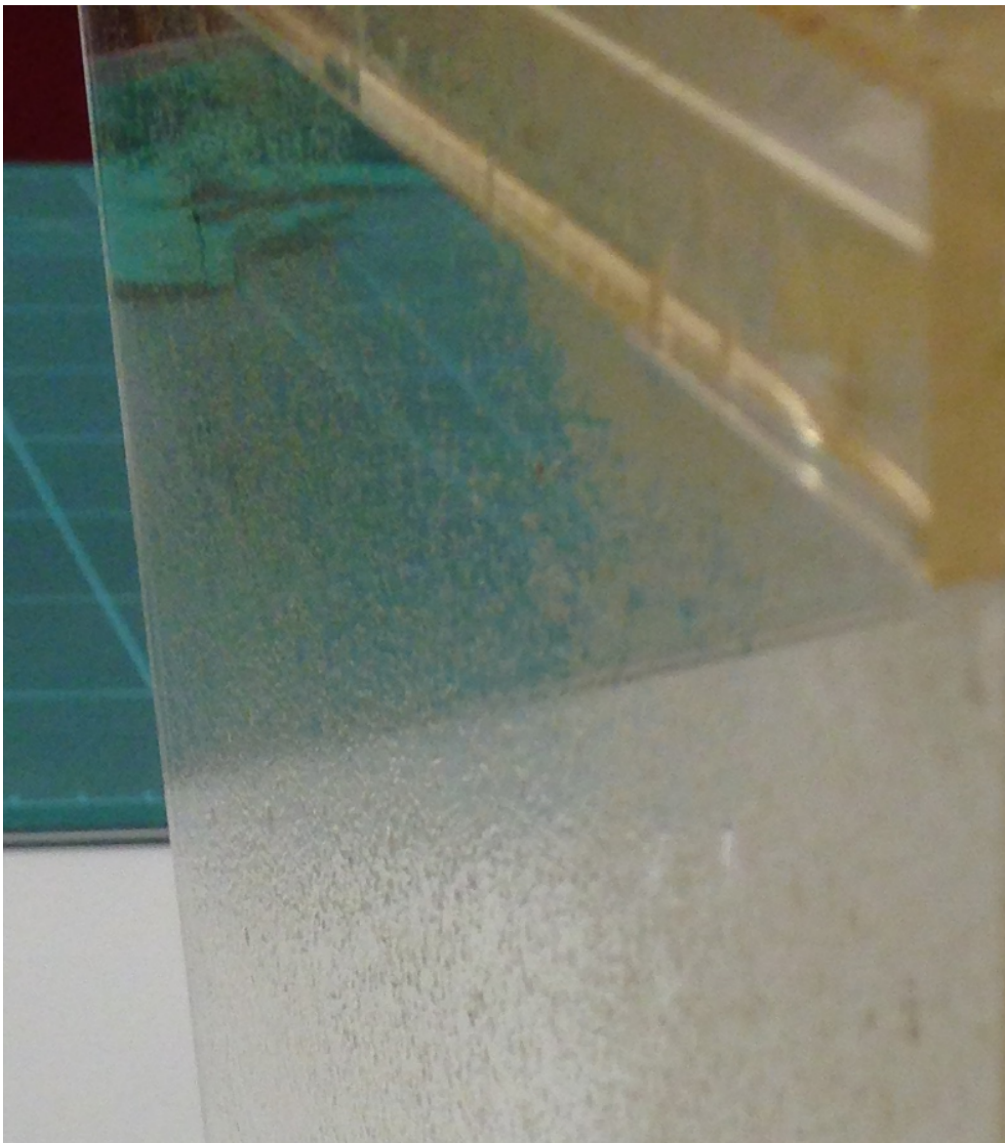

Figure 5.4: The non-knife experiment seen up close at grazing angles for easy comparison with Figure 5.2. The LED source is positioned in the top of the image. Less fouling is seen closer to the source. The distinct line, separating less from thicker fouling, is highlighting the angular spread of the LED.

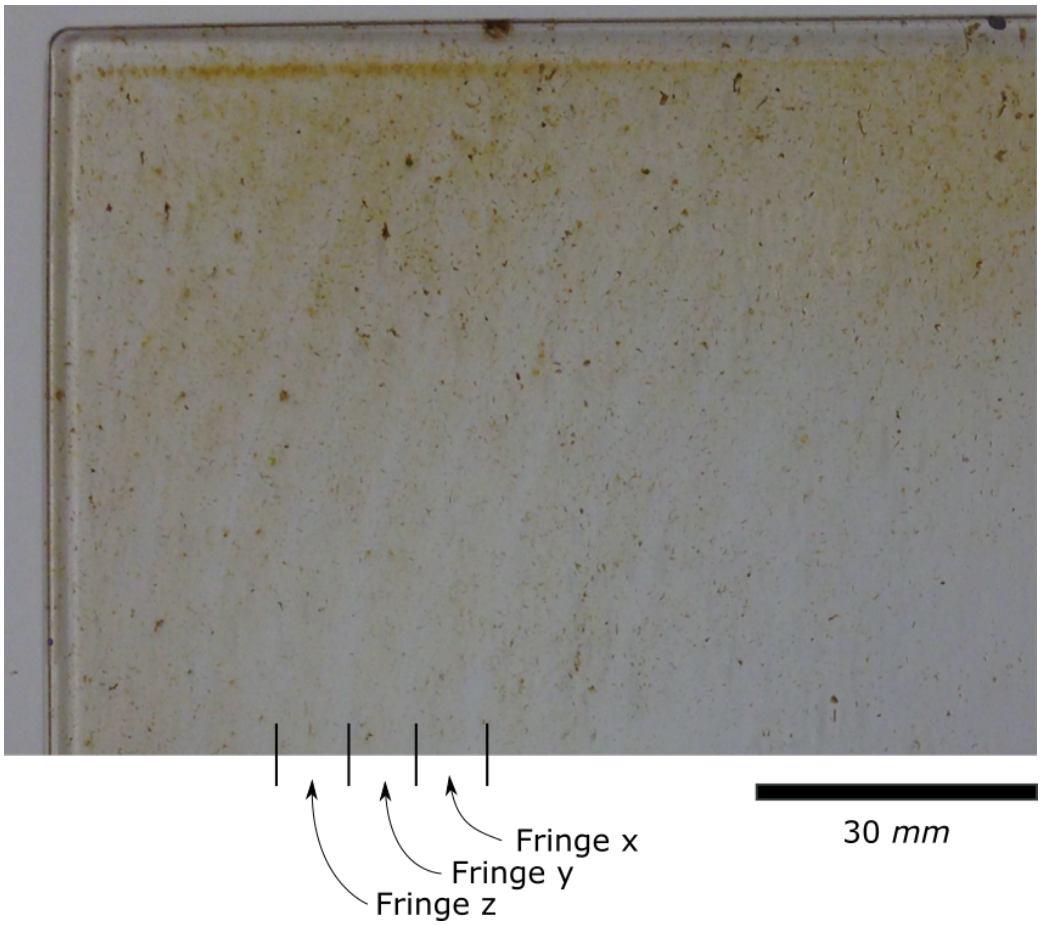

Figure 5.5: A close-up of the fringes is seen from the knife experiment. Some of the fringes are labeled as Fringe x,y,z to facilitate their distinction. The fringes are best visualized on a computer screen.

Interpretation

The observed increased fouling thickness behind the ceramic blade suggests that parallel rays have an antifouling contributing effect. When the fouling pattern of the non-knife experiment is inspected up close, a fouling gradient is observed which has less fouling closer to the source. The observed fouling fringes, in combination with the lack of fringes directly in front of the LED source, suggest that other antifouling causing light extraction mechanisms than parallel rays are affecting the fouling pattern.

5.2.2 LightTools results and predictions

The following graphs are from the LT models created to correlate the irradiance pattern with the experimental results, i.e. the fouling patterns. The MFP value was the main parameter altered to fit the irradiance pattern with respect to the observed fouling patterns when the irradiance threshold value of $1 \cdot 10^{-8}$ W/mm^2 was regarded and a g-parameter of 0.85 was used in the HG scattering model. The resulting MFP is presented as 'Output', in table 4.3 below. Fresnel reflection was also 'activated' as the optical property on all the quartz surfaces in the LT models.

	Input, MFP (mm)	Output, MFP (mm)
Quartz plate	-	20,000

Table 5.2: The output value was found to best correlate the LT irradiance pattern with the observed fouling pattern when an irradiance threshold value of $1 \cdot 10^{-8}$ W/mm^2 was used.

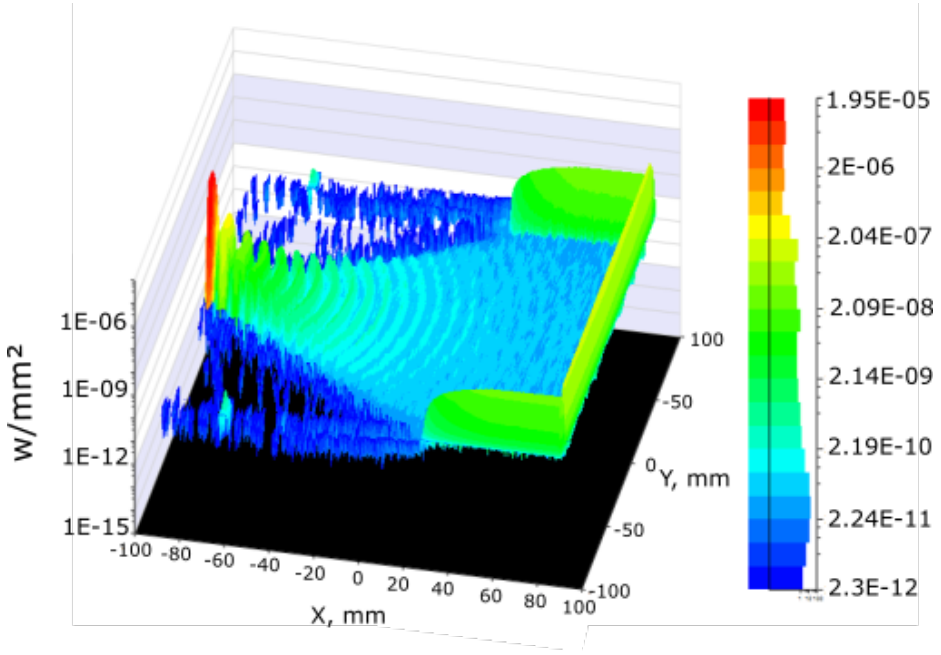

Figure 5.6: A 3-dimensional LightTools irradiance graph over an illuminated quartz plate is seen. No simulated ceramic knife was used. The quartz material had a MFP of 20,000 mm and a g-parameter of 0.85. The LT-detector was placed 1 μm above the quartz plate surface and had 178 bins in y-direction and 1780 bins in x-direction. The irradiance peaks have a period of roughly 70 mm. The first four irradiance half-circles all have an irradiance value above $1 \cdot 10^{-8}$ W/mm^2.

Interpretation

The LT irradiance pattern from the parallel ray LT model is not as close a correlation with its experimental fouling pattern, as previously seen for the scattering experiment. The period of the irradiance peaks matches well with the measured fringe period, seen in the fouling pattern of Figure 5.5 and summarized in Table 5.1, but the irradiance pattern has the following deviations. A clean area closest to the source is expected since the irradiance level in this area is above the irradiance threshold value of $1 \cdot 10^{-8}$ W/mm^2 according to Figure 5.6. This was however not observed.

Also, the irradiance peaks close to the edges of the quartz plate where fouling fringes are seen have an irradiance value roughly one order of magnitude smaller than that of the scattering

experiment. An unexpected value, because the fringes furthest away from the source, are the most prominent according to the fouling pattern, as seen in Figure 5.5.

The angular spread of the simulated light cone, i.e. the angular spread of the propagating irradiance pattern in Figure 5.6, matches the spread of the observed semi-clean fouling pattern of the quartz plate. The HG scattering model is required in the LT model to match the irradiance peaks to the fouling pattern, and the irradiance peaks do not exist if Fresnel reflection is not activated as an optical property, which suggests that these light extraction mechanisms, in combination with parallel rays, are needed to explain the fouling pattern.

5.3 Discussion

The purpose of the parallel ray experiment was to investigate if Fresnel outcoupled light, refracted as parallel rays along a quartz plate surface, had an antifouling effect. A fouling layer with increased fouling thickness was observed, when a ceramic knife was placed in contact with a quartz plate, between the source and the observed thicker fouling layer. Areas not shadowed by the knife, but at the same distance from the source, had less fouling compared to the area behind the knife. This result indicates that parallel rays have an antifouling effect.

An experiment was run in parallel without a ceramic blade in contact with the quartz plate, the non-knife experiment. The non-knife experiment did not stay completely clean, nor completely fouled, which tells that parallel rays are not the only antifouling causing light extraction mechanism affecting the fouling layer in this experiment. The fouling patterns of the knife and non-knife experiment appeared with fouling fringes, much like the fouling pattern of the scattering experiment, and this again suggests Fresnel outcoupling to be an antifouling causing light extraction mechanism.

A LT iteration process was started to correlate the fouling pattern, without a knife, with the observed fouling pattern. The fouling pattern was found to correlate relatively well with the final irradiance graph. The irradiance peaks are correlated with the fouling fringes in periodicity and width when the MFP value of the HG bulk scattering model is once again increased from the initial modeled MFP value. A MFP value of 20,000 mm was found to best correlate the fouling pattern with the irradiance pattern, and this suggests that the quartz plate has a higher quartz quality than the quartz rods. The MFP value of 20,000 mm is 8 times larger than the MFP value found to correlate the fouling pattern of the quartz rod with their irradiance patterns, but it is still 2.5 times smaller than the first approximation done from the scattering coefficient provided by Schröder et al. in Figure 2.3.

Therefore, in this experiment, both parallel rays and Fresnel outcoupling were indicated, as well as scattering, to be an antifouling causing light extraction mechanisms.

The LT irradiance pattern in Figure 5.6 indicates that the irradiance level close to the source is drowned by 'background radiated' light, extracted via scattering, and could explain why fouling fringes are not seen all over the quartz plate surface, but only further away from the source. There should be a clean area directly in front of the LED source, according to the irradiance pattern, but it is believed to have become fouled due to the reported broken down LEDs, 5-48 hours before it was discovered and the experiment was aborted. 5-48 hours is a time that would allow the formation of a visible biofilm. Although, the irradiance level of the irradiance peaks far away from the source is according to the simulation, below the irradiance value of $2 \cdot 10^{-10}$ W/mm^2 which is a value, according to the LT scattering experiment simulations, that clearly would result in a fouled area. This observation suggests that the LT model is not complete.

However, we suggest that parallel rays are continuously emitted from each internal reflection inside the quartz plate, seen as fringes in the fouling pattern on the outside of the quartz plate, and each parallel ray emitting fringe contributes to the antifouling effect 10-20 mm in front of each fringe. The increased fouling, seen behind the ceramic knife, is therefore believed to be caused by blocking the refracted light from the previous 2-3 fringes closest to the knife.

Chapter 6

Evanescent wave experiment

The following chapter contains method, result, and discussion, related to the evanescent wave experiment. The purpose of the evanescent wave experiment was to investigate if an evanescent wave has an antifouling effect on the outer surface of quartz waveguides in contact with aquarium water. The experiment will suppress the mechanisms evanescent wave and parallel rays, but enable scattering and Fresnel outcoupling. The samples consist of one quartz tube experiment (which suppresses the evanescent wave and parallel rays), one 800 mm quartz rod experiment (similar to the scattering experiment, but a longer quartz rod length), and a reference sample without a LED source.

6.1 Method

6.1.1 Immersion

The samples were placed in a horizontal position in the aquarium roughly 150 mm below the surface, attached at the ends by PVC wires. The samples were immersed for 45 and 40 days and had an optical output power of 2.0 mW.

6.1.2 Fouling pattern analysis

The fouling patterns were analyzed in a similar way mention in Chapter 4.

6.1.3 LightTools Simulations

The same quartz material and LED source as used in the scattering experiment, found in Chapter 4, was used to model the experiment.

The LED had optical power of 2.0 mW. The detector had 1 bin in the y-direction and 800 bins in the x-direction, placed 1 μm above either the quartz tube or quartz rod surface. 20,000,000 rays were used in the Monte Carlo simulation.

More detailed information about the LightTools models can be found in Appendix B.

6.1.4 Numerical calculations for a frustrated system

The amount of transmitted power was calculated for a frustrated system based on the theory found in Section 2.5. Both the distance between 'waveguide - fouling organism' was swept from $0 < d < d/1.6\lambda$, and the angle of incidence ($\theta_c < \theta_i < \pi/2$) for a fixed distance, $d = 50$ nm. The fouling organism was assumed to be E.coli bacterium with a refractive index of 1.45 in relation to $\lambda = 275$ nm. It was also assumed that the intermediate conditioning layer does not absorb any light, and has the same refractive index as salt water ($n_{water} = 1.366$). Calculations and MATLAB code can be found in Appendix D.

6.2 Results

6.2.1 Fouling pattern

The fouling patterns of the two quartz experiments are compared. One Ø15 mm quartz tube (with a Ø10 mm quart rod inside), and one Ø10 mm quartz rod, both with a length of 800 mm. Both of the experiments had sedimentation on the outer most quartz surface facing upwards in relation to the aquaria. The rods were found to be completely clean closest to the source, seen on the right side of the images in Figure 6.1 and 6.2. The Ø15 mm quartz tube experiment had a 106 mm clean length, from the source, and the Ø10 mm quartz rod experiment had a 405 mm clean length. Values are found in Table 6.1. The Ø10 mm quartz rod experiment also had a clean length of 55 mm, close to the end-side. The fouling pattern on both of the rods had no traces of fringes, nor a distinct gradient in fouling thickness over distance from the source. The reference rod, seen in Figure 6.3 is heavily fouled. Seaweed and settled hard macrofoulers were observed.

Evanescent wave experiment	Ø15 mm, Quartz tube	Ø10 mm, Quartz rod	Reference
Clean length, from source (mm)	106	405	0
Clean length, from end-side (mm)	-	55	0

Table 6.1: Values from measured clean lengths from the source and end-side side are presented. The total quartz length for each sample was 800 mm.

(a) Unrinsed sample

(b) Rinsed sample

(c) Rinsed, closeup of end-side

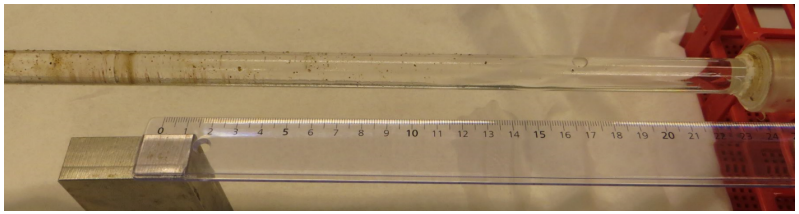

(d) Rinsed, closeup of source side

Figure 6.1: The Ø15 mm quartz tube experiment after 45 days of immersion where the source had an optical power of 2 mW. The source is seen to the right in the images, with a completely clean length closest to the source that becomes fouled in a fast transition further away from the source. In the transition area, a few speckles of fouling are seen. The sample was placed in a horizontal position, roughly 150 mm below the surface and the quartz tube measured 800 mm in length.

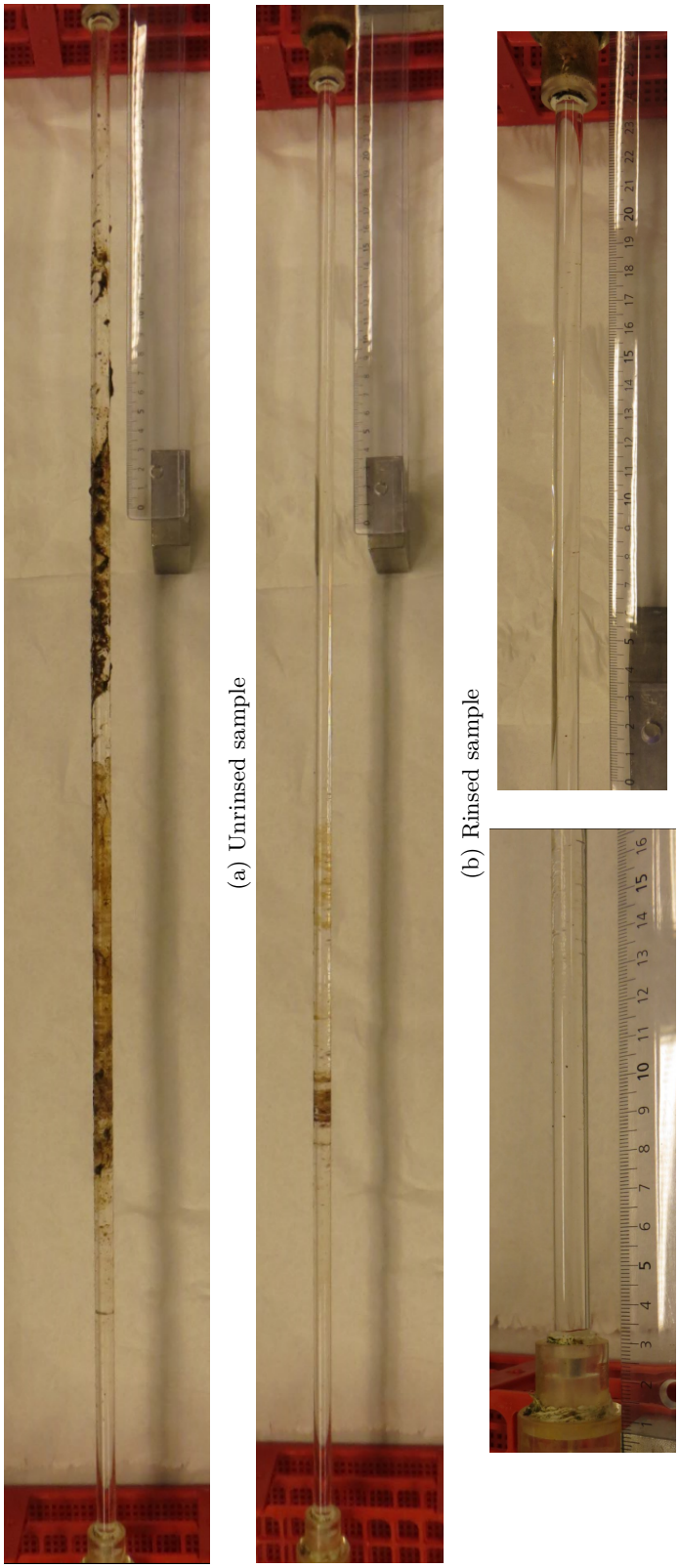

(a) Unrinsed sample (b) Rinsed sample (c) Rinsed, closeup of end-side (d) Rinsed, closeup of source side

Figure 6.2: The Ø10 mm quartz rod experiment after 40 days of immersion where the source had an optical power of 2 mW. The source is seen to the right in the images, a completely clean length is seen closest to the source that after 400 mm rapidly becomes fouled. Also, a completely clean length of 55 mm was observed close to the end-side, seen in Figure 6.2c. The sample was placed in a horizontal position, roughly 150 mm below the surface and the quartz rod measured 800 mm in length.

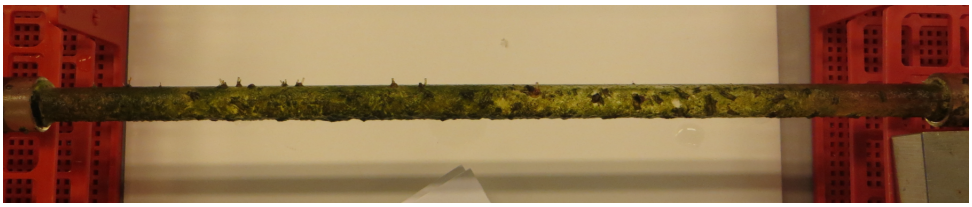

Figure 6.3: The rinsed reference rod was heavily fouled after 45 days of immersion. Seaweed and settled hard macrofoulers were observed. The rod was placed in a horizontal position roughly 200 mm below the surface. Note that the reference rod was only 350 mm long, and 10 mm in diameter.

6.2.2 LightTools results and predictions

The following irradiance graphs are from the LT models created to correlate the irradiance pattern with the experimental results, i.e. the fouling patterns. The LT models for the evanescent wave experimental series used the same parameters as determined for the LT scattering experimental series since its LT irradiance graph was regarded as a close correlation with its fouling pattern. Therefore, the quartz material had a MFP $= 2,500$ mm and is presented as 'output' from the LT iteration process, summarized in table 4.3.

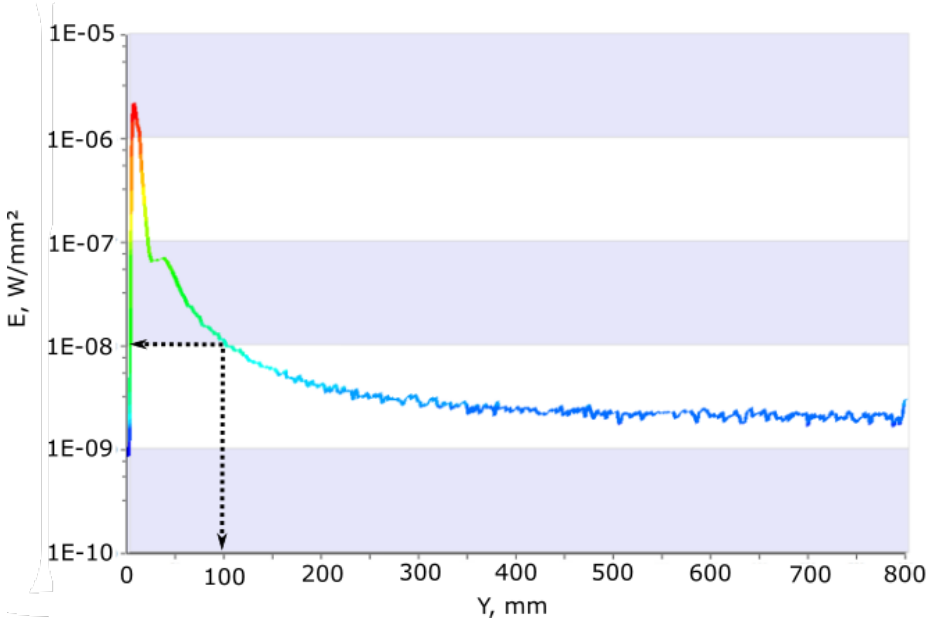

Figure 6.4: A 2-dimensional irradiance graph is seen over the **Ø15 mm quartz tube** experiment. The quartz material is the same as for the scattering experiment with a MFP of 2,500 mm and a g-parameter of 0.85. The irradiance curve has a value above $1 \cdot 10^{-8}$ W/mm^2 for $y = 0 : 100$ mm.

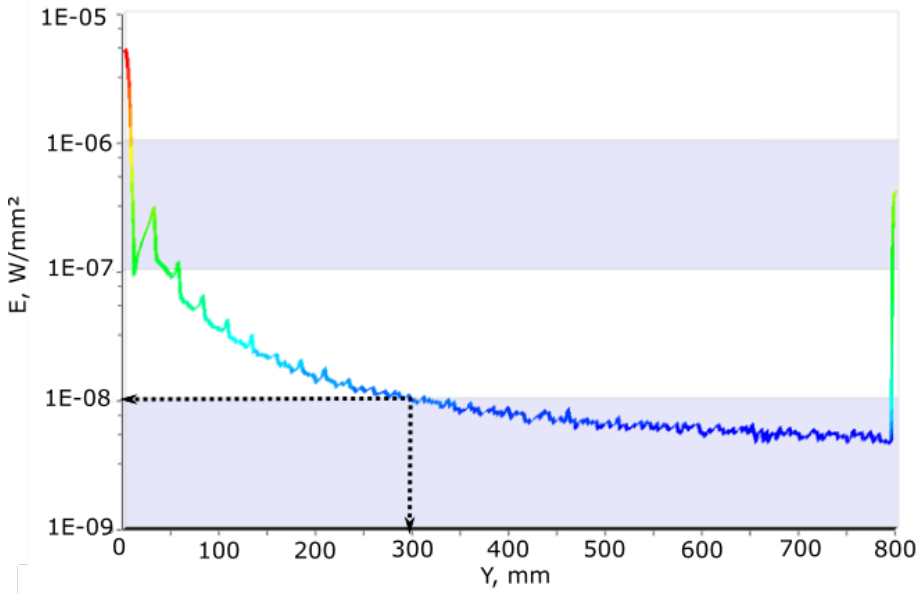

Figure 6.5: A 2-dimensional irradiance graph is seen over the **800 mm long, Ø10 mm quartz rod** experiment. The quartz material is the same as for the scattering experiment with a MFP of 2,500 mm and a g-parameter of 0.85. The irradiance curve has a value above $1 \cdot 10^{-8}$ W/mm^2 for $y = 0 : 300$ mm, with small additional irradiance peaks, seen in the curve between $y = 30$ and $y = 240$.

Interpretation

The same parameters of the LT model, used for the scattering LT model were used for this simulation, because it was regarded as such a close fit to reality, and the quartz rods used in both of the experiment were of the same quality as the Ø10 mm quartz rod of the scattering experiment. When an irradiance threshold level of $1 \cdot 10^{-8}$ W/mm^2 was regarded the quartz tube experiment, where only light extracted via scattering and Fresnel outcoupling was possible, matched perfectly with the observed clean length of the fouling pattern (100 mm).

When one looks at the irradiance graph belonging to the Ø10 mm quartz rod experiment, the same model fails to explain the fouling pattern. The irradiance graph rather suggests a clean length of 300 mm, a 33% reduction compared to the actual fouling pattern (400 mm), which was not the case in the scattering experiment.

The biggest difference when the 350 mm quartz rod of the scattering experiment is compared to the 800 mm, is the optical power. The optical power of the 800 mm quartz rod was roughly 10 times bigger (2 mW vs 0.2 mW). How sensitive the antifouling effect of the evanescent wave is, can be understood when regarding the graphs in Figure 2.5. An adhered conditioning layer to the quartz rod surface of roughly 70 nm would decrease the possible transmitted power due to FTIR with roughly 50% compared to a surface without a conditioning layer. Thus, it may be that the evanescent wave of the scattering experiment was not powerful enough to contribute significantly to the antifouling effect and the LT model fitted perfectly since it does not include electromagnetic optics. As of now, the optical power is 10 times larger, the evanescent wave may affect the settled fouling organisms and, therefore, the LT model does not fit.

The LT-simulations and the resulting irradiance graph also failed to explain the clean length observed from the opposite side of the source, a 55 mm clean length. Even though the end-surface of the quartz rod was partially reflected in the LT simulations. This indicates that only ray optics cannot fully explain the result. As the previously forward directed light would now back-reflected, the angle of incidence changes since the quartz rod end surface is not perfectly smooth. With enough optical power, and correct angle of incidence, the evanescent wave will be able to affect

fouling organisms settled on the quartz waveguide surface even if the light is rather back-reflected. The 55 mm clean length could be explained by the evanescent wave if there was enough optical power remaining, when the light was reflected.

The previously successful LT model fails to explain the observed clean length of the 800 mm quartz rod experiment, even though the model was such a close fit to reality in the quartz tube experiment where the light extraction scattering and Fresnel outcoupling took place.

This was expected if the evanescent wave would have an antifouling effect since the LT program is unable to include, and model for, electromagnetic optics. One explanation to the increased antifouling length of the quartz rod experiment is therefore the antifouling effect of an evanescent wave, on the outside surface of the quartz rod. Although, if the irradiance pattern of Figure 6.5 is regarded, an irradiance threshold value of $0.7 \cdot 10^{-8}$ W/mm^2 would also explain a clean length of 400 mm.

6.2.3 FTIR related to fouling based on calculations from Appendix D

Numerical calculation of FTIR was done to regard how the amount of transmitted optical power depend on various conditions. The equations found above, in section 2.5 were used. The entire solution is found in Appendix D.

The fouling organism modeled is imagined to be a bacteria, with a diameter of 1 μm and a cell membrane thickness of roughly 5 nm [29], settled on the waveguide surface, with an intermediate conditioning layer of 50 nm [20], part of the evanescent wave could reach past the cell's membrane and into the cell. The refractive index of Escherichia coli cells (E.coli bacteria) is approximated to $n_{E.coli} = 1.45$ for $\lambda = 275$ nm and $n_{water} = 1.366$ using [30].

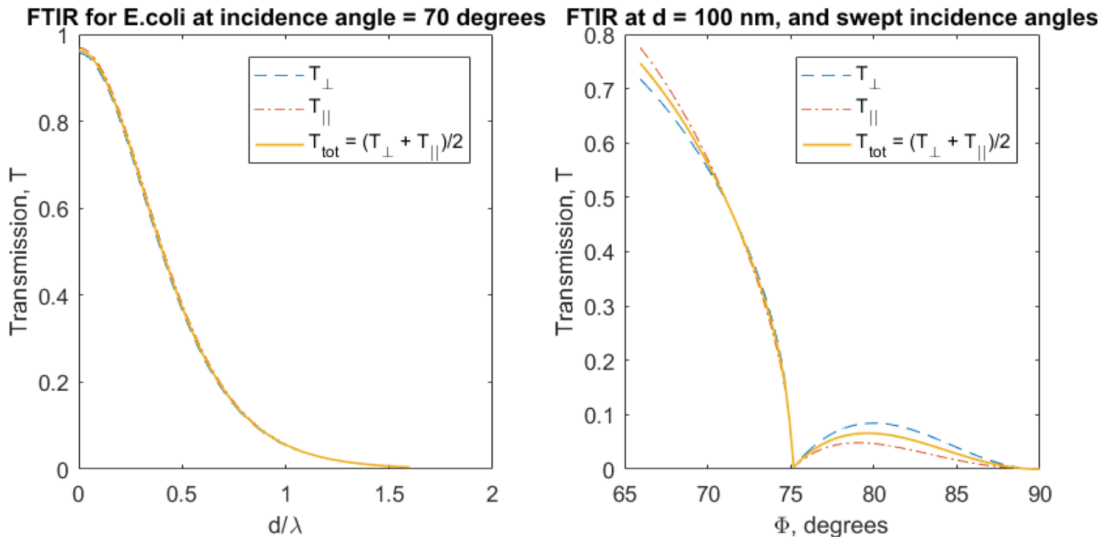

Figure 6.6: The left graph shows the amount of transmission, proportional to the irradiance of the quartz waveguide surface ($n_{quartz} = 1.496$), as the fouling organism, here E.coli bacterium ($n_{E.coli} = 1.45$), moves closer to the surface. The light has an incidence angle of 70° ($\theta_c = 65.94°$). It is assumed that the intermediate conditioning layer does not absorb any light and has the same refractive index as salt water ($n_{water} = 1.366$). The right graph displays the amount of transmitted optical power proportional to the irradiance of the quartz waveguide surface, when a conditioning layer with a thickness of $d = 100$ nm is assumed, and the angle of incidence is swept from θ_c to $\pi/2$. The graphs display the transmission for both polarization directions where the yellow graph displays the sum of the two. $\lambda_0 = 275$ nm was used.

In the right graph of Figure 6.6, the transmission components $\alpha_\perp$, $\beta_\perp$, $\alpha_\parallel$, and $\beta_\parallel$ become complex when $\theta_i > 75°$ which is due to the refractive index relation, $n \equiv (n_3/n_1) < 1$ when $n_3 < n_1$. It is unclear how the imaginary part should be interpreted. When considering the example, seen in Figure 2.7, n was equal to 1.

The result in the left graph in Figure 6.6 indicates that the amount of transmitted optical power over a large distance from the surface could cause an antifouling effect. At $d = 50$ nm, $T = 0.82$ ($\theta_i = 70°$). This indicates that the evanescent wave indeed could cause an antifouling effect. That is when the required conditions are met and there is enough optical power inside the waveguide. Although, when distance, d, and θ_i are swept simultaneously, the power falls off quickly.

6.3 Discussion

The purpose of the evanescent wave experiment was to investigate the antifouling effect of an evanescent wave by eliminating its presence and comparing the antifouling pattern with an unmodified experiment. Two experiments were conducted, one 800 mm long quartz rod experiment, where all of the posed light extraction mechanisms could affect the fouling pattern, and one 800 mm long quartz tube experiment, where evanescent waves and parallel rays were suppressed from affecting the fouling pattern.

The fouling pattern of the quartz tube experiment, where the combination of the extraction mechanisms - the 'package' (evanescent wave and parallel rays) was ruled out, completely correlated with the LT irradiance graph when an irradiance level of $1 \cdot 10^{-8}$ W/mm^2 was regarded. This model was based on the same parameters determined for the LT scattering experiment model. Note that the LT model had the same parameters that were determined to correlate with the fouling pattern of the scattering experiment, and that LT is only able to model geometrical optics, meaning scattering and Fresnel outcoupling. Some irradiance peaks, caused by the Fresnel outcoupled light, can be seen in the irradiance curve of the 800 mm quartz rod experiment in Figure 6.4, but the shape of the slope is mainly attributed to light extraction via scattering that was strongly indicated by the close match between LT predictions and fouling pattern. It is not clear why no irradiance peaks, attributed to the Fresnel outcoupled light, appears in the irradiance pattern of the quartz tube experiment. Also, no fringes are seen in the fouling pattern.

When the same LT model is used for the 800 mm quartz rod experiment, in an attempt to correlate the fouling pattern with the irradiance graph, it is 33% off in regards to the prediction of the clean length when an irradiance value of $1 \cdot 10^{-8}$ W/mm^2 is regarded. The LT model also fails to explain the 55 mm clean length observed on opposite side from the source. The increased clean length from the source side, 400 mm instead of 300 mm as expected, could be explained by regarding a relatively minor change such as an irradiance threshold level of $0.7 \cdot 10^{-8}$ W/mm^2 or a +30% light output. Yet, the LT model fails to explain the clean length from opposite to the source side, even with a decreased irradiance threshold value.

Comparing the two fouling patterns and their respective clean lengths, where the two extraction mechanisms the evanescent wave and the parallel rays were present (the quartz rod experiment) an increased clean length was seen, not explainable by LightTools. This indicates that the package, the combination of the light extraction mechanisms, may have an antifouling effect.

Which of the two mechanisms are behind the observed increase in clean length, or their individual contribution, cannot be deduced from the experiment. When designing the experiment the parallel rays were not believed to compete with the evanescent wave, but results from the parallel ray experiment suggests that parallel rays are refracted in a periodic manner from the internally reflected light and will therefore also be present along the entire quartz rod surface, along with an evanescent wave.

Therefore, in this experiment, the combined antifouling effect of parallel rays and the evanescent wave is indicated, as well as scattering, to be an antifouling causing light extraction mechanisms.

Since the combination of the two light extraction mechanisms cannot be separated, there is no direct proof that the evanescent wave is an antifouling causing light extraction mechanism in itself and the arguments remain theoretical. Numerical calculations of frustrated total internal reflection were done in MATLAB to determine if an evanescent wave could explain the increased clean length. The result is seen in Figure 6.6, where the transmission for a frustrated system by a fouling organism is shown. When the different polarization contributions are added together, the transmission is 0.96 for an incidence angle of 70° and a distance of $d = 0$ nm between the waveguide surface and frustrating object.

A distance of 0 nm between fouling organism and the waveguide surface, should be regarded as unlikely due to the adhered conditioning layer. A SEM analysis of a completely clean quartz surface after 6 weeks of immersion, mentioned in Appendix E was done to investigate the surface on the micro to nanoscale. An unknown material was seen on the otherwise visible clean surface (no settled organisms), seen in Figure E.2b, that indicates the presence of a conditioning layer. A conditioning layer is suggested, by literature, to have a thickness of roughly 70 nm. If this material is always present between the quartz surface and settled fouling organisms, transmission will be greatly reduced. Although, the evanescent wave, at a distance of 100 nm from the waveguide surface, and an angle of incidence from the critical angle to 74°, has a transmission of 0.75 to 0.28 if an intermediate layer is not absorbing any light.

The above arguments, the numerical calculations and the investigation of the conditioning layer with a SEM, are all arguments suggesting the evanescent wave is an antifouling effect to be considered. Meaning, the evanescent wave should be present on the outside surface of a waveguide affecting settling fouling organisms.

Chapter 7

Summary

A thorough investigation has been done to study the optical principles of UV-based antifouling. Experiments and simulations have been performed to study the role of specific light extraction mechanism's antifouling effect.

The scattering experiments indicate that scattering and Fresnel outcoupling affect the fouling pattern. The parallel ray experiments indicate that refracted rays, parallel to the surface may have an antifouling effect. This was seen when a ceramic knife was placed on top of a quartz plate creating a shadowed area resulting in a difference in the fouling thickness seen behind the knife compared to areas not shadowed by the knife. Lastly, the evanescent wave experiment indicates that scattering once again is an antifouling causing light extraction mechanisms by strongly matching the LT model when the combination of the evanescent wave and parallel rays is suppressed. Once the quartz tube is removed, a much longer clean length is achieved than predicted by the LT model which indicates the antifouling effect of the package, the evanescent wave and parallel rays together.

An irradiance threshold value of $1 \cdot 10^{-8}$ W/mm^2, proposed by independent research, is always assumed when the fouling pattern of the experiments is compared against the LT predictions. In the scattering experiment and the quartz tube experiment, as part of the evanescent wave experiment, the irradiance graphs correlate almost perfectly with the fouling pattern when this irradiance threshold value is used. The fluorescent microscopy investigation indicates the correctness of irradiance threshold level. Very few fouling organisms were observed directly in front of the source, and the single bacteria at the location of the expected threshold, in Figure 4.8, point toward the argued irradiance threshold value. These combined results indicate that the irradiance threshold is close to $1 \cdot 10^{-8}$ W/mm^2, in agreement with references.

The extensive LT iteration helped to find a value representing the quartz quality and model parameters. The irradiance pattern could not have been achieved without scattering, and Fresnel outcoupling, and the MFP value was necessary for a correct correlation between the irradiance graph and fouling pattern and came to represent the quartz quality of the samples when a g-parameter of 0.85 was used with LightTools Henyey-Greenstein scattering model.

The final table is obtained once the results from all of the experiments are combined.

Scattering	Strongly indicated since scattering is the main parameter needed to correlate LT simulations with observed fouling pattern in all of the experiments.
Parallel rays	Indicated in the parallel ray experiment when thicker fouling is observed behind the ceramic knife compared to area not shadowed by the knife.
Evanescent wave	Suggested, in combination with parallel rays to explain the observed fouling pattern of the quartz rod sample in the evanescent wave experiment since only the LT simulations, based on ray optics, failed to do this.
Fresnel outcoupling	Strongly indicated in most of the resulting fouling patterns by fouling-fringes in the fouling pattern.

Table 7.1: Summarizing all the experimental results for each of the examined antifouling causing light extraction mechanisms.

The fringe-like fouling patterns observed in many of the experiments, were earlier believed to be solely explained by Fresnel outcoupled light. Numerical calculations, presented in section 4.2.4 with calculations found in Appendix C, showed that only a small fraction of the total power had the required conditions, with a narrow range of a few incidence angles, to both refract and reflect light periodically. The reflected power is also highest, closest to the critical angle. It is therefore believed that such a small amount of optical power cannot explain the wide fouling fringes on its own. What is interesting is that the penetration depth of the theoretical evanescent wave is the biggest, close to, and after the critical angle, and the parallel rays are emitted, just before the critical angle. Instead of only explaining the fringes with Fresnel outcoupled light, all the light extraction mechanisms are believed to contribute to the suppressed fouling, observed in each fringe, highlighting the interplay and complexity of the initially asked question - "What are the exact antifouling causing light extraction mechanisms for UVC light in quartz?"

7.1 Conclusion

In this work it is strongly indicated that scattering is an important antifouling causing light extraction mechanism and the irradiance threshold value correlates with an irradiance of $1 \cdot 10^{-8}$ W/mm^2 for $\lambda_0 = 275$ nm that has been found in previous studies to be the threshold for an antifouling effect. The results also indicate an antifouling effect of parallel rays and Fresnel outcoupling. The antifouling effect of an evanescent wave remains undecided. It is concluded that none of the proposed antifouling causing light extraction mechanisms can definitely be ruled out.

Chapter 8

Outlook

After eight months of research, it is satisfying to have reached a compelling conclusion by results that were both surprising and insightful. Being as objective as possible, I am more convinced now, than before starting this project, that a UV-based AF solution for ship hulls is the best, and closest to the ideal solution (definition of the 'ideal solution' is found in [31]), currently researched globally.

UVC light as an antifouling solution is still a very novel research field with few publications related to it. As both industry and academia realize the potential of this solution, the number of publications and awareness will take off in the near future. It is my wish as a researcher, and author, to point out the most interesting new questions that arose from working with this project, and possible continuation and improvements of my research, for fellow peers and colleagues to pick up. These questions, suggestions, and thoughts, can be found in the list below.

Improve the LightTools model

- The LT models can be done more accurately. The biggest improvement will come from modeling the different sources correctly. Because the UVC sources used in the experiment are still new to the market, they have not yet been modeled in great detail in LT.
- Create a more scientifically backed-up volume scattering model for the quartz material in LT. By using the available Henyey-Greenstein scattering model, alter the g-parameter and MFP to obtain the same scattering profile as described by Rayleigh scattering. The uncertainty in the model will be the quartz quality, which different values of the MFP will account for.
- Lastly, surface scattering was never taken into the scattering model, due to lack of time. Investigate if, by modeling this, the visible light measurement can better correlate with the MFP output value discovered to explain the observed fouling pattern on the quartz waveguide surfaces.

Determine the origin of the fouling-fringes

The observed fouling fringes of the scattering experiment in particular, correlate well with the LT model but raise a few questions. The measured width of the fringes, and the observed fouling gradient in the fringes, question where the light originates from. Is the fouling gradient caused by the light just before the critical angle, that is refracted, or is some of the AF effect caused by parallel rays and evanescent waves, originating from close to the critical angle or after? Develop an, as accurate as possible, numerical model to find out. A numerical model will help interpret what happens at each surface interaction, or reflection, and can combine all of the theories including the theory explaining the evanescent wave.

The proportion of the total optical power for each light extraction mechanism

It is concluded in this thesis that all of the posed light extraction mechanisms contribute to the observed antifouling effect. However, it is unknown how much of the total radiated power each of light extraction mechanisms contributes to the antifouling effect. It is key to answering this question to decide which extraction mechanism one should enable, or enhance, in a product design, for an as energy efficient solution as possible. When the evanescent wave experiment is considered, a 30% longer, clean length appeared, compared to the predicted result, explained by the LightTools model. Because of the unexpected result, the evanescent wave will be interesting to study in more detail.

Confirm the Evanescent wave experiment

Since the antifouling effect of an evanescent wave indicates a potentially huge efficiency increase, the previous experiment should be repeated to confirm the result. This time, the samples should be placed in a vertical position to avoid debris falling onto the quartz surface and potentially affecting the result.

Investigate the thickness of the conditioning layer

Research related to the conditioning layer is incomplete and invaluable when it comes to future numerical calculations for the evanescent wave. First, investigate the layer thickness of the conditioning film on quartz. One quick and easy method is to measure the step height with an AFM, after scratching part of it and covering it with a metallic coating. Complement the research by investigating the film thickness of different UVC-transparent materials, kept clean by direct lit UVC, and immersed in different oceanic conditions, similar to the configuration found in Appendix E.

Fight or fly - A fouling organisms behavior towards UVC light

A very interesting question that arose during the project was if any of the fouling organisms can sense the light and its hazardous effect, and therefore choose not to settle on a UVC emitting surface. An article by Schuergers et.al. from 2016, concluded that one specie of cyanobacteria use micro-optics to sense light direction [32]. One can also invert the question - Are fouling organisms attracted by the light, and later killed by the wavelength? Much like a light source attracts flying insects in a rainforest at night.

The author's final thoughts

The following thoughts are author's alone. They should be regarded as optimistic thoughts and ideas, revealing future opportunities, instead of facts. The purpose of sharing these ideas is for peers and industries to realize the potential in a UV-based AF method.

UV-based AF is a research field in its infancy, and I look forward to seeing its potential being realized. As the area of research gets more attention in the future, the industry will wake up and dare to take more risks. UVC LED development is predicted to follow the same trend as visible LEDs did when they were first introduced to the market. Lower price, better efficiency and longer lifetime, are all improvements today's UVC sources would benefit from. It is also essential that the UVC LEDs come with different light cones, for instance, side emitting LEDs instead of top emitting, for more options in a design perspective.

For the research field to become more available for academia and smaller business, it is essential the infrastructure and tools surrounding the technology become cheaper and more accessible. UVC lasers, with the specific germicidal wavelength, are needed to study material properties like scattering more accurately. Camera systems, with appropriate lenses, enable accurate irradiance characterization for different experimental designs. A larger variety of sensors such as integrating spheres more sensitive to UVC light, are needed to better measure the absolute power. An opportunity with this novel field is that much research has to be done regarding the light-material interaction for the wavelength around $\lambda = 275$ nm. Some interesting questions are: What is the refractive index for fouling organisms for this wavelength, and what is the UVC's behavior in different UV-transparent materials?

As previously stated, enabling a UV based AF method will offer the first, completely fouling free surfaces, on ship hulls during their entire docking cycle. This realization will offer new opportunities for both the industry and shippers. M.P. Schultz, famous for his investigation of increased drag on U.S Destroyers [3], spoke in his talk *Impact & Application of marine fouling and corrosion research and technologies* on ICMCF 2016, about AF solutions ultimate goal of "closing the gap" between drag caused by marine growth on ship hulls, and the drag induced by a completely clean, and smooth, steel surface. I would state that we have to think bigger than this. We have to think about 'going beyond the gap'.

A completely clean surface will enable researchers to focus on the drag induced by the smooth surface, instead of caused by fouling. Since the surface will stay clean over time, one can now regard biomimicry in a greater extent, and consider changing the surface topography to decrease drag. Some research consists in the area where sharks and their skin often act as a model organism because of their fast and efficient swimming and their fouling free skin. When seen under the microscope the shark skin is found to have different riblet-like structures, on top of the denticles, aligned in the direction of the flow, thereby reducing the frictional drag, with a maximum drag reduction of 10% [33]. With my insight in the nanoscience, printing nano-topographies is possible, but it is naive to think that small patterns in the nano-regime will be able to withstand the large forces experienced by the blasting ocean onto a ship's surface. It is more reasonable to consider microtopographies, which coincide nicely with the detail size of the riblets, found on the shark dendrites. Patterns in this regime could easily be cast, or pressed, from a 3D printed master. Which is possible because the concept of developing a UV emitting film, relies on UV transparent silicone. When one is considering the durability of a micropattern in silicone, one could think of today's silicone based coatings and their shedding speed. As a reference, Self-polishing copolymers are designed to have a release rate of 5 - 20 μm a year [34].

By 3D printing different masters for the silicone casting process, it will be easy to customize the surface topography according to various sections of a ship's hull. This could open up an entirely new market for today's coating companies. Now, they will be able to offer their customers an entire range of products where the initial product being a smooth surface gives a 0% drag penalty. The additional products will be more customized for the unique ship hulls with drag reducing surface topographies, offering more complexity, for more fuel savings, by decreasing a vessels drag even further, by going beyond the gap.

Appendix A

Quartz characterization

In the following appendix the material characterization method and results for the four quartz rods, used in the scattering experimental series, are presented.

Purpose

To characterize the absolute power $[W]$ extracted via the quartz rod end- and cylindrical surface using an integrated sphere, IS, and to determine the quartz's bulk scattering property, i.e the MFP [mm] for the HG scattering model (g = 0.85) using LightTools. The amount of light extraction via scattering for UVC light, with a peak wavelength of $\lambda_p = 275$ nm, is then calculated to predict the antifouling behavior, and fouling free length, for each sample.

Material

Two different quartz rod diameters, two samples for each diameter, were examined. The quartz rods, Ø10 mm, were 350 mm long, had hazy quartz rod ends due to being cut with a diamond blade cutter, and distinct material impurities, seen as scattering sites when white light was coupled into the rods. The cylindrical quartz rod surfaces were also observed as lightly scratched.

The quartz rods, Ø12 mm, were cut in 350 mm lengths (+/- 1 mm) with a glass rod cutter. The quartz rod ends were regarded as optical smooth, and the rods appeared as almost completely clear when visible light was coupled into them. The cylindrical surfaces had no distinct scratches.

The visible light used was a fiber optics lamp with a peak wavelength of $\lambda_p = 620$ nm. The lamp had various power settings. The two power settings used in the experiment had an optical power of roughly 15.6 and 228 mW.

The absolute optical power was measured with an integrating sphere, measuring 20 inches (50.8 *cm*) in diameter, model name AS-02478-000, LMS-200. The lamp power supply was LPS-100-0278 and detector CDS 2100. All the equipment was from *labsphere*. The software used to run the setup and analyze the data was called *LightmtrX*

LightTools was used for optical ray simulations.

Method

The quartz rods were cleaned with *IPA* before the characterization. The inside of the integrated sphere, IS, was prepared with a plastic stand. The calibration lamp was turned on and lit for five minutes before a calibration measurement was taken. A small circular opening in the side of the IS was opened, and the fiber lamp was directed into the IS. A new measurement was taken (P_{in}). The quartz rod was inserted through the circular opening. The rod was suspended with a clamp on the outside of the IS and rested on the plastic stand on the inside of the IS. A new calibration measurement was taken. The fiber lamp was coupled to the quartz rod end surface, outside of the IS. A new measurement was taken (P_{out}). The quartz rod end, inside the IS, was capped, dressed on the inside with a black light absorbing material. A new calibration measurement was taken,

followed by a final measurement (P_s). The exposure time was adjusted for each new measurement with the goal of saturating the sensor with 80%. The number of *scan average* was set to 5. This procedure was repeated for all four rods.

The data was processed in Excel to determine what percentage of the light escapes via the quartz rod cylindrical surface and how much power is reflected from the quartz rod end surfaces. These calculated values were inserted in a LT model, and the MFP of the HG scattering model was altered. The MFP was determined when the proportion of the optical power of the white light ($\lambda = 620$ nm) correlated with the IS measurements.

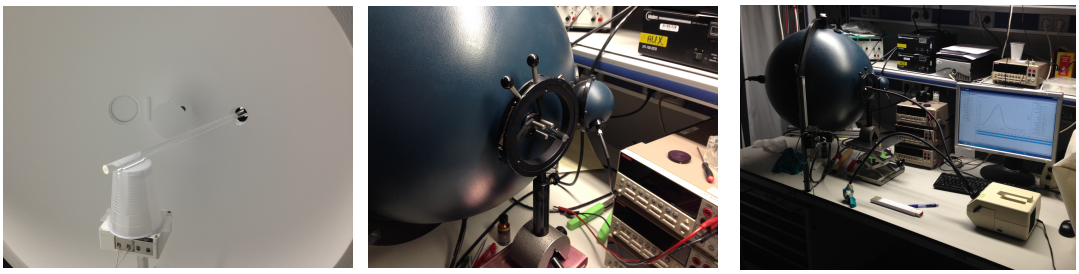

Figure A.1: The experimental setup is displayed. The left image illustrates a quartz rod resting on the plastic stand inside the integrated sphere. The center image depicts the quartz rod inserted through the spherical opening in the integrated sphere. The right image shows an overview of the setup. To the right in the image, the fiber lamp is seen. On the top shelf in the image, the source power supply and detector is seen. To the left, the integrated sphere is seen.

Calculations

The following equations were used to calculate the quartz rod end reflection and part transmission through the cylindrical quartz rod surface. It is assumed that the entire quartz rod length was inside the integrated sphere for measurement and the light absorption is zero in the quartz material.

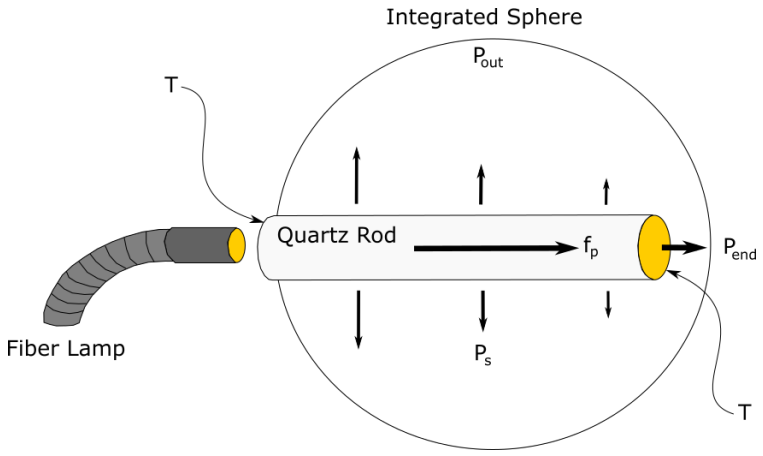

Figure A.2: Depicting the experimental setup. P_{in} is the optical power [W] from the fiber lamp, T is the transmissivity per quartz rod end surface, f_p is the fractional power propagating in the quartz rod before reaching the final end surface, P_s is the measured emitted power, [W], through the quartz rod cylindrical surface, P_{end} is the optical power, [W], escaping via the quartz rod end surface (calculated value) and P_{out} is the combined measured optical power [W], $P_s + P_{end}$. P_s is measured by placing an absorbing end cap over the quartz rod end, therefore removing the power contribution P_{end}.

The percentage power emitted through the cylindrical quartz rod surface is given by

$$Cylindrical surface power = \frac{P_s}{P_{in}}$$

where P_s is the power measured emitted through the cylindrical quartz rod surface and P_{in} is the optical power of the source.

The power emitted through the quartz rod end surface, P_{end} is calculated by the following equation

$$P_{end} = P_{out} - P_s$$

where P_{out} is the combined emitted power from both the cylindrical quartz rod surface and the quartz rod end.

f_p, the fraction of P_{out} that actually comes out of the end cap is calculated by the following equation

$$f_p = \frac{P_{out} - P_s}{P_{out}} = \frac{P_{end}}{P_{out}}$$

To calculate the reflection for the quartz rod end surfaces, the following set of equations are needed. It is assumed that the quartz rod has the same surface reflection for each rod end.

$$P_{in} \cdot T \cdot f_p \cdot T = P_{in} \cdot f_p \cdot T^2 = P_{end} \Leftrightarrow P_{in} \cdot \frac{P_{end}}{P_{out}} \cdot T^2 = P_{end} \Leftrightarrow P_{in} \cdot T^2 = P_{out}$$

where T is the transmission trough each quartz rod end surface. T is derived in the following manner

$$T = \sqrt{\frac{P_{out}}{P_{in}}}$$

The reflection is given by the following equation.

$$R = 1 - T$$

The reflection from a quartz rod end surface is given by the following equation

$$R = 1 - \sqrt{\frac{P_{out}}{P_{in}}}$$

LightTools

A LT model was constructed to alter the mean free path, MFP, of the HG scattering model to obtain the same optical power through the cylindrical surface, as measured in the integrated sphere.

A quartz rod was constructed, 350 mm long and a diameter of either 10 or 12 mm. The quartz material had an refractive index of 1.4574 for $\lambda = 620$ nm. The rod was totally immersed in a cube of air, with a refractive index of 1, and the source had a wavelength of $\lambda = 620$ nm and an optical power of 1 mW. The source was modeled with a 5x5 mm Lambertian emitter with an angular spread of 80°. The cylindrical surface detector was positioned 0.1 mm above the quartz rod surface with 1 bin in x-direction and 350 bins in y-direction. The cylindrical surface of all the rods was modeled as optical smooth with Fresnel losses. The quartz rod ends were also modeled as optical smooth, for all rods, with a surface reflectance, modeled as smooth optical, according to calculated values found in Table A.2.

The quartz material was modeled with the HG scattering model and had a g-parameter of 0.85. The MFP value of the HG scattering model was swept from zero until the recorded fraction of the total power, emitted via the cylindrical surface matched the percentage power emitted through the cylindrical quartz rod surface, measured by the IS.

Once the power was matched, the MFP values were divided by the UVC scattering conversion factor, according to section 2.4.1. By dividing the two scattering coefficients, extracted from the graph seen in Figure A.3, from $\lambda = 275$ nm, $\alpha = 2 \cdot 10^{-4}\ cm^{-1}$ is extracted and from $\lambda = 620$ nm, $\alpha = 6.5 \cdot 10^{-6}\ cm^{-1}$, a value of 31 is calculated by $\alpha_{275}/\alpha_{620} = 2 \cdot 10^{-4}/6.5 \cdot 10^{-6}$. The wavelength of the source was changed to $\lambda = 275$ nm and the ambient medium of the immersed rod was changed to salt water in the LT model, with a refractive index of $n = 1.3540$. The refractive index of quartz was simultaneously changed to 1.496.

Results

The following data is acquired using the integrated sphere.

QR	Diameter, (mm)	Radiant flux (W)			Cyl. Surface measurement	
		Source - P_{in}	Entire rod - P_{out}	Cylindrical surface - P_s	Exposure time (ms)	Sensor saturation (%)
QR10-A	10	1.89E-02*	1.56E-02	8.38E-04	120,000	unknown
QR10-B	10	2.25E-01	1.84E-01	1.13E-02	40,000	49.57
QR12-A	12	2.28E-01	2.04E-01	9.04E-04	70,000	13.50
QR12-B	12	2.22E-01	2.02E-01	1.21E-03	100,000	16.27

Table A.1: The following values were obtained from measuring four different quartz rods in an integrated sphere. *The optical power of the fiber lamp was roughly 10x lower because a different setting was used.

The following values are calculated using the above equations.

Quartz rod	Cylindrical surface power (%)	Reflectance per QR end (%)
QR10-A	4.43	9.15
QR10-B	5.02	9.57
QR12-A	0.40	5.41
QR12-B	0.54	4.61

Table A.2: The following values are calculated from the data in Table A.1 using the above equations.

The following MFP values were determined in order to achieve the same proportion of light extraction via the cylindrical quartz rod surface as was measured using the integrated sphere.

Quartz rod	MFP ($\lambda = 620$ nm)	MFP ($\lambda = 275$ nm)
QR10-A	1950 mm	63 mm
QR10-B	1710 mm	55 mm
QR12-A	19,000 mm	613 mm
QR12-B	13,500 mm	435 mm

Table A.3: The following MFP values for the different quartz rods were obtained using LT's HG scattering model. The central column is the MFP value of when the proportion of the optical power in LT matched the measured value obtained using the IS. The values in the right column, come from when the MFP for $\lambda = 620$ nm is divided with the UVC conversion factor 31.

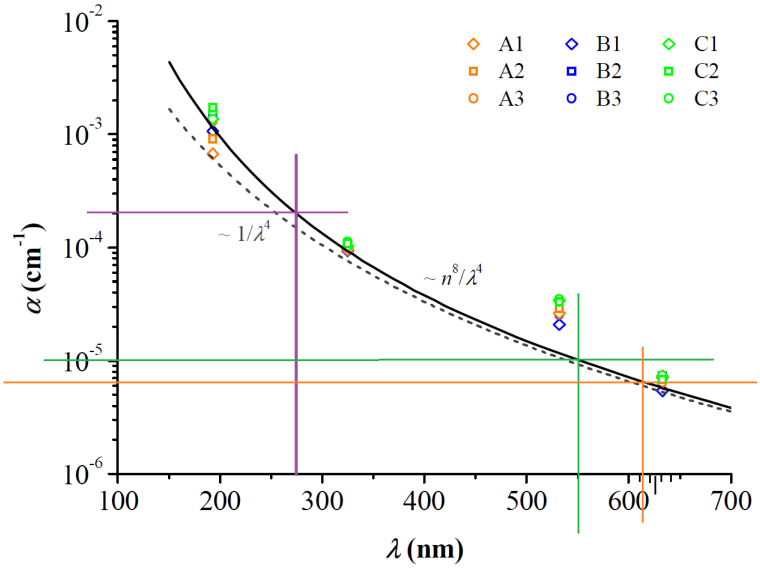

Figure A.3: The Rayleigh scattering for UVC-visible light in fused silica, reproduced from Schröder et al. The two colored lines, orange and violet, mark the different wavelength dependent scattering coefficients (α). The box in the top right corner indicates different material qualities investigated in the paper [12].

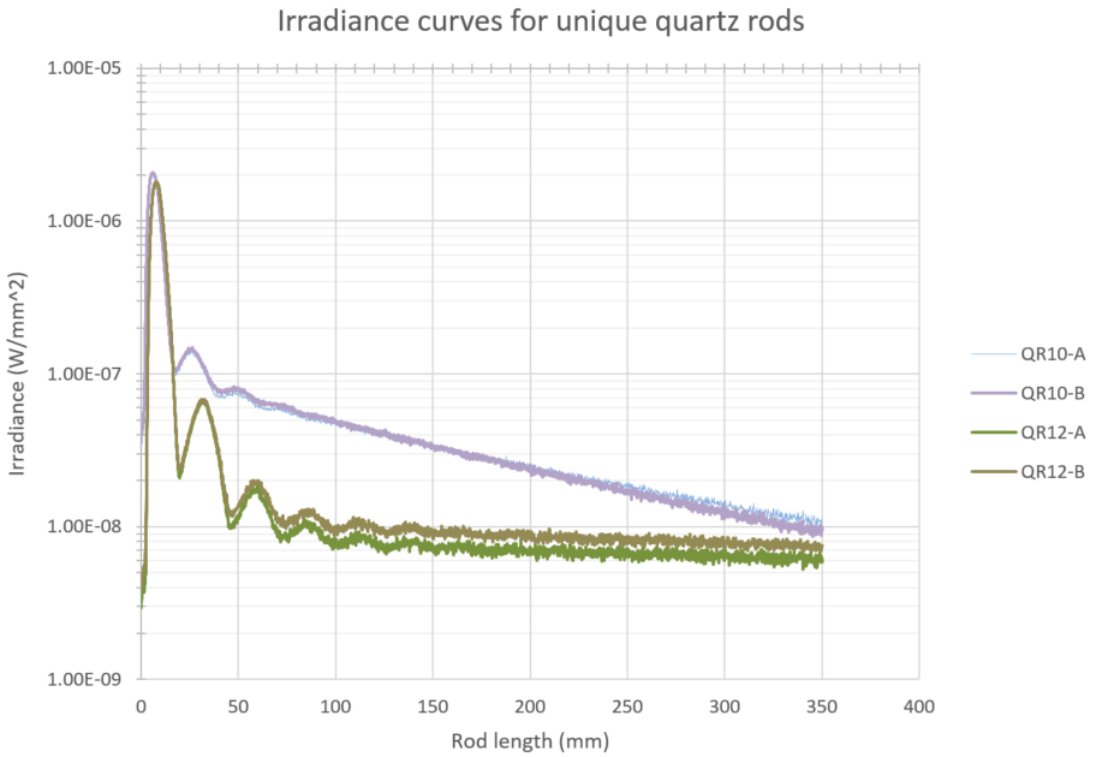

Figure A.4: The following irradiance curves were obtained for the different quartz rods using LightTools for $\lambda = 275$ nm for an optical power of 1 mW.

Appendix B

LightTools models

A more detailed description concerning the construction of the final LightTools models is presented. The purpose is to allow the reader to reproduce the models, and their result.

Scattering experiment

The quartz rods had a diameter of either 10 or 12 mm. They were 350 mm long. The quartz material had a Henyey-Greenstein, HG, scattering model with a g-parameter of 0.85 and a mean free path, MFP, of 2,500 mm. The MFP values 63, 55, 613 and 435 mm determined in the previous Appendix A, were found to not correlate with experimental results. The quartz rod end surfaces were individually characterized, according to Appendix A and had values according to Table B.1. The cylindrical surfaces of the quartz rods had Fresnel losses as optical property. The refractive index of quartz was 1.496.

The source was modeled as a cube, measuring 0.1x0.1x0.01 mm (length, width, height). It was a Lambertian emitter with an angular spread of 85 degrees, with $\lambda = 275$ nm. The source was immersed in an air cavity, 1 mm in front of the quartz rod end surface.

A cylindrical detector surrounded the outside of the cylindrical quartz rod surface and was elevated 1 μm above the quartz rod surface. It had 350 bins in the y-direction (one for each millimeter) and 1 bin in the x-direction. The detector was offset 4 mm in the y-direction only to allow detection after the light absorbing material (see below).

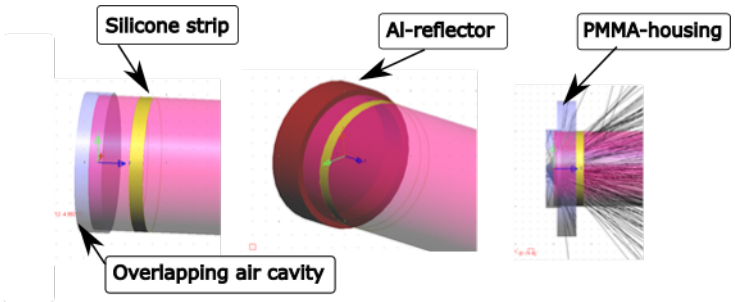

Figure B.1: Different images showing how the scattering experiment was constructed in LT. The text boxes in the images describe the various details that are mentioned in the text.

Quartz Rod	Ø10 mm	Ø12 mm
Optical Power	0.173 mW	0.21 mW
QR end-surface reflectance	9.47 %	4.75 %
$n_{saltwater}$	1.39*	1.395*

Table B.1: The following are unique values for each quartz rod simulated. The optical power was calculated from the known degradation of the LEDs after 1000 hours, in addition to calculations using the current values, read from the power supplies during the experiments. The reflectance for each quartz rod end was individually characterized, see Appendix A. The refractive index of the salt water was adjusted to fit the observed fouling pattern with the irradiance curve, and was done before the refractive index of the aquaria water was numerically calculated. *Different values of $n_{saltwater}$ were tested to better correlate the LightTools irradiance pattern with the observed fouling pattern. Numerical calculations done later, suggest that the refractive index of salt water is 1.366.

The air cavity, which the LED source was suspended in, overlapped with the quartz rod and aluminum reflector, to avoid interface issues with the probabilistic ray simulations.

An aluminum reflector surrounded the air cavity and reached 1 mm onto the quartz rod surface. It had an inner diameter of 4.8 and an outer of 5.5 mm for the Ø10 mm quartz rod. The Al-material was custom made to be accurately wavelength dependent. It had a HG-scattering model with g-parameter of -0.9 and a MFP of 1 mm. The refractive index was 0.20882 for a wavelength of $\lambda = 275$ nm [8]. The optical surface properties were modeled as a simple mirror, with a reflectance of 92.71% and 7.29% absorption.

A PMMA-circle reached around the quartz rod located 0.5 mm from the quartz rod end, with a length of 2.5 mm. The refractive index of PMMA was 1.5425 and the material had 0% in transmission.

The cylindrical quartz rod surface had a totally absorbing strip, 1 mm in height, seen in yellow in Figure B.1. The absorbing strip was totally absorbing and reassembles the silicone glue, used in the practical experiment.

The models were completely immersed in salt water, modeled as totally transmissive with two different refractive indices, found in Table B.1.

Why is scattering required?

It is argued in the results, related to the scattering experiment, seen in section 4.2 that scattering is still required to explain the fouling pattern, and thus the fouling pattern, and the fouling fringes, are not solely explained by Fresnel outcoupling.

In Figure B.2 below, two separate LT simulations of the Ø10 mm quartz rod with an optical power of 0.173 mW. The left image, Figure B.2a shows the irradiance pattern of the QR simulated with HG scattering activated, and a MFP of 55 mm. It can be seen that there are only a few smooth "bumps" in the irradiance graph. These are believed to be caused by the Fresnel outcoupling but becomes smoothed out due to too much scattering. If an irradiance threshold level of $1 \cdot 10^{-8}$ W/mm^2 is considered, two clear areas would appear closest to the source, up till 40 mm followed with an out-stretched fouling gradient with increased fouling thickness over distance.

In Figure B.2b the irradiance graph is displayed for the same QR, with the same conditions except that there is no scattering. Light outcoupling is only attributed to Fresnel outcoupling. The irradiance pattern consists of a very distinct spiky pattern. What is also noted is that the power quickly gets very low, and a thick fouling pattern, without any clear gradient would be expected.

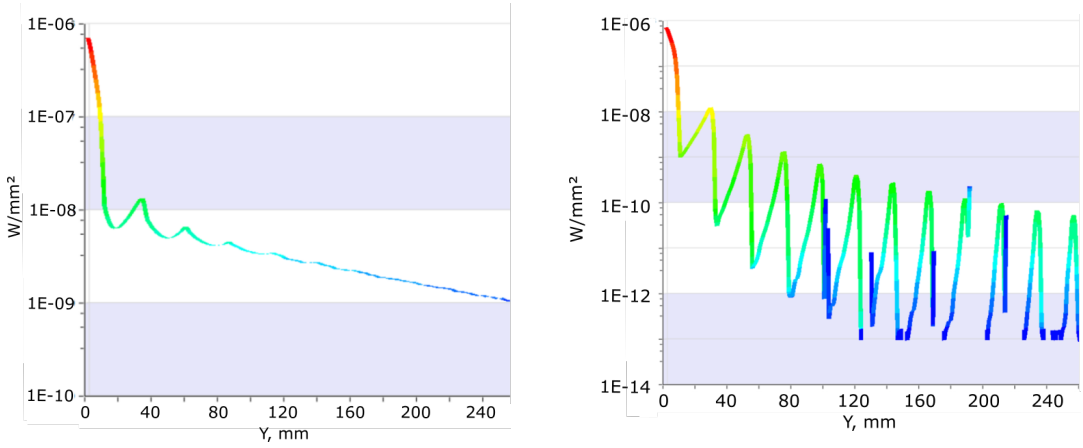

(a) MFP = 55 mm

(b) No HG-scattering

Figure B.2: The two images display the big difference between HG scattering with a MFP of 55 mm, and no bulk scattering with only Fresnel reflections to the surface of the quartz rod. The entire rod measured 350 mm but the graph was cut-off for a more easily view of the results.

Parallel ray experiment

The parallel ray experiment was modeled without a ceramic knife. It was believed to be difficult to detect irradiance for a square micrometer, the estimated size of a bacteria, and therefore hard to simulate the antifouling effect of parallel rays. The detector used is placed 1 μm above the quartz plate surface, to detect light extraction via scattering or Fresnel outcoupling.

The same source parameters were used as mentioned in the above section, **scattering experiment**, with a modified distance in front of the quartz plate edge of 2 mm and with an angular spread of 65°, since a different LED source was used. The quartz plate measured 178x178x3 mm (width, length, height). The source was immersed in an air cavity, overlapping with the quartz plate. All of the surfaces of the quartz were modeled as optically smooth with Fresnel losses.

The quartz material had a HG-scattering with a g-parameter of 0.85, a mean free path of 20,000 mm, and a refractive index of 1.496. The surface detector was an array of 400x400 bins in x- and y-direction. The entire construction was immersed in salt water with a refractive index of 1.39. A MFP value of 20,000 mm was the value determined to best correlate the LT irradiance pattern with observed fouling pattern.

Evanescent wave experiment

The LightTools model of the evanescent wave experiment used the same model as for the scattering experiment. The sample **without** the quartz tube, had a quartz rod with a diameter of 10 mm and a length of 800 mm. The surface detector, with an array of 1 bin in the x-direction and 800 bins in the y-direction, was placed 1 μm above and surrounding the quartz rod surface. The evanescent wave experiment **with** an outer quartz tube consisted of a quartz rod with 10 mm in diameter, placed inside a quartz tube, with an outer diameter of 15 mm and a wall thickness of 1.5 mm. Both the quartz tube and quartz rod were 800 mm in length. The surface detector was placed 1 μm above the quartz tube surface. The two quartz details had intermediate water between them which were modeled by immersing the entire construction in salt water with a refractive index of 1.39. For a more accurate model the intermediate water should be modeled as demineralized water. This was never done because of the demineralized water's refractive index, for $\lambda = 275$ nm, was unknown and time constraints did not allow for literature investigation nor estimated calculations. The refractive index of demineralized water was therefore approximated to the same value as for oceanic water.

Appendix C

Optical power in Fresnel outcoupled light

The reflection and transmission are calculated using the Fresnel equations, according to [15]. An illustration is seen in Figure C.1 that highlights the importance of understanding how light is outcoupled and internally reflected. This because fouling-fringes were observed in the fouling pattern on many of the experiments. The fouling fringes were partly explained by LT simulations when Fresnel losses were activated as an optical property on the quartz surface of the different quartz waveguides. To understand what part of the light is transmitted and reflected, the first light-surface interaction has to be regarded. It is assumed that LT implements the following equations.

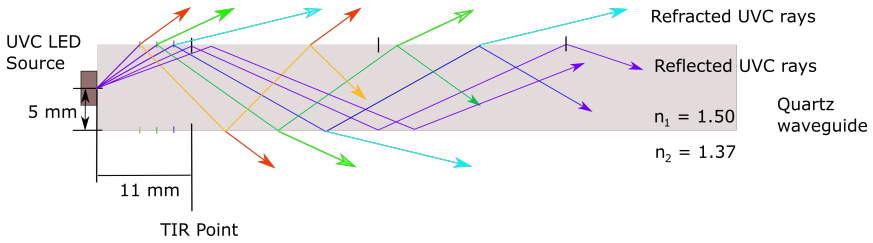

Figure C.1: An illustration of how different light rays behave as they undergo Fresnel reflection and total internal reflection in a quartz waveguide, immersed in oceanic sea water. Part of the light is Fresnel outcoupled, and part of the light is reflected for incident angles smaller than the critical angle.

To calculate the reflected power for light rays with an incident angle greater than 0°, the polarization has to be taken into account. The following equations are used to calculate the fraction of reflected s- and p-polarized power. The reflectance are given by the following expressions where R_s is the transverse electric (**TE**) and R_p is the transverse magnetic (**TM**).

$$R_s = \frac{n_1 cos\theta_i - n_2 cos\theta_r}{n_1 cos\theta_i + n_2 cos\theta_r} \tag{C.1}$$

$$R_p = \frac{n_1 cos\theta_r - n_2 cos\theta_i}{n_1 cos\theta_r + n_2 sec\theta_i} \tag{C.2}$$

where n_1 is the refractive index of the incidence dielectric material, quartz, n_2 is the refractive index of the refracted dielectric material, salt water. θ_i is the angle of incidence, and θ_r is the angle of refraction, calculated using Snell's law [10].

The power transmittance, T, is given by the following equations.

$$R_s + T_s = 1$$

and

$$R_p + T_p = 1$$

since our incident light is unpolarized, the following equation is used.

$$R_{tot} = \frac{1}{2}(R_s + R_p)$$

The implemented MATLAB code is found below. The resulting graphs and table is found in section 4.2.4.

```
%Author: Erik Wilson
%Date: 2018-04-22
%Name: Power in Fresnel outcoupled light

%Purpose: To calculate the amount of Fresnel reflection/transmission (outcoupling),
%including both polarization directions, depending on different incidence angles

%About Polarization: S, perpendicular, y | p, parallel, x.
format longEng
%Defenitions
%Refractive indices (lambda = 275 nm)
n_quartz = 1.496;
n_water = 1.366;
n_1 = n_quartz;
n_2 = n_water;

%Calculating the critical angle
theta_c = asin(n_2/n_1);
%The different angles of incidence (Sweeping from 0 to critical angle)
theta_i = linspace(0,theta_c,100);

for i = 1:length(theta_i)
    %Calculating angle of refraction w Snells law
    theta_r(i) = asin((n_1/n_2)*sin(theta_i(i)));

    R_s(i) = abs((n_1*cos(theta_i(i))-(n_2*cos(theta_r(i)))) /
    (n_1*cos(theta_i(i))+(n_2*cos(theta_r(i))))^2;
    R_p(i) = abs((n_1*cos(theta_r(i))-(n_2*cos(theta_i(i)))) /
    (n_1*cos(theta_r(i))+(n_2*cos(theta_i(i))))^2;

    T_s(i) = 1 - R_s(i);
    T_p(i) = 1 - R_p(i);

    R_tot(i) = (1/2)*(abs(R_s(i))^2 + abs(R_p(i))^2);
    T_tot(i) = 1 - R_tot(i);
end

subplot(1,3,1)
plot(theta_i*(180/pi), R_s, 'LineWidth', 2)
hold on
plot(theta_i*(180/pi), T_s, 'LineWidth', 2)
ylim([0.88 1]);
xlim([56 66]);
legend('R_s', 'T_s', 'Location', 'northwest')
xlabel('\theta_i - degrees')
ylabel('Transmittance, T')

subplot(1,3,2)
plot(theta_i*(180/pi), R_p, 'LineWidth', 2)
hold on
plot(theta_i*(180/pi), T_p, 'LineWidth', 2)
ylim([0.88 1]);
xlim([56 66]);
legend('R_p', 'T_p', 'Location', 'northwest')
xlabel('\theta_i - degrees')
ylabel('Transmittance, T')

subplot(1,3,3)
plot(theta_i*(180/pi), T_tot, 'b', 'LineWidth', 2)
ylim([0.88 1]);
xlim([56 66]);
legend('T_{tot} = 1 - R_{tot}', 'Location', 'northwest')
xlabel('\theta_i - degrees')
ylabel('Transmittance, T')

%%
%table creation
```

```
M = cell(6,9);
M{1,1} = 'theta_i';
M{2,1} = 'theta_i (degrees)';
M{3,1} = 'theta_r';
M{4,1} = 'theta_r (degrees)';
M{5,1} = 'R';
M{6,1} = 'T';

theta_i2 = linspace(58*(2*pi()/360),theta_c,8);
for f = 1:length(theta_i2)
    M{1,(f+1)} = theta_i2(f);
    M{2,(f+1)} = theta_i2(f) * (360 / (2*pi()));

    theta_r(f) = asin((n_1/n_2)*sin(theta_i2(f)));
    M{3,(f+1)} = theta_r(f);
    M{4,(f+1)} = theta_r(f) * (360 / (2*pi()));

    R_s2(f) = abs((n_1*cos(theta_i(f))-(n_2*cos(theta_r(f)))) /
    (n_1*cos(theta_i(f))+(n_2*cos(theta_r(f)))))^2;
    R_p2(f) = abs((n_1*cos(theta_r(f))-(n_2*cos(theta_i(f)))) /
    (n_1*cos(theta_r(f))+(n_2*cos(theta_i(f)))))^2;

    T_s2(f) = 1 - R_s2(f);
    T_p2(f) = 1 - R_p2(f);

    R_tot2(f) = (1/2)*(abs(R_s2(f))^2 + abs(R_p2(f))^2);
    M{5,(f+1)} = R_tot2(f);

    T_tot2(f) = 1 - R_tot2(f);
    M{6,(f+1)} = T_tot2(f);
end
```

Appendix D

Evanescent wave: Calculations and simulations

The following equations discuss a frustrated evanescent wave, and how much light is transmitted into the frustrated object depending on distance between waveguide surface and frustrating object [18]:

$$1/T = \alpha \sinh^2 y + \beta, \tag{D.1}$$

where

$$y = (2\pi d/\lambda)(n_1^2 \sin^2\theta_1 - n_2^2)^{1/2} \tag{D.2}$$

and the 'transmission coefficients' α and β take the forms $\alpha_\perp$, $\alpha_\parallel$, $\beta_\perp$, and $\beta_\parallel$:

$$\alpha_\perp = \frac{(N^2-1)(n^2N^2-1)}{4N^2\cos\theta_1(N^2\sin^2\theta_1-1)(n^2-\sin^2\theta_1)^{1/2}}, \tag{D.3}$$

$$\beta_\perp = \frac{[(n^2-\sin^2\theta_1)^{1/2}+\cos\theta_1]^2}{4\cos\theta_1(n^2-\sin^2\theta_1)^{1/2}}, \tag{D.4}$$

$$\alpha_\parallel = (\alpha_\perp/n^2)\big((N^2+1)\sin^2\theta_1-1\big)\big((n^2N^2+1)\sin^2\theta_1-n^2\big), \tag{D.5}$$

$$\beta_\parallel = \frac{[(n^2-\sin^2\theta_1)^{1/2}+n^2\cos\theta_1]^2}{4n^2\cos\theta_1(n^2-\sin^2\theta_1)^{1/2}}. \tag{D.6}$$

where $n \equiv (n_3/n_1)$, $N \equiv (n_1/n_2)$, T is the transmission and d is the width between the waveguide surface and the frustrating object.

The above equations are implemented in an example of FTIR below where a 3-layered structure is regarded for quartz-conditioning layer-e.coli. Its MATLAB code is found below and resulting graphs are found in section 6.2.3.

```
%Author: Erik Wilson
%Date: 2017-01-08
%Purpose: To replicate example provided in literature:
%Frustrated total internal reflection - a demonstration and review
%S.Zhu, A.W. Yu, D. Hawley and R. Roy, 1985.
%----------------------------------
%Peak UVC wavelength
lambda = 275e-09;
%Wavelength dep. Refractive index for quartz
n_1 = 1.496;
%Refrtactive index of salt water
n_2 = 1.366;
%Refractive index of E.coli bacterium
n_3 = 1.4453916;
%Refractive indices relations defined by literature
n = n_3/n_1;
N = n_1/n_2;
%Incidence angle = 70 degrees
psi_1 = 70*(pi/180);
%Perpendicular constants
alpha_per = ((N^2-1)*(n^2*N^2-1)) / (4*N^2*cos(psi_1)*
    (N^2*sin(psi_1)^2-1)*sqrt(n^2-sin(psi_1)^2));
beta_per = (sqrt(n^2 - sin(psi_1)^2)+cos(psi_1))^2 /
    (4*cos(psi_1)*sqrt(n^2-sin(psi_1)^2));
%Parallel constants
alpha_para = (alpha_per/n^2)*((N^2+1)*sin(psi_1)^2-1)*
    ((n^2*N^2+1)*sin(psi_1)^2-n^2);
beta_para = (sqrt(n^2-sin(psi_1)^2)+n^2*cos(psi_1))^2 /
    (4*n^2*cos(psi_1)*sqrt(n^2-sin(psi_1)^2));
%Penetration depth
d = linspace(0, 1.6*lambda, 100);
for i = 1:length(d)
    y(i) = ((2 * pi * d(i)) / lambda) * sqrt(n_1^2 * sin(psi_1)^2 - n_2^2);
    T_per(i) = 1/(alpha_per*sinh(y(i))^2+beta_per);
    T_para(i) = 1/(alpha_para*sinh(y(i))^2+beta_para);
    T_tot(i) = (T_per(i)+T_para(i))/2;
end
subplot(1,2,1), plot(d/lambda, T_per, 'Linestyle', '--')
hold on
subplot(1,2,1), plot(d/lambda, T_para, 'Linestyle', '-.')
hold on
subplot(1,2,1), plot(d/lambda, T_tot, 'LineWidth', 1)
ylabel('Transmission, T')
xlabel('d/\lambda')
legend('T_{\perp}','T_{\mid\mid}', 'T_{tot} = T_{\perp} + T_{\mid\mid}')
str = sprintf('FTIR for E.coli at incidence angle = 70 degrees');
title(str)
%----------------------------------
%Next subplot
%Critical angle
theta_c = asin(n_2/n_1);
%Incidence angle = 65.94 degrees
psi_1 = linspace(theta_c + 0.0001, pi/2, 100);
%fixed depth
d = 50e-9;
for a = 1:length(psi_1)
    y(i) = ((2 * pi * d) / lambda) * sqrt(n_1^2 * sin(psi_1(a))^2 - n_2^2);
    %Perpendicular constants
    alpha_per(a) = ((N^2-1)*(n^2*N^2-1)) / (4*N^2*cos(psi_1(a))*
        (N^2*sin(psi_1(a))^2-1)*sqrt(n^2-sin(psi_1(a))^2));
    beta_per(a) = (sqrt(n^2 - sin(psi_1(a))^2)+cos(psi_1(a)))^2 /
        (4*cos(psi_1(a))*sqrt(n^2-sin(psi_1(a))^2));
    %Parallel constants
    alpha_para(a) = (alpha_per(a)/n^2)*((N^2+1)*sin(psi_1(a))^2-1)*
        ((n^2*N^2+1)*sin(psi_1(a))^2-n^2);
    beta_para(a) = (sqrt(n^2-sin(psi_1(a))^2)+n^2*cos(psi_1(a)))^2 /
        (4*n^2*cos(psi_1(a))*sqrt(n^2-sin(psi_1(a))^2));
```

```
    T_per(a) = 1/(alpha_per(a)*sinh(y(i))^2+beta_per(a));
    T_para(a) = 1/(alpha_para(a)*sinh(y(i))^2+beta_para(a));
    T_tot(a) = (T_per(a)+T_para(a))/2;
end
subplot(1,2,2), plot(psi_1 * (180/pi), T_per, 'Linestyle', '--')
hold on
subplot(1,2,2), plot(psi_1 * (180/pi), T_para, 'Linestyle', '-.')
hold on
subplot(1,2,2), plot(psi_1 * (180/pi), T_tot, 'LineWidth', 1)
ylabel('Transmission, T')
xlabel('\Phi, degrees')
legend('T_{\perp}','T_{\mid\mid}', 'T_{tot} = T_{\perp} + T_{\mid\mid}')
str = sprintf('FTIR at d = 50 nm, and swept incidence angles');
title(str)
```

Appendix E

SEM-analysis of direct-lit quartz slices

The following appendix presents a scanning electron microscopy, SEM, investigation of direct-lit quartz slides, immersed for 44 days.

Purpose

The purpose of the experiment is to create a surface where a transition from a fouled, to a completely clean area, is present, and to create an experiment that is easy to investigate using a SEM. The completely clean surface will also be investigated on the nanoscale to examine if a conditioning layer, or traces of one, is present.

Method

Samples

Four samples were created using 30x30x3 mm (WxLxH) quartz slides where a UVC LED was attached in direct contact with the backside, in a center position. It is adhered using silicone glue that also acts as a sealer.

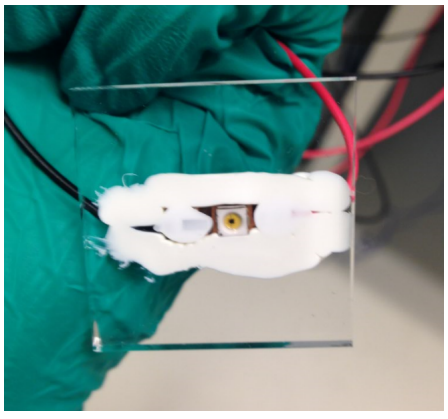

(a) One of the quartz slide samples before immersion.

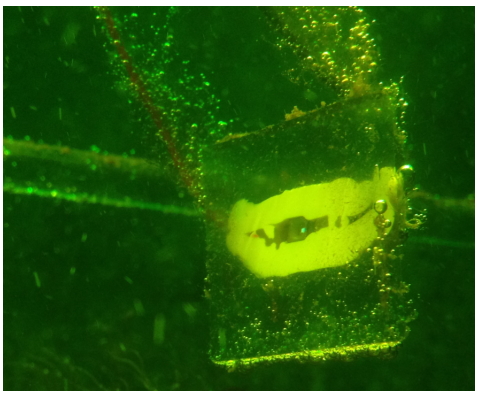

(b) One quartz slide sample immersed in one of the aquaria after 19 days.

Figure E.1: 2 samples are seen before and during the experiment. The optical power was 1.3 mW.

Immersion

The four samples were immersed in three different aquaria and suspended on various depths by attaching the wires connected to the LED. The sources have an optical power of 1.3 mW.

Retrieval and SEM preparation

The samples were retrieved after 44 days of immersion and rinsed in BSA. The samples were put in a 3% formaldehyde solution for 10 minutes, to fixate the cell membranes. A dehydration step followed where the samples were put in buffered solutions of ethanol for 10 minutes each in 30%, 50%, 70% and 100% ethanol steps, before they were put in the ambient air for the remaining solution to evaporate. The samples are lastly sputtered with platinum. The platinum sputtering offers greater contrast since no environmental SEM was available.

Results

A selection of the SEM images can be seen below.

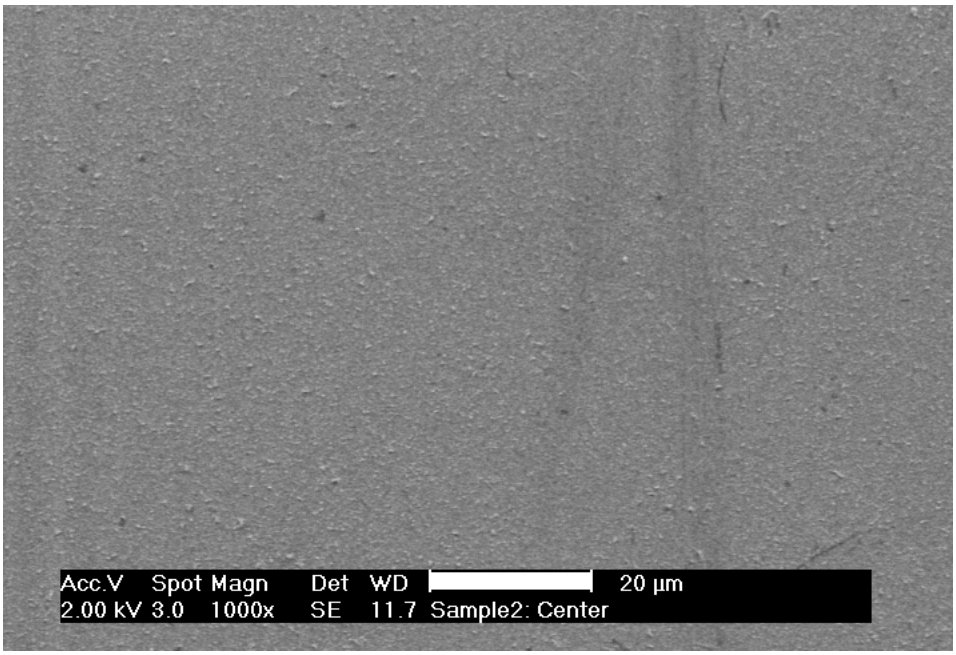

(a) The center position of a quartz slide sample, previously regarded as completely clean when inspected by eye.

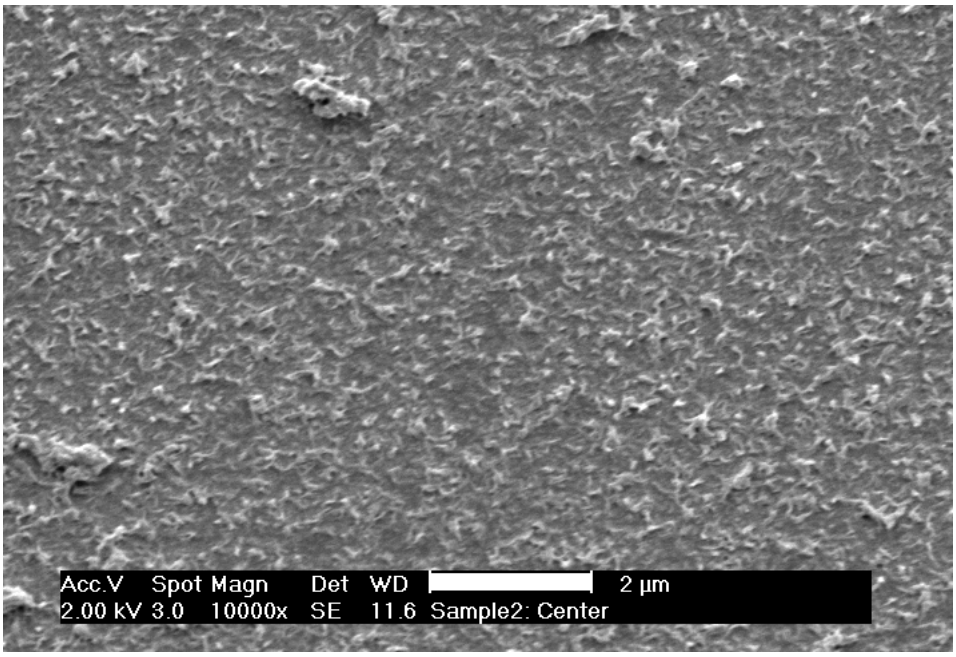

(b) The center position of a quartz slide, up close, previously regarded as completely clean when inspected by eye. No bacteria can be seen.

Figure E.2: One quartz slide sample was investigated in the center of the quartz surface after being sputtered. No biofilm could be seen by visible inspection, and no bacteria was seen in the images. The surface is believed to be covered in organic polymers, making up the conditioning film.

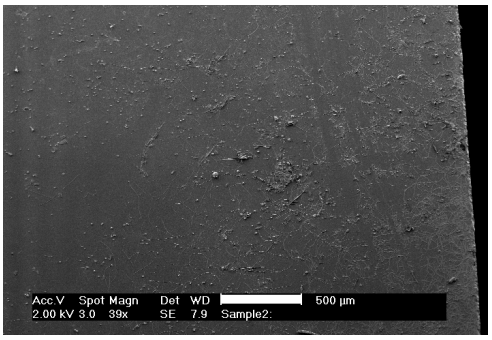

(a) In the corner of the quartz surface.

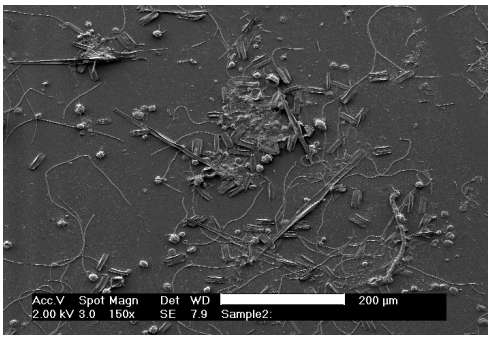

(b) Diatoms and bacteria grouped together.

(c) Diatoms often survived the preparation steps.

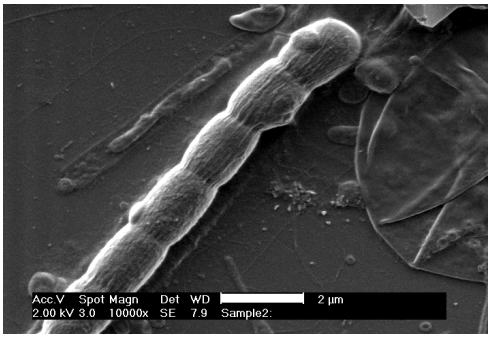

(d) Closeup of bacteria strand.

Figure E.3: Example images of some fouling found close to a corner of a quartz slide sample. The same area is increasingly magnified. Diatoms and bacteria were most often found together. Figure E.3d is believed to be a bacteria population.

Observations

No bacteria were found in the areas which had no visible biofilm formation by eye. This area was made up of a circle, roughly 10 mm in diameter, directly above the UVC LED. Residues, believed to be organic polymers making up the conditioning layer, were found on the otherwise regarded as completely clean surface, seen in Figure E.2. Further away from the center, a few single bacteria were found. The majority of the bacteria were found to have imploded, and an insufficient sample preparation was believed to be the reason. Even further away from the center of the quartz slide, closer towards the quartz slide edges, more fouling was found. It was often bacteria, in combination with diatoms, in small isolated populations, seen in Figure E.3.

Appendix F

Glossary

Optics

Diffuser A surface that diffuses, spreads out or scatters light in some manner.

Intensity $[W/m^2]$ In physics, the intensity is the power $[J/s]$ transferred per unit area (m^2), where the area is measured on the plane perpendicular to the direction of the propagation of the energy. Intensity most often refer to the visible light part of the electromagnetic spectrum.

Irradiance $[W/m^2]$ The radiant flux (power $[J/s]$) received by a surface per unit area (m^2). Used in radiometry which deals with detection and measurement of electromagnetic radiation across the total spectrum. Irradiance is used frequently in this thesis because of the thorough work with UVC light.

Lambertian emitter An emitter where the light, radiant intensity or luminous intensity apply Lambert's cosine law (also known as cosine emission law or Lambert's emission law) which states that the intensity observed from an ideal diffusely reflecting surface or ideal diffuse radiator is directly proportional to the cosine of the angle θ between the direction of the incident light and the surface normal.

Luminous intensity $[cd$, candela] A measure of the wavelength-weighted power emitted by a light source in a particular direction per unit solid angle. Meaning, it is adjusted for the human eye based on the luminosity function.

MFP Mean Free Path, the average distance a photon travels before successive impact which modifies its direction or energy.

Radiant flux $[W]$ The radiant energy received per unit time

Radiant intensity $[W/sr$, Watt per steradian] The radiant flux received, per unit solid angle.

Chemistry

BSA Bovine serum albumin. A protein, used as nutrient in cell and microbial culture.

IPA Isopropyl alcohol.

PMMA Poly(methyl methacrylate)

General

SEM Scanning Electron Microscope. A type of electron microscope that produces a topographic image of a sample by collecting the scattered electron from shooting a focused electron beam at the sample surface.

Bibliography

[1] Bart Salters. "Prevention of bio-fouling by using UV-light emission outwards from the ship hull". In: *17th International Congress on Marine Corrosion and Fouling*. 2014.

[2] Bart Salters and Roelant Hietbrink. "Progress in Philips RunWell UV-based antifouling technology". In: *18th International Congress on Marine Corrosion and Fouling*. 2016.

[3] MP Schultz et al. "Economic impact of biofouling on a naval surface ship". In: *Biofouling* 27.1 (2011), pp. 87–98.

[4] James A Callow and Maureen E Callow. "Trends in the development of environmentally friendly fouling-resistant marine coatings". In: *Nature communications* 2 (2011), p. 244.

[5] Erik Wilson and Niklas Hansson. "Problemet med marin påväxt och dess lösningar". In: (2015).

[6] Kowalski W. *Ultraviolet Germicidal Irradiation Handbook*. Springer, 2009.

[7] Bart Salters et al. "Prevention of biofouling using UV-light emission from low voltage miniature LEDs". In: *Pacific 2015 - International maritime exposition*. 2015.

[8] M. N Polyanskiy. *Refractive index database*. 1965. URL: `http://refractiveindex.info/?shelf=main&book=SiO2&page=Malitson` (visited on 06/15/2016).

[9] Roswell W Austin and George Halikas. "The index of refraction of seawater". In: *U.S. Department of Commerce. National Technical Information Service* (1976).

[10] E. Hecht. *Optics 4th edition*. Pearson education. Addison-Wesley, 2002. ISBN: 9780321188786. URL: `https://books.google.se/books?id=T3ofAQAAMAAJ`.

[11] James P Black and Kirt C Hickman. "Bulk scatter measurements in fused silica at two wavelengths: a comparison with Rayleigh scatter theory". In: *SPIE's 1993 International Symposium on Optics, Imaging, and Instrumentation*. International Society for Optics and Photonics. 1993, pp. 273–284.

[12] Sven Schröder et al. "Bulk scattering properties of synthetic fused silica at 193 nm". In: *Optics express* 14.22 (2006), pp. 10537–10549.

[13] Lord Rayleigh. "XXXIV. On the transmission of light through an atmosphere containing small particles in suspension, and on the origin of the blue of the sky". In: *The London, Edinburgh, and Dublin Philosophical Magazine and Journal of Science* 47.287 (1899), pp. 375–384.

[14] Synopsys. *Digital instruction manual - LightTools 8.4*. Synopsys. May 2016.

[15] Bahaa EA Saleh, Malvin Carl Teich, and Bahaa E Saleh. *Fundamentals of Photonics*. Wiley New Jersey, 2007.

[16] D Axelrod, Edward H. Hellen, and Robert M Fulbright. "Total Internal Reflection Fluorescence". In: *Topics in Fluorescence Spectroscopy*. Ed. by Joseph R Lakowicz. Vol. 3. Okluwer academic publishers, 2004. Chap. 7, pp. 289–337.

[17] Frédérique de Fornel. *Evanescent waves: from Newtonian optics to atomic optics*. Vol. 73. Springer Science & Business Media, 2001.

[18] S Zhu et al. "Frustrated total internal reflection: a demonstration and review". In: *Am. J. Phys* 54.7 (1986), pp. 601–607.

[19] D Roberts et al. "Factors influencing initial larval settlement: temporal, spatial and surface molecular components". In: *Journal of Experimental Marine Biology and Ecology* 150.2 (1991), pp. 203–221.

[20] George I Loeb and Rex A Neihof. "Marine Conditioning Films". In: ed. by Robert E Baier. Vol. 145. American Chemical Society, 1975. Chap. 16, pp. 319–335.

[21] Martin Wahl. "Marine epibiosis. I. Fouling and antifouling: some basic aspects". In: *Marine Ecology Progress Series* 58 (1989), pp. 175–189.

[22] Anand Jain and Narayan B Bhosle. "Biochemical composition of the marine conditioning film: implications for bacterial adhesion". In: *Biofouling* 25.1 (2009), pp. 13–19.

[23] M Lehaitre, L Delauney, and C Compère. "Biofouling and underwater measurements". In: *Real-time observation systems for ecosystem dynamics and harmful algal blooms: Theory, instrumentation and modelling. Oceanographic Methodology Series. UNESCO, Paris* (2008), pp. 463–493.

[24] KE Cooksey and B Wigglesworth-Cooksey. "Adhesion of bacteria and diatoms to surfaces in the sea: a review". In: *Aquatic Microbial Ecology* 9.1 (1995), pp. 87–96.

[25] Colin Munn. *Marine microbiology*. Garland Science, 2003.

[26] Jagadish S Patil et al. "Ultraviolet radiation (UV-C): a potential tool for the control of biofouling on marine optical instruments". In: *Biofouling* 23.4 (2007), pp. 215–230.

[27] LH DiSalvo and AB Cobet. "Control of an estuarine microfouling sequence on optical surfaces using low-intensity ultraviolet irradiation". In: *Applied microbiology* 27.1 (1974), pp. 172–178.

[28] Rajeshwar P Sinha and Donat-P Häder. "UV-induced DNA damage and repair: a review". In: *Photochemical & Photobiological Sciences* 1.4 (2002), pp. 225–236.

[29] Bruce Alberts et al. *Essential cell biology*. Garland Science, 2013.

[30] Aleksei E Balaev, KN Dvoretski, and Valeri A Doubrovski. "Refractive index of Escherichia coli cells". In: *Saratov Fall Meeting 2001*. International Society for Optics and Photonics. 2002, pp. 253–260.

[31] Emily Ralston and Geoffrey Swain. "Can biomimicry and bioinspiration provide solutions for fouling control?" In: *Marine Technology Society Journal* 45.4 (2011), pp. 216–227.

[32] Nils Schuergers et al. "Cyanobacteria use micro-optics to sense light direction". In: *Elife* 5 (2016), e12620.

[33] Brian Dean and Bharat Bhushan. "Shark-skin surfaces for fluid-drag reduction in turbulent flow: a review". In: *Philosophical Transactions of the Royal Society of London A: Mathematical, Physical and Engineering Sciences* 368.1929 (2010), pp. 4775–4806.

[34] Wen Jing Yang et al. "Polymer brush coatings for combating marine biofouling". In: *Progress in Polymer Science* 39.5 (2014), pp. 1017–1042.

Framtidens lösning mot marin påväxt utnyttjar UVC-ljus

Finns det ingen bättre lösning mot marin påväxt än giftig båtbottenfärg? I samarbete med Philips Research undersöktes hur deras framtida lösning – UVC- ljusemitterande ytor, förhindrar påväxt på ett effektivare, och mer miljövänligt sätt, med bara ljus!

UVC ljus har en våglängd mellan 100 - 280 nm och absorberas vanligtvis av ozonlagret vilket motverkar att vi får hudcancer. Det är därför inte bara en bra våglängd för att skapa cellmutation utan också bra till att skada bakterier och används idag i reningsverk och för desinficering i stor utsträckning. Tack vare att ljuskällorna har gått från att vara stora och ömtåliga lysrör, till nu lysdioder, ökar också möjligheterna och därmed användningsområdena.

Med mindre ljuskällor kan man skapa en film med inbäddade LEDs, likt en tapet, som sätts mot fartygsskrov där hela ytan emitterar UVC-ljus med en våglängd på 275 nm. Ingen marin organism kommer att kunna slå sig ner och börja växa på fartygsskrovet och ljuset uppfattas bara ett par centimeter från ytan före det absorberas helt av vattnet. Den här tekniken möjliggör därför ett helt rent fartygsskrov och skadar inte på något sätt den marina miljön.

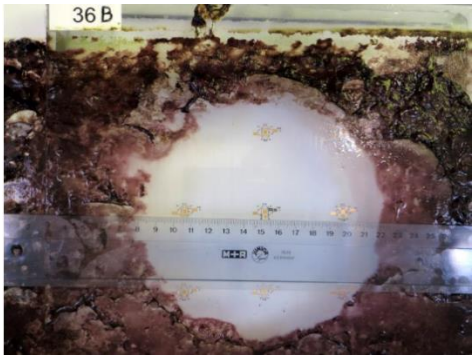

Figur 1 *En enstaka lysdiod i mitten av bilden på 1 mW ljusenergi håller en ca 110 cm² area helt ren från marin påväxt som kan ses omringa den rena cirkeln.*

Philips har jobbat med det här konceptet i snart 3 år och visat att det fungerar genom att hålla en större yta helt ren från marin påväxt under en längre tid, i havsvatten.

Vill man täcka ett helt containerfartyg med den UV-ljusemitterande filmen, kommer den ca 10.000 m² stora ytan att behöva ungefär 10.000 W, vilket är ungefär lika mycket effekt som 5 vattenkokare.

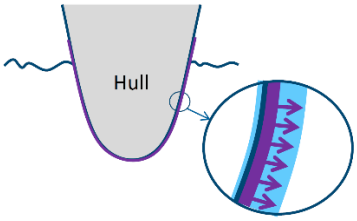

Figur 2 *Philips UV-ljusemitterande film kan ses emittera ljus från fartygsskrovet ut mot vattnet och på så sätt förhindra alla marina organismer från att sätta sig.*

I min forskning undersökte jag exakt hur UV-ljuset tar sig ut från materialet (extraheras), in i organismerna på ytan och dödar dem (antifouling). Förstår man detta bättre kan man optimera den ljusemitterande filmen och använda mindre energi för att hålla en lika stor yta ren.

Olika optiska teorier beskriver olika ljusextraktionsmekanismer som alla beskriver hur ljuset på olika sätt lämnar materialet. Några av mekanismerna är via ljusspridning (scattering), Fresnel utkoppling (Fresnel outcoupling) och via en försvinnande våg (evanescent wave).

Olika experiment designades för att antingen förstärka, eller förhindra de teoretiska ljusextraktionsmekanismerna. Plattor och stavar av kvartsglas med LEDs sänktes ner i akvarium innehållande Nordsjövatten i mellan 7 och 90 dagar. Resultatet blev marin påväxt i olika mönster som jämfördes med de andra experimenten och datorsimuleringar, för att fastslå vad som egentligen händer.

Slutsatsen av arbetet var att ingen av de teoretiska ljusextraktionsmekanismerna gick att utesluta och samtliga mekanismer tros därför påverkade marin påväxt och till att hålla glasplattan i Figur 1 helt ren.